Geometric superinductors and their applications in circuit quantum electrodynamics

by

Matilda Peruzzo

August, 2021

A thesis presented to the
Graduate School
of the
Institute of Science and Technology Austria, Klosterneuburg, Austria
in partial fulfillment of the requirements
for the degree of
Doctor of Philosophy

I|S|T AUSTRIA

Institute of Science and Technology

The thesis of Matilda Peruzzo, titled *Geometric superinductors and their applications in circuit quantum electrodynamics*, is approved by:

Supervisor: Johannes Fink, IST Austria, Klosterneuburg, Austria

Signature: _____

Committee Member: Georgios Katsaros, IST Austria, Klosterneuburg, Austria

Signature: _____

Committee Member: Ioan Pop, KIT Physikalisches Institut, Karlsruhe, Germany

Signature: _____

Defense Chair: Kimberly Modic, IST Austria, Klosterneuburg, Austria

Signature: _____

signed page is on file

I hereby declare that this thesis is my own work and that it does not contain other people's work without this being so stated; this thesis does not contain my previous work without this being stated, and the bibliography contains all the literature that I used in writing the dissertation.

I declare that this is a true copy of my thesis, including any final revisions, as approved by my thesis committee, and that this thesis has not been submitted for a higher degree to any other university or institution.

I certify that any republication of materials presented in this thesis has been approved by the relevant publishers and co-authors.

Signature: _____

Matilda Peruzzo

August, 2021

signed page is on file

Abstract

This work is concerned with two fascinating circuit quantum electrodynamics components, the Josephson junction and the geometric superinductor, and the interesting experiments that can be done by combining the two. The Josephson junction has revolutionized the field of superconducting circuits as a non-linear dissipation-less circuit element and is used in almost all superconducting qubit implementations since the 90s. On the other hand the superinductor is a relatively new circuit element introduced as a key component of the fluxonium qubit in 2009. This is an inductor with characteristic impedance $Z_\mathrm{C} = \sqrt{L/C}$ larger than the resistance quantum $R_\mathrm{Q} = \Phi_0/(2e) \approx 6.45$ kΩ and self resonance frequency $f_0 = 1/(2\pi\sqrt{LC})$ in the GHz regime.

The combination of these two elements can occur in two fundamental ways: in parallel and in series. When connected in parallel the two create the fluxonium qubit, a loop with large inductance and a rich energy spectrum reliant on quantum tunneling. On the other hand placing the two elements in series aids with the measurement of the IV curve of a single Josephson junction in a high impedance environment. In this limit theory predicts that the junction will behave as its dual element: the phase-slip junction. While the Josephson junction acts as a non-linear inductor the phase-slip junction has the behavior of a non-linear capacitance and can be used to measure new Josephson junction phenomena, namely Coulomb blockade of Cooper pairs and phase-locked Bloch oscillations. The latter experiment allows for a direct link between frequency and current which is an elusive connection in quantum metrology.

This work introduces the geometric superinductor, a superconducting circuit element where the high inductance is due to the geometry rather than the material properties of the superconductor, realized from a highly miniaturized superconducting planar coil. These structures will be described and characterized as resonators and qubit inductors and progress towards the measurement of phase-locked Bloch oscillations will be presented.

Acknowledgments

About the Author

Matilda completed a Physics Msci at Kings College London. Her research there mainly revolved around light scattering in photonic glass in the context of random lasing and thermoelectric materials. In the fall of 2015 she started graduate school at IST Austria where she initially worked on electro-mechanics by simulating and modelling the coupling between high impedance resonators and the design of an on-chip mechanical circulator. She then transitioned to her project: studying geometric superinductors. Her work required the fabrication of an extensive amount of complex microchips, the construction of a low temperature microwave setup and the development of software for qubit measurements.

List of Publications

1. S. Barzanjeh, M. Wulf, **M. Peruzzo**, M. Kalaee, P. B. Dieterle, O. Painter & J. M. Fink, Mechanical on-chip microwave circulator, Nature Comm., **8**, 953 (2017)

2. M. Kalaee, M. Mirhosseini, P. B. Dieterle, **M. Peruzzo**, J. M. Fink, O. Painter, Quantum electromechanics of a hypersonic crystal, Nature Nano., **14**, 334-339 (2019)

3. S. Barzanjeh, E. S. Redchenko, **M. Peruzzo**, M. Wulf, J. M. Fink, Stationary Entangled Radiation from Micromechanical Motion, Nature, **570**, 480-483 (2019)

4. **M. Peruzzo**, A. Trioni, F. Hassani, M. Zemlicka, J. M. Fink, Surpassing the resistance quantum with a geometric superinductor, Phys. Rev. App., **14**, 044055 (2020)

5. **M. Peruzzo**, F. Hassani, G. Szep, A. Trioni, E. S. Redchenko, M. Zemlicka, J. M. Fink, Geometric superinductance qubits: Controlling phase delocalization across a single Josephson junction, arXiv:2106.05882 (2021)

6. F. Hassani, **M. Peruzzo**, J. M. Fink, The inductively shunted transmon qubit, in preparation (2021)

Contents

List of Tables

List of Figures

List of Abbreviations

AC Alternating Current

ACE Acetone

Al Aluminum

AWG Arbitrary Waveform Generator

dB deciBel

DC Direct Current

HEMT High Electron Mobility Transistor

HF Hydrogen Fluoride (acid)

ICP Inductively Coupled Plasma

IPA Isopropyl alcohol

JJ Josephson Junction

LC Inductance-Capacitance

LO Local Oscillator

LOR Lift-Off Resist

NMP N-Methyl-2-pyrrolidone

PCB Printed Circuit Board

PEC Proximity Effect Correction

PMMA PolyMethylMethAcrylate

RC Resistor-Capacitor

RF Radio Frequency

RT Room Temperature

Si Silicon

SMA Sub-Miniature A (connector)

SOI Silicon on Insulator

SQUID Superconducting QUantum Interference Device

TLS Two Level Systems

transmon transmission line shunted plasma oscillation qubit

UC UltraSonicator

UHV Ultra High Vacuum (evaporator)

VNA Vector Network Analyzer

CHAPTER 1

INTRODUCTION

1.1 IMPEDANCE AND QUANTUM FLUCTUATIONS IN SUPERCONDUCTING CIRCUITS

Superconducting circuits are the playing field of two quantum variables: the charge (n) and the phase (ϕ) [Krantz, 2019; Blais, 2021]. These play the role of the position and momentum and as such they satisfy the commutation relation

$$[\hat{\phi}, \hat{n}] = i. \tag{1.1}$$

From the uncertainty principle it follows that if one of these quantities is well defined the other must be uncertain.

A relevant example is the LC circuit formed by an inductor in parallel with a capacitor. Such a circuit is dissipationless, as it doesn't include resistance, and linear. The latter implies that the energy difference between any two adjacent quantum states is constant. The charge of the LC circuit is defined as the displacement charge on the capacitor plates $\hat{Q} = 2e\hat{n}$ given by the number of Cooper pairs $\hat{n}$ multiplied by the charge of a single Cooper pair $2e$. The flux of the circuit, on the other hand, is related to the phase by $\hat{\Phi} = 2\pi\Phi_0\hat{\phi}$ with Φ_0 being the magnetic flux quantum. In the LC circuit Φ represents the generalized flux inside the inductor.

The relevant parameter that distinguishes between the charge certain regime and the phase certain regime is Z_C/R_Q, where $Z_C = \sqrt{L/C}$ is the characteristic impedance of the circuit and $R_Q = \Phi_0/(2e) \approx 6.45$ kΩ is the resistance quantum obtained from the ratio between the flux and charge quanta. $Z_C/R_Q << 1$ indicates a low impedance circuit which allows for high charge fluctuations making the phase a low uncertainty, semi-classical variable. On the other hand if Z_C is larger than the resistance quantum phase fluctuations dominate leaving the charge well-defined [Manucharyan, 2012; Ulrich, 2016]. This can be extracted from the analysis of quantum fluctuations of the LC circuit [Manucharyan, 2012]. The ground state energy of the quantum LC circuit $\hbar\omega/2$ accepts contributions from the charge and the phase

$$\frac{\hbar\omega}{2} = \frac{\delta\hat{Q}^2}{2C} + \frac{\delta\hat{\Phi}^2}{2L}, \tag{1.2}$$

where $\omega = 1/\sqrt{LC}$.

As the capacitive and inductive contributions carry equal weight due to the equipartition

theorem we can express the relative charge number and phase fluctuations (δn and $\delta \phi$ respectively) in terms of the characteristic impedance of the circuit Z_C and the resistance quantum R_Q

$$
\begin{aligned}
\delta \hat{n} &= \frac{\delta \hat{Q}}{2e} = \sqrt{\frac{R_Q}{4\pi Z_0}}, \\
\delta \hat{\phi} &= \frac{\delta \hat{\Phi}}{\Phi_0} = \sqrt{\frac{Z_0}{4\pi R_Q}}.
\end{aligned}
\tag{1.3}
$$

Eq. 1.3 shows that the charge fluctuations can be reduced with high characteristic impedance. Most superconducting circuits are in the phase-certain regime as nature generally prefers low impedance. The impedance of vacuum is $Z_{\text{vac}} = \sqrt{\mu_0/\epsilon_0} = 377\Omega$ and most electrical engineering environments are less then that (typically 50 Ω) however there exists an opposite regime where charge is well-defined and a phase is highly uncertain.

The work presented here seeks to investigate the behaviour of a critical superconducting element, the Josephson junction, as it is placed in a high-impedance environment. In this chapter we will look at the physics of Josephson junctions, what to expect when one is placed in high impedance and how planar spiral inductors can be used to reach this regime. Then a few applications of high-impedance superconducting physics will be explored.

1.1.1 SHORT INTRODUCTION TO JOSEPHSON JUNCTIONS

A Josephson junction arises when two superconducting wavefunctions are separated by distance small enough that their exponential tails overlap [Josephson, 1962; Tinkham, 1996]. The material between them could be a dielectric, a normal conducting metal or even a section of superconductor with very small diameter, here we will consider the Superinductor Insulator Superinductor (SIS) junction.

The overlap of the superconducting wavefunctions allows for the possibility of Cooper pair tunneling between the two superconductors. This tunneling is governed by the first Josephson relation

$$
I_S = I_C \sin(\phi_J),
\tag{1.4}
$$

where I_C is the critical current and ϕ_J is the phase difference between the two superconducting wavefunctions. The second Josephson relation regards the voltage $V(t)$ that arises

across the junction due to a change of phase

$$\frac{d\phi_J}{dt} = V(t)\Phi_0. \tag{1.5}$$

In reality the entirety of the circuit must be taken into account, this typically includes a capacitance and a resistance in parallel with the junction. By combining Ohm's law ($I = V/R$) and the displacement current of the capacitor ($I = CdV/dt$) with Eqs, 1.4 and 1.5 the equation of motion for the phase is

$$C\frac{\Phi_0}{2\pi}\frac{d^2\phi_J}{dt^2} + \frac{1}{R}\frac{\Phi_0}{2\pi}\frac{d\phi_J}{dt} + I_C\sin(\phi_J) = I, \tag{1.6}$$

commonly named the Resistively and Capacitively Shunted Junction (RCSJ) model, this is a second order differential equation and in most cases must be solved numerically. Physically the resistive term arises from the resistance of the insulating barrier in series with any shunting resistance added to the circuit while the capacitive term is due to any geometrically induced capacitance between the two electrodes of the junction. In the case of semi-classical phase (low impedance) the motion of the junction phase resembles that of a ball rolling down a tilted washboard potential as seen in Fig. 1.1(a). The tilt of the washboard is given by the total current passing through the junction (I). When the current is larger than the critical current (I_C) the tilt of the washboard is such that no minima are formed and the ball (phase) rolls down the potential. The effect manifests itself in the IV curve of a Josephson junction. If the current is slowly ramped up no voltage (ie. no change in phase according to 1.5) appears until $I > I_C$ after which the voltage increases to reach the Ohmic limit. The IV curve for this process can be seen in Fig. 1.1(b).

Like a ball rolling down a washboard potential experiences a gravitational force with *effective* mass M_{eff} and friction η can be expressed as:

$$M_{\text{eff}} = (\frac{\Phi_0}{2\pi})^2 C,$$
$$\eta = (\frac{\Phi_0}{2\pi})^2 \frac{1}{R}, \tag{1.7}$$
$$U = -E_J\cos\phi_J - \frac{\hbar I}{2e}\phi_J$$

where $E_J = \Phi_0/(2\pi)I_C$, I_C being the critical current and U is the washboard potential. A useful figure of merit [Stewart, 1968; McCumber, 1968] is the quality factor of the junction

$$Q = \omega_{\text{c}}/\omega_{\text{RC}}, \tag{1.8}$$
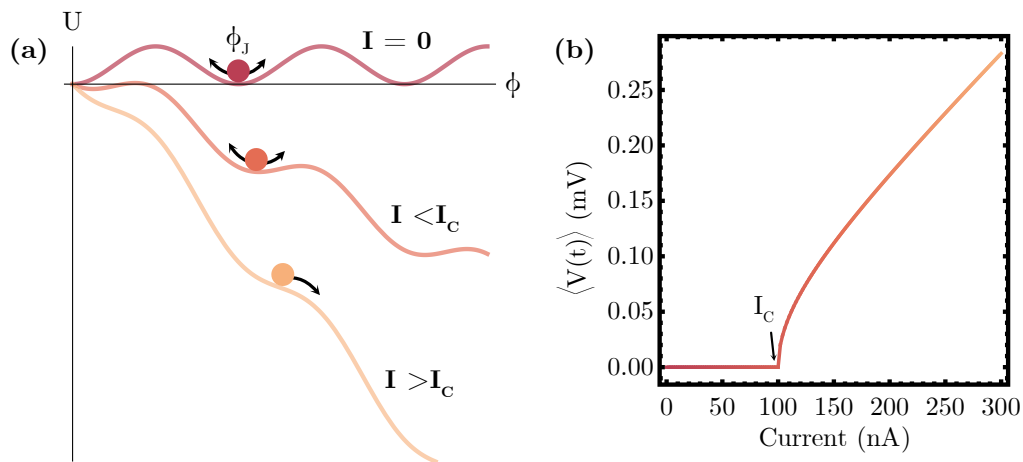
Figure 1.1: **Tilted washboard potential and IV curve of a Josephson junction.** (a) Potential the phase (ϕ_J) in a Josephson junction under the semi-classical approximation. The three curves represent three different values of the applied current. In the case where the applied current is less than the critical current I_C (red and orange curves) the phase particle is still trapped in a local minimum while in the case of $I > I_C$ the potential no longer has minima and the phase particle is allowed to roll down. (b) The resulting IV curve.

which compares two timescales: the characteristic frequency $\omega_c = ((2\pi/\Phi_0)I_C R)^{1/2}$, the inverse relaxation time of the system, and the characteristic frequency $\omega_{RC} = 1/RC$, the inverse relaxation time of the corresponding RC circuit.

When $Q < 1$ the junction is considered *overdamped*, specifically the friction force is dominant and the ball has little inertia. When $Q > 1$ the junction is *underdamped* which means there is little friction slowing the junction down.

The distinction between under- and over-damped becomes clear when the current is decreased from $I > I_C$ down to zero. When the current reaches the critical current minima are formed in the potential. In an overdamped junction the phase is slowed down by friction and is immediately stuck in a the minima, as the phase is no longer changing the voltage goes to zero. However if the junction is underdamped the phase will maintain it's inertia and continue rolling even though minima are formed in the potential. Therefore hysteretic behaviour is associated with underdamped junctions.

Figure 1.2 shows the different IV curves of an underdamped junction for increasing current (solid line) and decreasing current (dashed line) displaying a strong hysteresis. The current at which the junction switches to the voltage state is the switching current I_{sw}. In
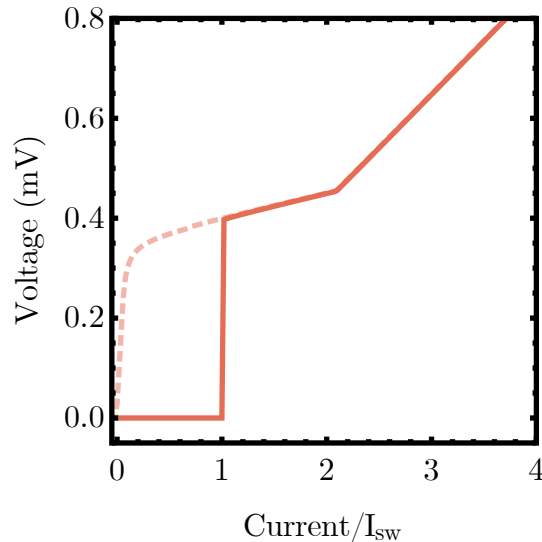
Figure 1.2: **IV curve or an underdamped junction.** Solid line represents the IV curve when current is increased from zero to above the critical current. The dashed line represents the IV curve for current being decreased from above the critical current to zero. The current axis is normalized as to the switching current I_{sw} which represents the current at which a junction switches to the voltage state.

the case of no noise or fluctuations affecting the junction the switching current coincides with the critical current. When decreasing the current the voltage returns to zero at a value lower than the switching and critical current known as the return current I_R.

When fluctuations (quantum or thermal) are considered the possibility of phase tunnelling emerges. This allows for the voltage to be non-zero at currents below the critical current. In overdamped junctions this effect manifests as a rounding of the curve seen in Fig. 1.1(b) around the critical current [Ambegaokar, 1969], while in underdamped junctions tunnelling events cause the junction to jump to the voltage state lowering the switching current below the critical current. Due to the random nature of the tunneling process the switching current is a random value that falls in a distribution [Fulton, 1974; Washburn, 1985; Blackburn, 2014].

Another interesting feature of the Josephson junction is the shape of the IV curve when it is irradiated with an AC current. In fact in the case where the junction is overdamped and the amplitude of the AC current is around $0.5I_C$, steps appear in the IV curve at specific voltage values:

$$V_n = n\frac{hf}{2e} \tag{1.9}$$
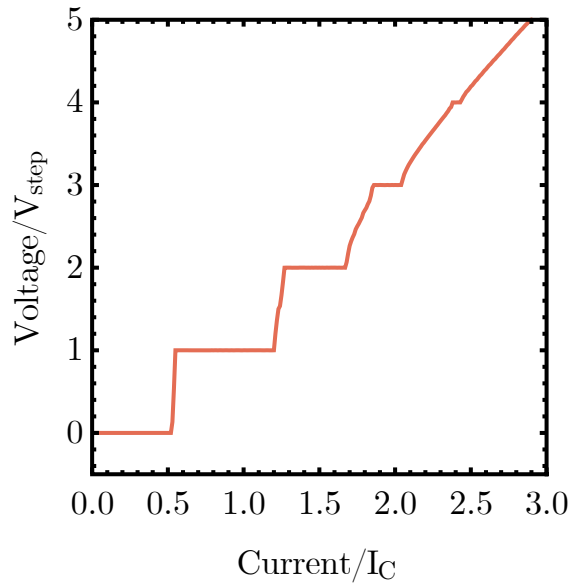
Figure 1.3: **IV curve of an underdamped junction under microwave irradiation.** The plot shows the current (normalized by the critical current) vs. the voltage arising across the junction (normalized by the Shapiro step height defined in Eq. 1.9) when an AC current with frequency of 100 GHz is threaded through. The steps occur at integer values of V_{step}.

where V_n is the voltage position of the nth step, f is the frequency and h and e are the Plank constant and electron charge. The key to this measurement is having the applied current oscillate around the critical value, I_C. This results in a periodic dipping of the tilting potential. If the phase particle resonates with this oscillation it will be able to jump to subsequent minima during the dips which will change the phase by multiple of 2π and hence return quantized voltage steps as seen in Fig. 1.3. These are named Shapiro steps after S. Shapiro measured the effect in 1963 [Shapiro, 1963]. Due to atomic clock technology frequency is defined with a very high precision and the Shapiro steps relate voltage to frequency conferring voltage a similar measurement accuracy. This effect is used to establish a very precise voltage standard [Hamilton, 1997].

1.1.2 FROM JOSEPHSON JUNCTIONS TO PHASE-SLIP JUNCTIONS

So far the Josephson junction was considered in an environment with a level of quantum phase fluctuation well below 2π and therefore the phase is a well defined (classical) variable

and the charge across the junction capacitance is subject to high quantum fluctuations. The phase defined Josephson junction presented in Section 1.1.1 has often been described as a non-linear inductor [Tinkham, 1996; Vool, 2017] due to the nonlinear relationship between current and phase. Its conjugate circuit element would be a non-linear capacitor where the voltage is defined by a 2e periodic relation to charge. Conjugacy implies that one can mathematically switch between the two circuits by means of the transformations:

$$E_J \rightarrow E_S \qquad C \rightarrow L \qquad \phi \rightarrow n \qquad (1.10)$$

where $E_S = \frac{2eV_C}{2\pi}$ is the phase-slip energy which depends in turn on the critical voltage V_C and the charge becomes the semiclassical variable with quantum fluctuations below 2e. Consequently one can use many of the reasonings and calculations that apply to the Josephson junction to describe this new component named phase-slip junction.

For example the phase-slip junction's relations can be extracted analogously to the Josephson relations:

$$V = V_C \sin(2\pi n),$$
$$I = \frac{2en}{dt}. \qquad (1.11)$$

Such a non-linear capacitor and can potentially be used for novel types of superconducting quantum circuits [Mooij, 2006; Manucharyan, 2010; Pop, 2010].

While the tunneling event in the Josephson junction is the Cooper pair tunnelling across the insulating barrier, for the phase-slip junction it is the phase-slip. This is a tunneling of the phase between two minima of the washboard potential (see Fig. 1.4).

The phase-slip junction can be built out of a Josephson junction itself as it is approximately a self-dual element [Ulrich, 2016], meaning that under certain approximations it will display the physics of the phase-slip junction. In fact the Hamiltonian of the Josephson junction is

$$\mathcal{H} = 4E_C \hat{N}_{\text{tot}}^2 - E_J \cos(\hat{\phi}), \qquad (1.12)$$

where $E_C = e^2/2C$ is the charging energy and N_{tot} is the total charge on the capacitor plates. It is useful to express charge $\hat{N}_{\text{tot}} = \hat{n} - n_o$ as the sum of a discrete component $\hat{n}$ which can only change by integers and a continuous component n_o which represents the environment induced offset charge. The energy levels of Eq. 1.12 show a 2e periodicity in the offset charge with a maximum at $n_o = \pm 0.5$. The voltage is therefore also 2e periodic. However when the junction is connected to an external circuit these effects are usually

obscured by charge fluctuations in n_o that completely wash out the charge dependence of the voltage. This is where the ability of high impedance to suppress charge fluctuations comes into play [Arndt, 2018].

The ability of characteristic impedance to affect charge fluctuations and unlock the dual behavior of the Josephson junction can be explored by considering a loop with a junction as a weak link. This circuit is known as the RF SQUID, as seen in Fig. 1.5(b). The Hamiltonian of such a circuit is

$$\mathcal{H} = 4E_C(\hat{n} - n_o)^2 - E_J \cos(\hat{\phi}) + \frac{1}{2}E_L(\hat{\phi} + \phi_{\text{ext}})^2. \tag{1.13}$$

ϕ_{ext} is the flux threaded through the circuit loop and is a continuous variable and $E_L = (\frac{\Phi_0}{2\pi})^2/L$ is the inductive energy.

The Hamiltonian is nothing but the Cooper pair box Hamiltonian (Eq. 1.12) with an additional inductive term. In the limit of high impedance ($E_L << E_C$) the phase and the charge dynamics can be adiabatically decoupled and the phase wavefunction is acted on by a series of Hamiltonians [Koch, 2007; Ulrich, 2016]

$$\mathcal{H}^{(s)} = \frac{E_L}{2}(\frac{d}{d\hat{q}} + \frac{2\pi\Phi}{\Phi_0})^2 + \epsilon_s(\hat{q}), \tag{1.14}$$

where $\epsilon_s(\hat{q})$ represent the Cooper pair box energy levels associated with the band s. The variable $\hat{q}$ is the quasicharge, an externally supplied charge which exists in the interval $[0, 1)$ [Koch, 2009; Pechenezhskiy, 2020]. The approximation is valid for $E_L << E_C$ and for negligible coupling between different energy bands that is achieved by $E_J/E_C > 2$. As the Cooper pair box energy bands are 2e periodic they can be mathematically expressed as a Fourier series, when increasing E_J/E_C the lowest band reduces of a cosine potential.
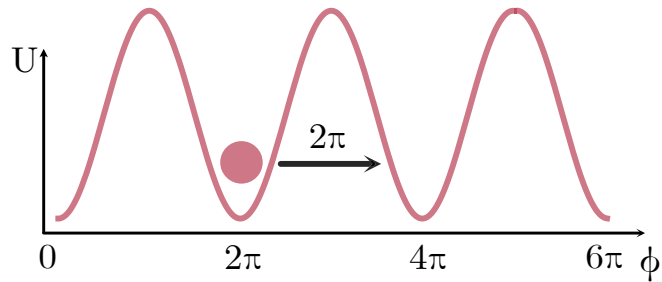
Figure 1.4: **Phase-slip event.** A phase-slip is an abrupt change in phase by 2π which corresponds to the phase of the junction tunneling through the potential to another minima.

9
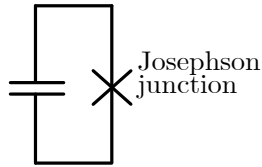
(a) Cooper pair Box   **(b)** RF SQUID   **(c)** Phase-slip box
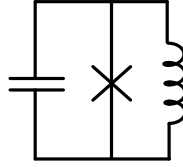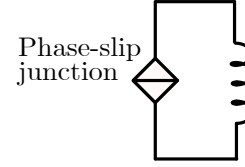
Figure 1.5: **Circuit diagrams:** (a) Circuit diagram of a Cooper Pair Box described by the Hamiltonian in Eq. 1.12. (b) Circuit diagram of an inductively shunted Cooper pair box described by the Hamiltonian in Eq. 1.13. (c) Circuit diagram of the phase slip box described by the Hamiltonian in Eq. 1.15.

In the limit of $\epsilon_s(\hat{q})$ being in cosine form the Hamiltonian of the lowest Cooper pair band can be re-written as

$$\mathcal{H}^{(1)} = \frac{E_L}{2}(\hat{\phi} + \phi_{ext})^2 + E_S \cos(\pi\hat{q}/e). \tag{1.15}$$

Here we have introduced E_S which is the phase-slip rate. It represents the total charge dispersion of the Cooper pair box energy band and for $E_J/E_C \gtrsim 1$ is given by

$$E_S = E_C^{1/4} E_J^{3/4} e^{-(8E_J/E_C)^{1/2}}. \tag{1.16}$$

The phase slip rate determines the critical voltage of the phase-slip junction as $V_C = \frac{E_S}{he}$. The Hamiltonian in Eq. 1.15 is the dual of the Cooper pair Hamiltonian under the transformation in Eq. 1.10. Its circuit diagram is displayed in Fig. 1.5(c) where the phase-slip junction symbol is introduced.

In conclusion this section has shown how it is possible to make a phase-slip junction by placing a Josephson junction in a high impedance environment.

1.2 A CASE FOR GEOMETRIC IMPEDANCE

In section 1.1.2 the importance of high impedance was delineated, in this section the specific method we use to obtain said impedance is presented theoretically.

This section is based on the ideas presented in Ref. [Peruzzo, 2020]. In recent years

the field of superconducting quantum circuits has been introduced to a new player: the superinductor. A superinductor is defined as a circuit element which has characteristic impedance Z_C greater than the quantum impedance R_Q, has zero DC resistance and is in its ground state at mK temperatures. This last criteria implies its self-resonance resides at least in the GHz regime. In order for a superinductor to be useful, especially in quantum computing, it also needs to have low microwave losses [Manucharyan, 2012].

Despite these challenging requirements the superconducting community has successfully surpassed the quantum resistance with a variety of methods. Among these is using disordered superconductors which have high kinetic impedance [Grünhaupt, 2018; Grünhaupt, 2019; Wang, 2019; Hazard, 2019; Kamenov, 2020] and Josephson junction chains [Manucharyan, 2009; Bell, 2012; Nguyen, 2019; Pechenezhskiy, 2020] which act effectively as inductors.

Geometric inductances were widely considered to be not suited to be superinductors [Manucharyan, 2009; Manucharyan, 2012; Masluk, 2012; Kamenov, 2020] since reaching $Z_C > R_Q$ is impossible with a simple single-wire resonator as the impedance will be limited to the order of magnitude of the free space impedance Z_{vac}. The geometric impedance of a wire according to the transmission line model is constant with respect to length and is defined by

$$Z_{\text{wire}} = \frac{1}{\pi} \sqrt{\frac{\mu_0}{\epsilon_0 \epsilon_r}} \text{arccosh}(d/w), \tag{1.17}$$

where w is the width of the wire and d is the distance to ground. One could try to rise Z_{wire} by increasing d, since w is ultimately limited by fabrication, by pulling the wire apart from the ground. However, when a separation in the order of the wavelength is reached, the circuit starts radiating energy, behaving as an antenna [Manucharyan, 2012]. It is the same effect as loading the transmission line with a load resistance, that turns out to be in the order of Z_{vac} at resonance. The wire impedance is clearly not able to reach the resistance quantum, however by using the mutual inductance contribution of concentric loops (i.e. a planar coil) this limit is lifted and we are able to satisfy all superinductor requirements. In fact the geometric inductance of such a structure is enhanced as expressed by [Mohan, 1999]

$$L_g = \frac{\mu_0 n^2 d_{\text{av}} c_1}{2} (\ln(c_2/\rho) + c_3 \rho + c_4 \rho^2), \tag{1.18}$$

where μ_0 is the vacuum permeability (assuming none of the material have magnetic properties), n is the number of turns, $d_{\text{av}} = \frac{d_{\text{in}} + d_{\text{out}}}{2}$ is the average between the inner and the

outer diameter of the coil and $\rho = \frac{d_{\text{out}} - d_{\text{in}}}{d_{\text{out}} + d_{\text{in}}}$ is the *fill-ratio* of the coil. $c_{1,2,3,4}$ are geometry dependent constants, for circular coils they are (1.0, 2.5, 0.0, 0.2) and for square coils they are (1.27, 2.07, 0.18, 0.13). All the considerations in this section regard circular coils, however in later chapters square ones will be considered as well. As d_{out} is linear in the number of turns Eq. 1.18 shows the geometric inductance L_g increases as n^3.

From Ref. [Maleeva, 2014] the resonance of a planar coil can be analytically calculated to be

$$f_0 = \sqrt{\gamma \frac{c_0^2}{\epsilon_{\text{eff}}} \left(\frac{2p}{\pi(d_{\text{in}} + 2np)^2} \right)^2}, \qquad (1.19)$$

where γ is a shape-dependant constant which for circular coils is 0.656(4), the pitch p is the distance between adjacent turns (i.e. wire width plus spacing) and ϵ_{eff} is the effective permittivity of the environment, n is again the number of turns and c_0 is the speed of light in vacuum. Due to them having less symmetries an exact formula for the frequency of square coils is not available.

Eq. 1.19 is based on purely geometric considerations and as a result it shows the frequency scaling as $f_0 \sim \text{pitch}^{-1} n^{-2} \sim l^{-1}$ similar to a $\lambda/2$ resonator. By assuming we are dealing with an LC oscillator we can express the impedance as $Z_C = \sqrt{L/C} = 2\pi f_0 L$ and from this conclude that the characteristic impedance scales with number of turns. We can therefore conclude that planar coil resonators with small pitch and large number of turns are viable candidates to be superinductors.

Fig. 1.6 compares a straight wire to a coiled wire (i.e. a planar resonator) by representing the impedance and resonance frequency change as a function of length. The coil's impedance increases as $\sqrt{l}$ contrary to the straight wire which is length independent. On the other hand the frequency decreases as $1/l$ for both cases.

Resonators that rely on kinetic inductance often are less linear (i.e. the frequency of the self-resonance will change with the number of photons) [Maleeva, 2018]. A non-linear inductor is not a big problem if it is a qubit component as qubits are already highly non-linear. However high inductance can also be used for resonators which need to couple to a dipole or parametrically to a mechanically modulated capacitance. In both these examples the coupling strength depends on the resonator's vacuum voltage fluctuations

$$V_{ZPF}^{RMS} = 2\pi f_0 \sqrt{\hbar Z_C / 2}, \qquad (1.20)$$
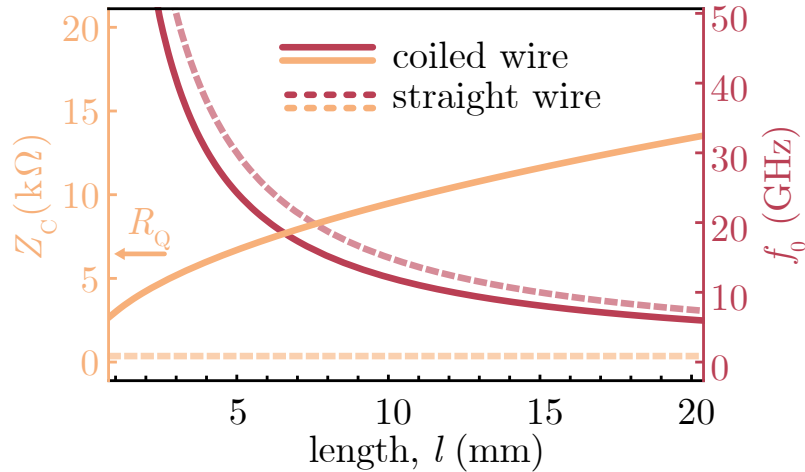
Figure 1.6: **Resonance frequency and characteristic impedance of a planar coil compared to a single wire.** The plot shows the resonance of a coil ($p = 1\mu$m, $\rho = 1$, solid) and wire ($d/w = 10$, dashed) to follow a similar trend. On the other hand the impedance of a straight wire is length-independent unlike the coil where the impedance increases as $\sqrt{l}$. Both systems were considered in vacuum.

where f_0 is the resonator frequency and Z_C is its characteristic impedance. In these cases a linear resonator with high impedance is necessary. Geometric capacitance and inductance doesn't depend on photon number, in fact such resonators are shown to be highly linear until photon numbers reaching 10^7 [Fink, 2016].

In conclusion geometric superinductors constructed from planar coils have all the necessary ingredients to be superinductors with a wide variety of applications.

1.3 APPLICATIONS OF HIGH GEOMETRIC IMPEDANCE

This section will go through some of the most interesting applications of geometric superinductors. The first two sections are the main research areas of this work and the measurements done towards these applications is discussed in later chapters.
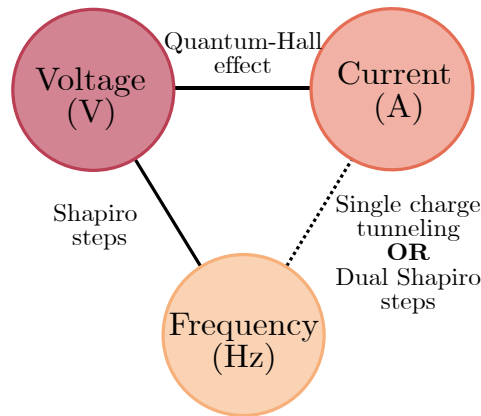
Figure 1.7: **The quantum metrological triangle.** A representation of the three quantities in the metrological triangle (in the circles) and the experiments that relate the quantities to each other (along the lines). The missing link is the connection between current and frequency which the dual Shapiro step experiment has the possibility to close.

1.3.1 CURRENT STANDARD

The realization of a phase-slip element is not only interesting from a theoretical standpoint but may have interesting technological applications. As mentioned in 1.1.1 the Shapiro steps measurement done on Josephson junctions has been a staple for quantum metrology due to it's ability to relate quantities of voltage and frequency through nothing but fundamental constants (see Eq. 1.9). To this day current is defined much less accurately. Metrological experiments attempting to define current use electron pumps which are able to source up to 100 pA with an uncertainty of 2 parts in 10^7 [Scherer, 2019]. In contrast the Volt has an uncertainty lower than 1 part in 10^8 [Piquemal, 2000; Scherer, 2012].

A dual Shapiro step measurement, also referred to in the literature as phase-locked Bloch oscillations would allow to define current with a similar certainty as voltage and hence close the metrological triangle seen in Fig. 1.7. This is the set of three electrical quantum effects that when closed would allow for the definition of the Volt, the Ampere and the Hertz to be interconnected solely in terms of fundamental constants.

As discussed in Section 1.1.2 the dual circuit to the one used to measure Shapiro steps is obtainable by immersing a Josephson junction in a high-impedance environment, however this is easier said than done. Past experiments have relied on the impedance of resistors to meet these requirements [Haviland, 1991; Kuzmin, 1991; Kuzmin, 1992] by implementing

(a) Original circuit   **(b)** Modified circuit
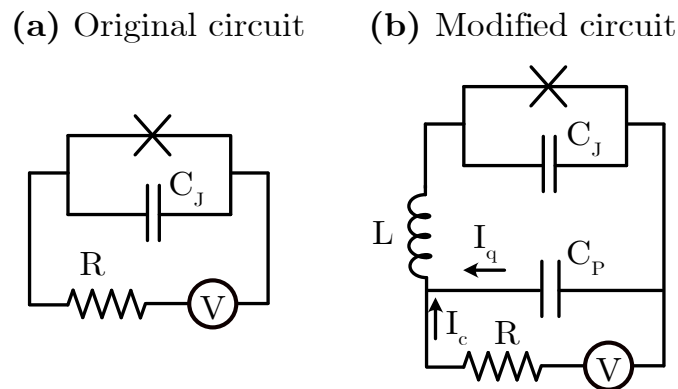
Figure 1.8: **Modified dual Shapiro circuit** The circuit on the left represents the typical circuit used for the measurement of a phase-slip junction in the past. On the right is a modified circuit which inserts a superinductor in series with the Josephson junction and the resistor.

the circuit seen in Fig. 1.8(a). This is a safe method as a large resistance ($R >> R_Q$) will act as an ideal current bias. However for this measurement to work the resistor needs to be placed in proximity to the junction as long leads between the two components will significantly increase the parallel capacitance. The visibility of the dual Josephson effects will depend in the value of critical voltage V_C mentioned in the previous section. This quantity decreases exponentially in magnitude with decreasing E_J/E_C and for E_C to remain in the GHz regime the capacitance needs to remain below 20 fF.

Such small cross capacitance requires short leads and therefore places the junction and the resistor close by which in turn requires the resistor to be a few microns in size and fabricated right next to the junction. As a consequence the resistor will generate strong localized Joule heating in close proximity to the junction adding thermal and quasiparticle noise which has the effect of washing out the steps. This was the issue encountered in [Haviland, 1991] when the experiment was first attempted. A more indepth analysis of the noise encountered in this method was done by Refs. [Kuzmin, 1994; Vora, 2017] and the conclusion was that the thermal quasiparticles were the main contribution to the washing out of the Bloch oscillations.

It seems like the need for a resistor to be close *and* far from the junction makes the measurements of dual Shapiro steps something only possible in the dreams of theoreticians. However the introduction of a lossless high-impedance element (i.e. a superinductor) was shown to be a possible solution. In Ref. [Arndt, 2018] a more intricate circuit is envisioned,

one that includes the junction, the resistor and a large inductor in between. Here different capacitances are distinguished, the Junction capacitance C_J and the parasitic capacitance C_P. The inductance is there to protect the junction from the parasitic capacitance and hence the relevant impedance quantity is $Z = \sqrt{L/C_P}$.

The circuit is composed of two loops, the outer loop which includes the resistor and the voltage source and the inner loop which includes C_P. The currents circulating these loops are denoted I_q and I_q respectively and can be seen depicted in Fig. 1.8(b). The current fluctuations in both of these loops must be minimized in order for the charging effects of the Josephson junction to be visible. If the resistance in the outer loop is large enough $(R \gg R_Q)$ the current I_C can be considered a classical variable. On the other hand the current I_Q does not flow through the resistor and has to be treated as a quantum variable where the current fluctuations are reduced by increasing the impedance.

From a time domain prospective there are three relevant timescales in the system

- $\omega_q = 1/\sqrt{LC_p}$, the plasma frequency of the quantum charge,

- $\omega_c = 1/\sqrt{LC_S}$, the plasma frequency of the classical charge,

- $\omega_R = 1/RC_S$, the RC rate with which the motion is damped.

Here C_S is the capacitance of the phase-slip junction, this is easily confused with the junction capacitance but is a different quantity and usually larger. In order to extract the phase-slip capacitance it is necessary to go back to the phase-slip junction Hamiltonian in Eq. 1.15 where the phase-slip energy $E_S \cos(\pi q/e)$ is defined. By differentiating this term with respect to charge the voltage relation of the phase-slip junction is obtained (see Eq. 1.11) and the critical voltage V_C is calculated. The phase-slip junction capacitance is extracted as follows

$$C_S = \frac{e}{\pi} V_C = \frac{e^2}{\pi^2} E_S. \tag{1.21}$$

This quantity is different from the capacitance of the junction as it depends on *both* E_J and E_C.

The main result of [Arndt, 2018] is finding a generalized equation for the width of the current step which takes into account finite impedance

$$\Delta V = \frac{V_{\text{ac}}}{1 + e^{\pi R_Q/Z}(\omega_0/\omega_R)}, \tag{1.22}$$

where ΔV is the voltage width and V_{ac} and ω_0 are the amplitude and frequency of the irradiated AC voltage and ω_0. This implies that in order to have a step that is not heavily

suppressed the impedance of the system must be ideally around $10\ \mathrm{k\Omega}$. This equation is valid to first order in $V_{\mathrm{ac}}/(e^{-\pi R_\varrho/Z}V_C)$.

In addition they identify a region of parameters where the step is expected to be maximal which is when $\omega_R e^{-\pi R_\varrho/Z}/\omega_{\mathrm{c}} \approx 1$ and $\omega_0/e^{-\pi R_\varrho/Z}\omega_R \approx 0.5$. This implies that the frequency of the AC drive ω_0 will be limited by the resistance of the circuit via ω_R.

1.3.2 RF-SQUID QUBITS

Superinductors are also key elements in inductively shunted superconducting qubits also referred to as RF-SQUID qubits introduced in Section 1.1.2 and Fig. 1.5(b). The ideas in this section are taken from Ref. [Peruzzo, 2021].

Superconducting qubits are highly engineerable quantum systems that are at the forefront of quantum technology due to the offered strong interactions resulting in fast and precise control but also due to the similarity to existing microchip fabrication and the available diversity of circuit designs [Clarke, 2008; Vool, 2017; Krantz, 2019]. Creative new ideas on how to encode, store and control single quanta in electrical circuits paired with state of the art fabrication have not only led to a big push in coherence times but also facilitated the observation of many new quantum physics phenomena [Blais, 2021]. Among the latest qubit designs is the RF-SQUID, which offers high anharmonicity, a rich spectra and is unaffected by static charges [Krantz, 2019]. A specific type of RF-SQUID is the fluxonium [Manucharyan, 2009], characterized by high impedance and wavefunctions delocalized in phase. One of the advantages of this circuit is the ability to create such qubits with small transition frequency and charge matrix element around the flux sweet spot which has led to the energy relaxation time T_1 being greatly extended [Earnest, 2018; Nguyen, 2019; Somoroff, 2021] but driving the qubit transition also becomes increasingly difficult for the same reason. On the opposite side of the RF-SQUID spectrum the qubit can be made flux insensitive by increasing the shunting inductance. This bears resemblance to the transmon where increasing the shunting capacitance decreases charge noise sensitivity [Koch, 2007]. This limit was recently explored in [Pechenezhskiy, 2020] where the lowest qubit transition only varies by 100 MHz across the flux period, such small dispersion allows the flux-limited T_2 to reach hundreds of μs.

In this work qubit inductance is obtained geometrically with a planar coil described in Sec-

tion 1.2. In contrast with kinetic implementations the geometric superinductor presents a single uninterrupted superconducting wavefunction with a fixed and geometrically defined inductance. The design of these qubits is aided by the reproducibility of the geometric inductor where both inductance and capacitance can be calculated with good accuracy as their value is mostly geometry dependent.

The different types of flux qubits described in this work are considered to be different parameter regimes of the Hamiltonian in Eq. 1.13. Of the three energy terms the capacitive term (related to E_C) is considered the kinetic energy while the potential is attributed to the inductive (E_L) and Josephson (E_J) terms. What makes this qubit interesting is the fact that completely different regimes can be reached by changing the relative magnitude of the three energies (E_C, E_L and E_J) while maintaining the same circuit.

Figure 1.9 shows the various qubits that can be constructed with this circuit and the wavefunctions of the ground and excited state superimposed to the qubit potential when the external flux Φ_{ext} is half a flux quantum, i.e. the flux frustration point. Said point is often where the qubit is operated as it is a flux sweet spot where the waveunctions are formed as symmetric and anti-symmetric superpositions of the single well wavefunctions as well as being the point where the qubit is less susceptible to quasiparticles [Pop, 2014]. The qubits are placed on a 2D plot based on the ratios between the two potential terms and the kinetic term in the Hamiltonian.

On the x-axis we have E_L/E_C, given by

$$\frac{E_L}{E_C} = \frac{1}{2\pi^2} (\frac{R_Q}{Z})^2. \tag{1.23}$$

This quantity affects the quadratic part of the Hamiltonian and will determine the quadratic tilt of the potential. The difference is that when the tilt is small the phase is more de-localized as the wavefunctions of the ground and excited states bleed into more wells corresponding to higher phase values. As the qubit wavefunction spreads in phase the qubit transition becomes less sensitive to flux noise.

The y-axis is E_J/E_C and concerns the depth of the periodic wells. In fact the intra-well tunnelling probability E_S is exponentially dependent on E_J/E_C. Decreasing tunneling has the advantage of increasing the relaxation time by means of creating very low frequency qubit transitions. In addition when the qubit is tuned slightly away from the sweet spot the overlap of the ground and excited state wavefunctions is vanishingly small which strongly protects the qubit from relaxation. High E_J/E_C qubits are conventionally named
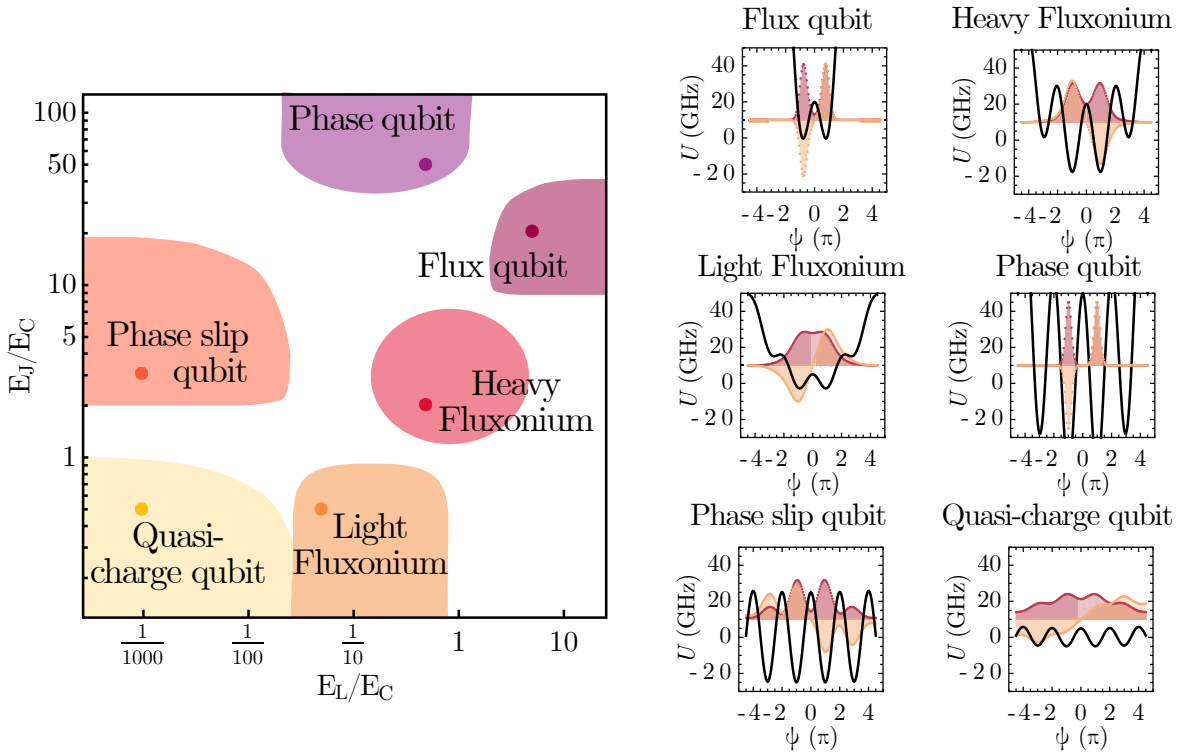
Figure 1.9: **Classification of inductively shunted qubits.** The left plot places the types of inductively shunted qubits on a 2D plane spanned by E_L/E_C and E_J/E_C. The plot identifies regions corresponding several types of RF-SQUIDs. The dots correspond to the specific values of the wavefunction and potential plots on the right. These are representations of the qubit potential at half flux quantum and of the wavefunctions of the ground (red) and excited (orange) states (scaled for visibility).

heavy due to their low kinetic energy.

The different qubits types shown in Fig. 1.9 are the following:

- *The flux qubit:* The wavefunctions of the ground and excited states of these qubits are strongly localized in the lowest potential wells due to both potential terms being higher than the kinetic energy. For E_L close to E_J the system is similar to the flux qubits made out of three junctions in terms of spectrum and properties [Yan, 2016].

- *The inductively shunted transmon*: For intermediate impedance and $E_J/E_C \gg 1$ the transitions between wells become increasingly unlikely and each well contains many plasmon levels. In this limit the qubit spectrum resembles that of a transmon qubit and the dispersion of the plasmon states can be made to be less than 100 MHz. This qubit has also been shown to be accessible with geometric superinductors [Hassani,

2021].

- *The heavy fluxonium:* This circuit is a flux qubit where E_L is close to E_C. Due the high value of E_J/E_C tunneling is unlikely and typically requires involvement of higher order transitions [Vool, 2018] or non adiabatic protocols [Zhang, 2021] to prepare the first excited state at the half flux value. These qubits have demonstrated the highest coherence and relaxation times of all RF-SQUID representations [Nguyen, 2019; Somoroff, 2021].

- *The light fluxonium:* With intermediate impedance and low E_J/E_C the light fluxonium has a lower energy dispersion and anharmonicity than it's heavy counterpart. It's first qubit transition is also found at higher frequencies. However the transition is not well protected from relaxation due to high tunneling probability between wells.

- *The phase-slip qubit:* Qubits in this limit have a high impedance and low inter-well tunneling. As mentioned in Section 1.1.2 the lower levels of this qubit are described by the phase-slip box Hamiltonian from Eq. 1.15.

- *The quasi-charge qubit:* These qubits are similar to the phase-slip qubit but due to low E_L and low E_J with respect to E_C the wavefunction is able to spread further in between wells. In the case of very low E_L/E_C [Pechenezhskiy, 2020] the spread of the wavefunction will extend significantly beyond the two lowest potential wells making the qubit more insensitive to flux noise than its siblings. However, due to low E_J/E_C this qubit has a relatively large wavefunction overlap and hence the state is not well protected from relaxation.

So far the majority of superconducting qubits couple to a resonator capacitively. This type of coupling adds large capacitances to the circuit lowering the charging energy and consequently constraining the circuit parameters. The few inductively coupled qubits have a shared inductance with the resonator which creates a galvanic connection between the two. The type of coupling is often trivially given by the qubit geometry, for example a shared inductance will give an inductive coupling while a large antenna placed in a 3D cavity will produce a capacitive coupling.

However in theory both types are possible so in order to model them the following terms

need to be added to the Hamiltonian in Eq. 1.13

$$H_{\text{int}} = \hbar\omega_R \hat{a}^\dagger \hat{a} - ig_C \hat{n}(\hat{a} - \hat{a}^\dagger) - g_L \hat{\phi}(\hat{a} + \hat{a}^\dagger). \tag{1.24}$$

The first term is the Hamiltonian of the resonator, where ω_R is the resonance frequency and $\hat{a}^\dagger$ ($\hat{a}$) is the creation (annihilation) operator. The second and third term are the capacitive and inductive coupling, where g_C (g_L) is the capacitive (inductive) coupling constant, $\hat{n}$ is the qubit charge operator and $\hat{\phi}$ is the flux operator.

The qubit matrix elements, wavefunctions, potentials and dispersive shifts are calculated with the help of the *scqubits* Python library available at [Koch, 2021].

1.3.3 CAVITY ELECTRO-MECHANICS

As mentioned in Section 1.2 one of the advantages of geometric inductors is their high voltage fluctuations and linearity with respect to other superinductor implementations. Cavity electro-mechanics is a field where a mechanical oscillator is coupled to an LC resonator such that quantum and classical states can be transferred between the two [Aspelmeyer, 2013; Fink, 2016; Dieterle, 2016; Barzanjeh, 2017]. The advantage is that coupling between the oscillators can occur for large difference in resonance frequency, in fact microwave cavity resonances are typically in the GHz regime while mechanical elements resonate at MHz frequencies. An example of such a system can be seen in Fig. 1.10 where a coil is in parallel with a mechanically modulated capacitance. On the right the design of the mechanical element is shown with an exaggerated displacement which is due to the differential mechanical motion of the first in-plane mode. Said motion changes the capacitance of the element and hence the resonance frequency of the LC resonator creating a coupling between the two. Energy exchange between the two systems is obtained when the resonator is pumped at a frequency equal to $f_{\text{res}} \pm f_m$, where f_{res} is the frequency of the resonator and f_m is the frequency of the mechanical mode. This so called side-band pumping enhances the interaction between the two systems allowing the detuned pumped photon to combine with the creation or annihilation of a mechanical quanta in order to create or annihilate a photon on resonance with the cavity. Such a process however only occurs if the photon density of states at the non-resonant sideband is low, i.e. the width of the cavity κ needs to be lower than the frequency of the mechanical mode f_m. This
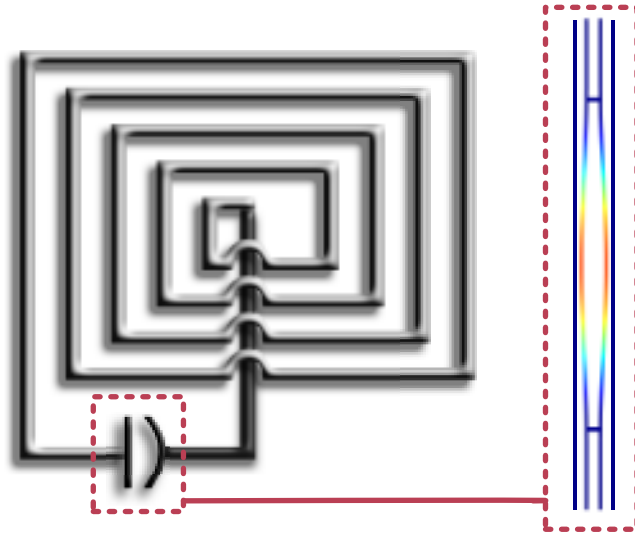
Figure 1.10: **Geometric inductor + mechanics** A scheme of a coil in parallel with a mechanically modulated capacitor. On the right is a simulated distribution of the displacement of the capacitor plates when the mechanical mode is excited. The displacement changes the distance between the capacitor plates and therefore the capacitance of the system.

condition is known as the *side-band limit.*

When the pump is placed at a frequency higher than the LC frequency (blue detuned) mechanical quanta are created while in the case of lower pump frequency (red detuning) quanta are removed from the mechanical system. The latter process allows to cool the mechanical element to its quantum ground state even in the case when thermal fluctuations are higher than the mechanical energy quanta [Teufel, 2011; Fink, 2016].

The figure of merit in these experiments is the cooperativity C which compares the coupling between the two harmonic oscillators and the coupling of each to loss sources. The cooperativity is defined as:

$$C = \frac{4g_0^2 n_{av}}{\kappa \gamma_m} \tag{1.25}$$

where g_0 is the coupling, n_{av} is the average photon number in the LC resonator, κ is the linewidth of the LC resonator and γ_m is the linewidth of the mechanical mode.

The coupling strength (g_0) depends on the way in which the coupling is achieved, often a mechanically modulated capacitor is used where the mechanical motion changes the distance between the capacitor plates and hence the capacitance. When this capacitance is part of an LC oscillator the change in displacement affects the capacitance and hence

the frequency of the resonator. The coupling of two such systems is as follows:

$$g_0 = \frac{\partial \omega}{\partial x} x_{\mathrm{ZPF}} \tag{1.26}$$

where ω is the frequency of the LC resonator, x is the capacitor plates displacement due to mechanical motion and x_{ZPF} is the zero-point fluctuation of the mechanical motion.

In order to increase the derivative in Eq. 1.26 the resonator must have a very low self capacitance such that the mechanically modulated capacitance is more influential, i.e. it must have high impedance. This condition is critical in the cases where the modulated capacitance is in the order of few fF. Additionally Eq. 1.25 tells us that a large amount of photons in the LC cavity also increases coupling, this requires the resonator to have a high linearity.

High impedance *and* linearity is a characteristic typical of geometric superinductors rendering them an ideal component for cavity electro-mechanical experiments.

1.3.4 HARDWARE PROTECTED QUBITS

One of the major challanges of superconducting qubits is to decouple them simultaneously from all intrinsic noise sources present in the environment, specifically flux and charge noise. Several implementations have tackled with these issues but even state of the art qubits barely scratch the *ms* mark in coherence time [Rigetti, 2012; Somoroff, 2021].

In Refs. [Kitaev, 2006; Brooks, 2013] a *hardware protected qubit* was proposed where the protection from environmental noise is two-fold. On the one hand the overlap between ground an excited state is minimized with the effect of prolonging the relaxation time. On the other hand the flux and charge dispersion is flattened which will reduce the effects of noise on the system.

The realization of such a system is obtained by creating a complex but symmetric circuit that is seen in Fig. 1.11. The key is creating a variable that isn't affected by the two main noise sources (charge and flux) and making sure it is decoupled from other variables in the system. Both of these objectives are obtained with a perfectly symmetric implementation of the circuit in Fig. 1.11, however a lack of symmetry between the two inductors risks reducing the decoupling and hence re-introducing noise sources [Groszkowski, 2018].

Geometric superinductors are highly reproducible because of their inductance depending
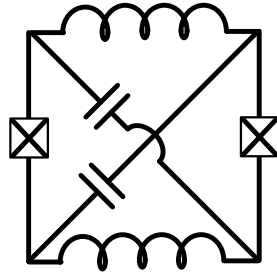
Figure 1.11: **0-π qubit circuit.** Scheme of the proposed circuit composed of several inductors, capacitors and Josephson junctions which is optimized to protect the qubit transition simultaneously from flux and charge noise.

only on the turn number and diameter and therefore are excellent candidates for this type of application.

CHAPTER 2

EXPERIMENTAL METHODS

2.1 CHAPTER INTRO

This chapter discusses the methods by which the experiments presented in subsequent chapters are conducted. These methods include simulations done in order to predict sample parameters, nanofabrication recipes used to make the samples and the description of the setup and techniques used to perform measurements. This final part is devided by the two types of measurements performed for this work: low noise DC setup used for single Josephson junction transport measurements and RF setup and measurements used to characterized coil resonators and qubits.

The setups and methods in this section were constructed with the help of Shabir Barzanjeh, Matthias Wulf and Jason Jung based on the work presented in Ref. [Fink, 2010].

2.2 SIMULATIONS

When designing an experiment simulations are a key aspect as they should inform design decisions. For the work presented in this thesis simulations were mainly carried out in 2D and 3D finite element simulators. The 2D simulator specializes in solving for the complex transmission S, admittance Y and impedance Z of a planar circuit where the user constructs the elements and port configurations. This method is used to extract frequency dependent parameters and is ideal to simulate frequency response of RF circuits. This includes finding its fundamental resonances and the coupling to input lines in the form of the external quality factor Q_e. The quality factor Q is the ratio between the energy stored in a resonator and the energy dissipated per cycle [Pozar, 1993; Göppl, 2008]. The external quality factor Q_e only considers the losses to the input and output line while the internal quality factor Q_i refers to losses through other channels.

The 3D finite element simulator allows to insert lumped elements in the circuit geometry and extract Y for a frequency range. This allows to simulate the admittance of specific circuit element.

(b)

(a)
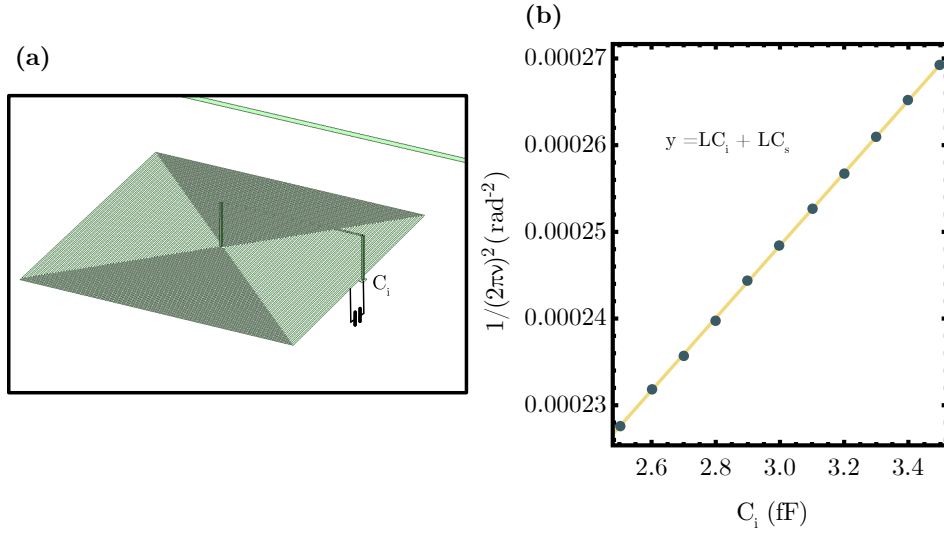
Figure 2.1: **Example of a coil simulation.** (a) Image from the Sonnet GUI where the coil and coupler wire are simulated. The added ideal capacitance C_i is increased in the simulation to obtain the plot in (b). The square coil parameters are $n = 64$, $p = 0.5\mu m$, $d_{out} = 68\ \mu m$ on Silicon on Insulator (SOI). (b) Frequency change as the ideal capacitance (C_i) is increased. The fit allows to extract the intrinsic capacitance and inductance of the coil. The parameters were found to be $L = 61$ nH and $C = 2.9$ fF

2.2.1 COIL SIMULATIONS

Simulations aimed at predicting resonance frequency, capacitance and inductance of coils were performed in Sonnet, a 2D finite element simulator.

The parameters are extracted by adding an ideal series capacitor C_i to the coil and extracting its self-resonance frequency for different capacitances. This occurs by analyzing the reflected signal sent through the coupler wire and identifying the resonance in the phase of S_{11}, $\psi = \tan^{-1}(\mathrm{Im}(S_{11})/\mathrm{Re}(S_{11}))$.

The resonance frequency of the coil is given by $\omega = \frac{1}{\sqrt{L(C_i+C_s)}}$ which can be turned into a linear equation:

$$\frac{1}{\omega^2} = LC_i + LC \tag{2.1}$$

where C_i is the added capacitance and C is the stray capacitance of the coil. By fitting a line for different values of the ideal capacitance L and C can be extracted.

27

2.2.2 SINGLE COIL COUPLING TO WAVEGUIDE

When designing a device it is not only important to know the inductance and capacitance of a resonator but also how it couples to the input line.

The RF devices presented in this thesis were measured in reflection via a coupling to a coplanar waveguide where the center conductor is shorted near the devices. This has two effects: firstly the wave at the short will have a maximum in current and a minimum in voltage allowing it to inductively couple to the devices, in addition the wave gets reflected at the short allowing for a reflection measurement [Fink, 2016; Kalaee, 2019]. The wire near the devices was designed considerably thinner ($< 1\mu m$) than the center conductor of the coplanar waveguide ($\approx 20\mu m$) to reduce capacitance between wire and resonator.

Figure 2.2 shows how the external coupling Q_e varies as a function of distance between the coil edge and the coupler (a-b) but also as a function of distance between the coil center and the symmetry point of the coupler (c-d). This occurs because in the case of the coil being symmetrically placed with respect to the coupler the currents cancel out resulting in no coupling.

2.2.3 DOUBLE COIL COUPLING TO WAVEGUIDE

Symmetry considerations are especially interesting when considering a pair of coils coupled to each other with a coupling factor *g*. In fact placing two coils next to each other causes them to couple inductively and capacitively. The coupling can be extracted by sweeping an ideal capacitor which is connected in parallel with one of the resonators such that the frequencies of the two coils cross. The coupling gives rise to an anticrossing between the modes where the minimum separation is given by **2*g*** seen in Fig. 2.3(c).

When the bare resonance of the two coils is the same the entire system displays collective modes where the currents flow in the coils symmetrically and anti-symmetrically, these are sketched in Fig. 2.3(a) and (b). Which of these modes is lower in frequency will depend on weather the coil winding is the same or opposite.

Knowing the current distribution of the modes allows one to selectively couple to either at will [Toth, 2017; Kalaee, 2019]. Figure 2.3(d) shows how the external quality factor
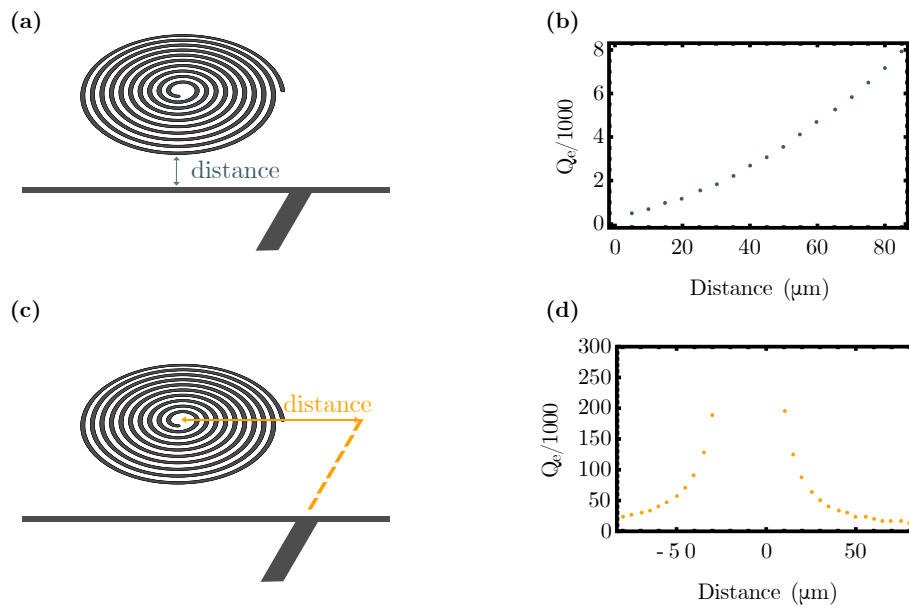
Figure 2.2: **Coupling between the coil and coupler wire.** Simulations showing how external coupling Q_e depends on the relative position between the coil and coupler wire. The square coil parameters are $n = 36$, $p = 1\mu m$, $d_{out} = 74\ \mu m$ on Silicon on Insulator (SOI). (a) and (b) show how the coupling decreases as the coil is moved further from the coupler wire, (a) is a scheme and (b) is Q_e fitted from the simulated S_{11} response. (c) and (d) show how Q_e changes when the position of the coil is changed with respect to the symmetry point of the coupler wire.
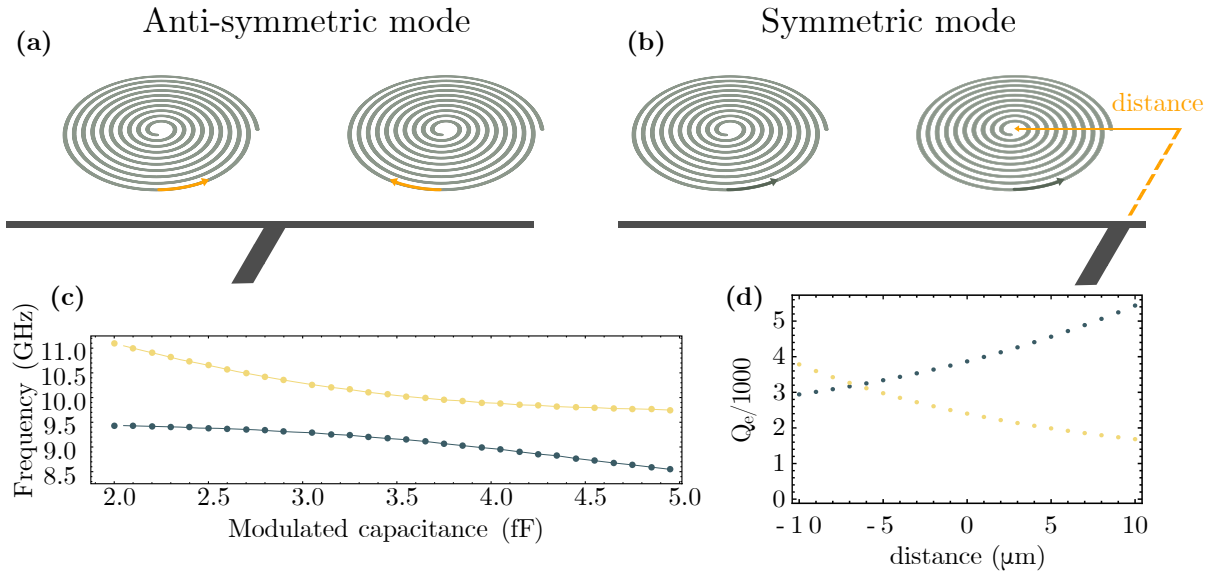
Figure 2.3: **Coil-coil coupling.** (a) and (b) representation of the anti-symmetric and symmetric super modes. (c) Frequency of the two modes as a function of the ideal capacitance displaying an anticrossing. Square coil parameters used $p = 1\mu$m, $n = 30$, $d_{out} = 62\ \mu m \times 88\mu m$ and $p = 1\mu$m, $n = 44$, $d_{out} = 88\ \mu m \times 88\mu m$, distance between coils $2\ \mu m$, distance to waveguide from coil edge $3\ \mu m$, on SOI substrate. (d) Change in quality factor of the two super modes as a function of distance between the center of one of the coils and the symmetry point of the coupler wire. Asymmetry with respect to zero comes from the crosswire necessary to connect the coil center to the outer turns.

between the two modes changes as a function of the distance represented in (b). The external quality factor of the two collective modes will be a symmetric and anti-symmetric combination of the quality factors of the individual modes. The point in the plot where the two modes have the same external quality factor arises when one of the coils is placed at the symmetry point with of the coupler wire and therefore both collective modes couple to the system through the other coil.

2.2.4 SPURIOUS MODE SIMULATIONS

Finally a 3D finite element simulator is used to extract the frequency dependent admittance $Y(f)$ of different coil geometries. The admittance is useful to understand how the circuit acts as a function of frequency, for example to understand the limitations of an LC circuit approximation. The simulation places a lumped port where the ideal capacitance was placed in Fig. 2.1 from which an excitation is sent. The location of the port coincides with the location of the Josephson junction for the Fluxonium qubit and this method is mostly used to predict the position of spurious modes of the coil.

Figure 2.4 shows a typical simulation of the admittance of a coil. The frequency marked as f_0 is the fundamental frequency of the coil given by it's capacitance and inductance. At higher frequency the coil admittance deviates from that of an LC circuit due to the appearance of poles. Each shaded section in the plot can be described by the circuit within it, for every new pole that appears an additional series LC circuit must be added in parallel to the original circuit in order to model it accurately at such frequencies. This simulation confirms the validity of the LC approximation up to around 13 GHz, far beyond the coil's self resonance frequency.

2.3 CHIP FABRICATION

The devices presented in this work follow 4 recipes the result of which can be seen in Fig. 2.5. Three recipes are for coil devices where planar coils are measured as resonators on different types of substrates while the remaining recipe is for samples that include coils
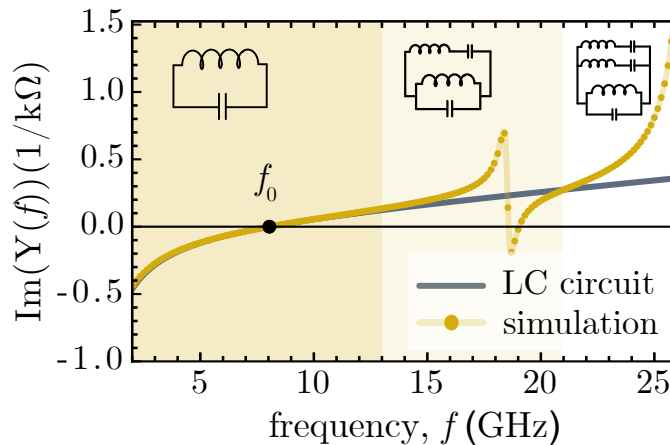
Figure 2.4: **Spurious mode simulations** Plot of a simulation of the admittance of a coil done with a 3D finite element simulator. Coil parameters $p = 1\,\mu$m, $n = 60$, $d_{out} = 132\,\mu m$ in vacuum. The yellow dots represent simulated points while the gray line is the expected admittance of an LC circuit. Up to a certain frequency the two are in agreement because the coil simulation displays a series of poles which can be modelled with the circuits shown in the different shaded sections.

and Josephson junctions. The two chips in the *Device chips* category in Fig. 2.5 follow the same recipe as they have the same components albeit in different order.

2.3.1 COIL ONLY DEVICES

The first row in Fig. 2.5 shows the different kind of chips that were fabricated to test planar inductor (coil) resonators. Because these coils are all open there is no need to create an air-bridge or crossover as for the other chips. For these implementations the metal is all deposited in one layer, the main difference lies in the substrate.

The three substrates are a silicon wafer (Si), 220 nm silicon membrane separated from a silicon handle wafer by $3\,\mu$m of vacuum (Silicon on insulator or SOI), and a fully suspended 220 nm silicon membrane (SOI Backetched). On silicon the fabrication is a simple one layer process on a high resistivity silicon wafer. The coil, ground and waveguide are patterned with e-beam lithography then the aluminum is deposited via evaporation.

The SOI fabrication is done on a wafer consisting of 220 nm of silicon, $3\,\mu$m of silicon dioxide (SiO_2) which rests on 750 μm of silicon. In the first step ebeam lithography is

Coil only chips

Coil on Si

Coil on SOI

Coil on SOI-BE

Device chips

Coulomb blockade chip

Fluxonium chip
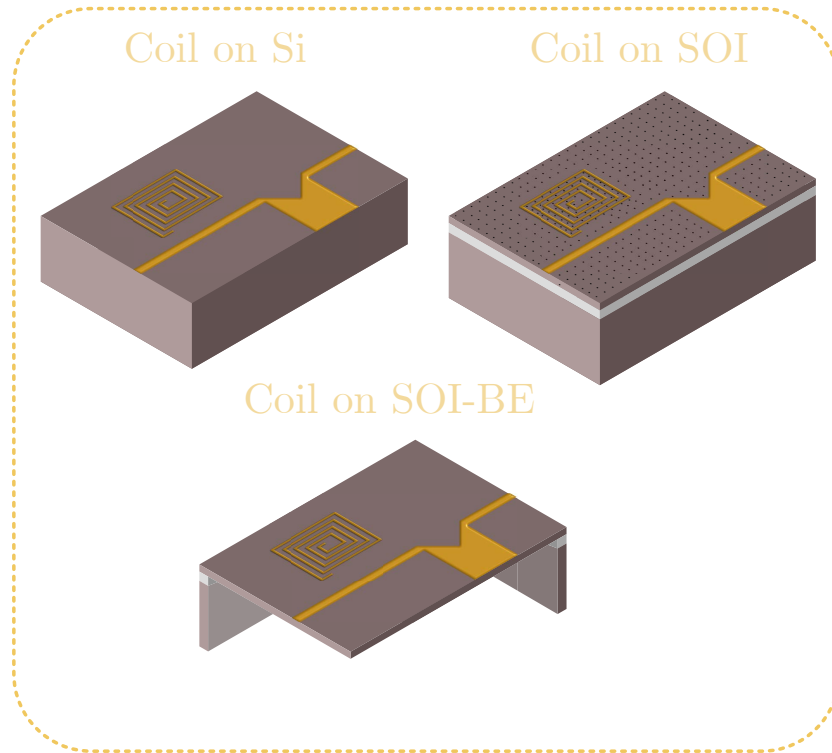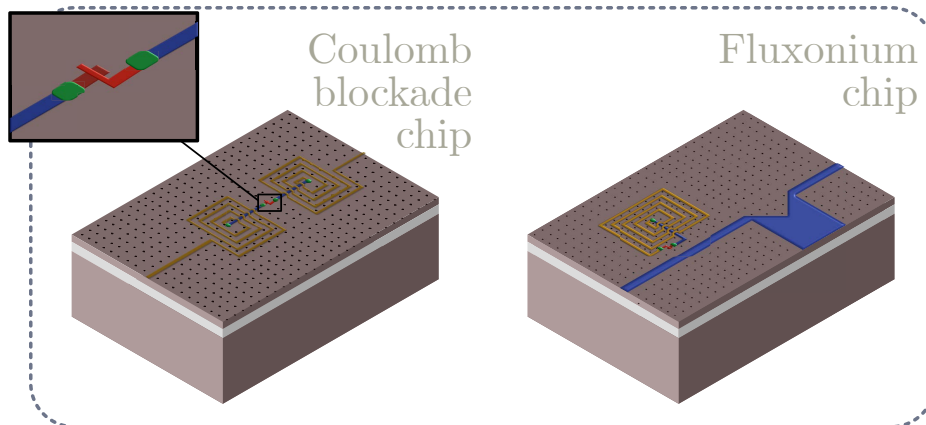
Figure 2.5: **Sample types and fabrication.** Simplified cartoons of the types of samples presented in this work. The first row represent the samples fabricated for the classification of geometric superinductors. The second row are devices used for other experiments, namely measurement of fluxonium qubits and of Coulomb blockade. Inset of the Coulomb blockade chip shows the Josephson junction (red) and bandaids (green). Different colors represent metal deposited on different layers.

used to pattern small holes (radius 65-100 nm) on the thin silicon layer around the coil and on the waveguide, the chip is then placed in an ICP where C_4F_8 etches the holes through the silicon layer reaching the oxide. Then the coil is patterned and evaporated as in the previous case and finally the sample is placed in HF vapour. In this final step the vapour penetrates through the etched holes and removes the oxide leaving a suspended membrane in the desired places.

Lastly for the SOI backetch the starting chip is composed of a 220 nm silicon layer, 3 μm of SiO_2 and 200 μm of silicon. The first two steps are identical to the SOI chip. After the coils have been deposited a thick layer of protective resist (LOR) is placed on the structures and the chip is then flipped. A mask is written on the back side of the chip and 50 nm of cromium are deposited, leaving open rectangles directly under the coil. The chip is then placed in an ICP with the devices facing down and the silicon in the rectangle is completely etched away with a customized Bosch process using C_4F_8 and SF_6, leaving only the SiO_2 and the 220nm silicon layer under the coils. The resist is then removed and the chip is placed again in vapour HF. Finally the coils are left suspended on a 220 nm membrane with nothing below.

2.3.2 COIL AND JOSEPHSON JUNCTION DEVICES

The device chips are all fabricated on SOI. The first layers follow the coil on SOI recipe with the holes and deposition of the ground plane (for the fluxonium qubit) or connecting wires (for the Coulomb blockade chip). In addition the crosswire of the coil (blue in Fig. 2.5) is deposited in this layer. Subsequently a double layer of LOR and PMMA is spun on the sample and squares of around 300 μm x 450 μm are patterned around the coil with the exception of a rectangle above the crosswire. This has the aim to create a mask of PMMA above the LOR, a photoresist that isn't affected by the electron beam. The chip is then subjected to a wet etch in MIF319 where the exposed LOR is removed. Upon removing the leftover PMMA a rectangle of LOR remains above the crosswire. In order to round the corners of the rectangle a reflow process is performed by heating the chip to 200 °C for 11 minutes on a hot plate. The coil is then written and deposited such that the wires are arched above the crosswire. A liftoff process in NMP then removes the LOR leaving the airbridges suspended. In the subsequent layer the Josephson junction is deposited

with a Dolan bridge technique [Dolan, 1977] and finally the bandaid layer is carried out. The bandaids are necessary to connect metals deposited in different layers. Because of Aluminum's short oxidation time [Krueger, 1972] soon after the metal is exposed to air a layer of aluminum oxide is formed on the surface, this means that different metal pieces will have very bad electrical contact. In the bandaid layer e-beam lithography is used to write squares in the areas where different layers overlap (see the green parts in the inset of Fig. 2.5) then before metal is deposited an ion beam of argon ions is applied to remove the oxidized Al in ultra high vacuum. Then new Al is deposited on the exposed metal creating a direct electrical contact. Finally the sample is placed in vapour HF to remove the oxide and suspend the membrane.

More detailed recipies can be found in Appendix A.

2.4 DC SETUP

DC measurements presented in this work were performed at the mixing chamber stage of a Blufors LD250 dilution refrigerator (base temperature around 10 mK). This stage can be accessed via 24 inbuilt lines running from room temperature to the stage in twisted pairs.

The voltage and current signals are generated by a low noise IVVI rack developed by Raymond Schouten in Delft[1]. Specifically voltage is sourced by the *S2f* module or the *S3b* module when lower voltages were needed and current is sourced from the *S4m* module with range going down to 1 nA. To read-out voltage the signal is passed to a *M2m* amplifier module where the amplification can be selected between 1 and 10^4 while a current signal is sent to a *M1b* current to voltage converter module where the resistance goes from 10 MΩ to 1 GΩ. Both these modules output voltage signal high enough to be measured with a multimeter. These two measurement modules are internally connected to a *M0* which has a BNC output which is connected to a Keysight P9373A multimeter.

---

[1]http://qtwork.tudelft.nl/ schouten/ivvi/index-ivvi.htm

(a) source current   **(b)** source voltage
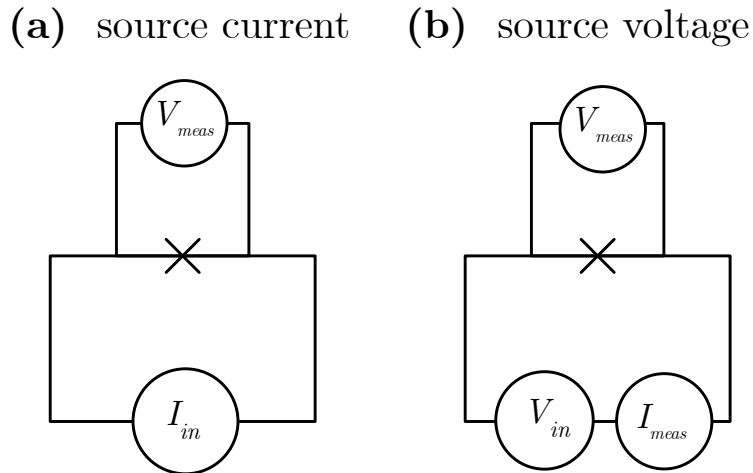
Figure 2.6: **DC measurement techniques.** (a) 4 probe measurement scheme for current sourced Josephson junction measurements. (b) 4 probe measurement scheme for voltage sourced Josephson junction measurements

2.4.1 MEASUREMENT TECHNIQUES FOR DIRECT CURRENT MEASURE-MENT

When measuring the IV curve we can use two methods, current driven and voltage driven. For a current driven measurement a current is sent through the sample and the voltage is collected across it. However this method will include all resistances that occur between the sample and the measurement setup. In our case this includes the resistance of the Blufors wires, the resistance of the filters and the on-chip or off-chip resistors.

These issues are circumvented by using the four probe approach. The idea is to split the *measurement* line and the *excitation* line as close as possible to the sample. This allows for the voltage and current lines to be independent and therefore the effect of the resistances is not included in the measurement. The typical 4-probe measurement includes exciting with a current I_{in} and measuring the voltage V_{meas} across the separate lines as seen in Fig. 2.6(a).

Alternatively the measurement can be done with a voltage excitation as seen in Fig. 2.6(b). For this configuration the voltage supply and the current measurement are in series. This uses only two of the probes, the remaining probes are used to measure the voltage applied across the junction $V_{JJ} = V_{meas}$. In fact the voltage sent will be changed by the line
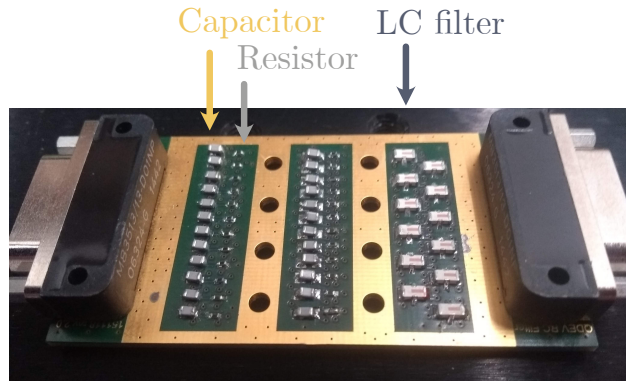
Figure 2.7: **DC low pass filters.** Picture of a low pass filter used for DC measurements consisting of two stages of RC filters and one stage of LC filters in series.

resistance R by $V_{JJ} = V_{in} - I_{meas}R$. If the resistance of the line (without the junction) is known through a reference measurement then the voltage at the junction can be calculated and the measurement can be done with only two probes.

2.4.2 SAMPLE HOLDER AND FILTERING

At the 10 mK stage the lines are connected to a filter which contains two RC filters and one LC filter in series. An image of a filter is shown in Fig. 2.7. The RC filters consist of film surface mount resistors from Susumu (s.n. RG1005P-9762-B) of the value of 96.7 kΩ and ceramic multilayer capacitors from Murata (s.n. GRM2195C1H103JA01J) of the value of 10 nF. These result in a cutoff frequency of 163Hz. In addition to two repetitions of the RC filter, each line also incorporated an LC filter with a cutoff of 80 MHz at room temperature. This part is added to strengthen the filtering of higher frequency where the RC components might fail. All lines connected to the sample went through the filter box meaning that the total resistance of a voltage or current measurement would be **390 kΩ** at room temperature, the value went up to **425 kΩ** when the fridge was at base temperature. This type of filtering however fails at higher frequencies (> 10 GHz), in order to extend the range of the filtering 12 thermocoax lines were also implemented in the setup.

2.5 RF SETUP

Measurements done at high frequency (4-12 GHz) were performed in the same dilution refrigerator at around 10 mK.

2.5.1 PACKAGING

Samples are mounted in a sample box made out of oxygen-free high conductivity copper shown in Fig. 2.8(a-b). The box is closed by a lid in order to shield from external RF radiation. The chip is placed carefully on a PCB where 4 MMPX connectors are surface mount soldered to 50 Ω coplanar wave transmission lines that extend to the edge of the chip. Aluminum bond wires connect the chip ground to the PCB ground and the center wire of the PCB transmission lines is bonded to the devices, an example is shown in Fig. 2.8(c). Finally to guarantee that the bonds are successful the resistance between center conductor and ground of the MMPX connector is measured. In most of the samples the waveguide is shorted near the device for inductive coupling, this indicates that the resistance measurement will result in a resistance of 50-100 Ω. However it is important to distinguish a working device from a device where the center wire is shorted to the ground on the PCB, something that can occur because of misplaced bonds or solder. This results in a resistance to ground below 10 Ω. Finally the box is thermally anchored to the 10 mK stage of the dilution refrigerator as shown in Fig. 2.8(c).

2.5.2 LOW TEMPERATURE SETUP AND FILTERING

When measuring at low temperatures it is important that the signals reaching the samples are well thermalized with the temperature of the fridge stage. As all signals are sent from room temperature they come with room temperature Johnson-Nyquist noise. For this reason all signals coming in are heavily attenuated. The low temperature setup shown in Fig. 2.9 displays a total of 50 dB attenuation distributed across three stages. 50 dB is enough to remove room temperature noise, however the cables increase the total attenu-
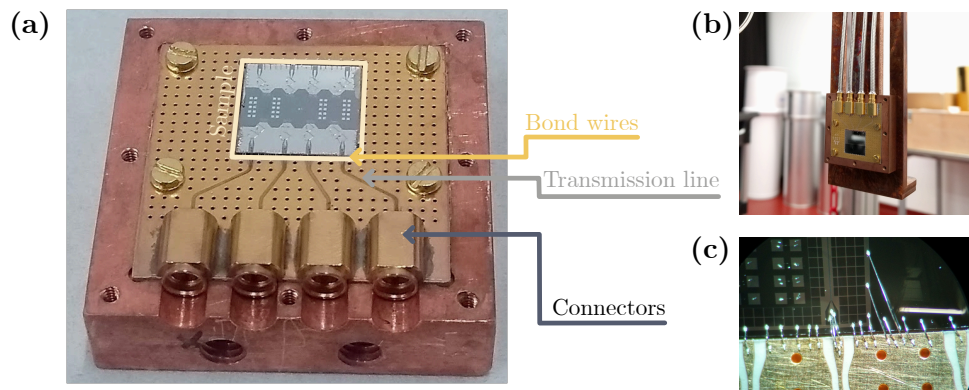
Figure 2.8: **Copper box, PCB and sample.** (a) Picture of the bottom part of the copper box. RF connector, PCB transmission lines and position of bond wires are highlighted. The box is then closed with a copper lid to avoid stray RF radiation. (b) Bottom part of the PCB mounted on a copper cold finger thermally anchored to the 10 mK stage of the dilution refrigerator. (b) Close up of bonds connecting the PCB to the sample.

ation to approximately 70 dB which becomes 83 dB when the room temperature cables are included. Attenuations reported are for around 8 GHz and decrease with increasing frequency with a total variation of 10 dB across the 4-12 GHz range.

The attenuators are distributed across several stages as they dissipate the signal to the ground, were they all placed on the 10 mK stage they would risk causing heating for particularly high power signals. Each component will add noise at the temperature it is thermalized to making it crucial to have sufficient attenuation at the 10 mK stage.

In addition to being attenuated the input lines are heavily filtered for signals outside of the measurement band. The measurements were done in two measurement bands, 4-8 GHz and 8-12 GHz, on two separate lines. Both lines have the same configuration of filters and attenuators with the difference being the filtering band.

Commercial microwave filters however only work up to a certain frequency and are ineffective above approximately 50 GHz. This is important because photons at these frequencies have enough energy to break Cooper pairs and hence can be very detrimental to the quality factor of superconducting circuits. Materials such as Eccosorb and Stycast filter at these frequencies [Halpern, 1986] and therefore Eccosorb filters and Stycast shielding were added. Once the incoming signal passes the first round of filtering it reaches a circulator. This element is crucial in order to separate incoming signals from outgoing ones, it works similar to a roundabout with three exits. It's presence means a wave coming from the
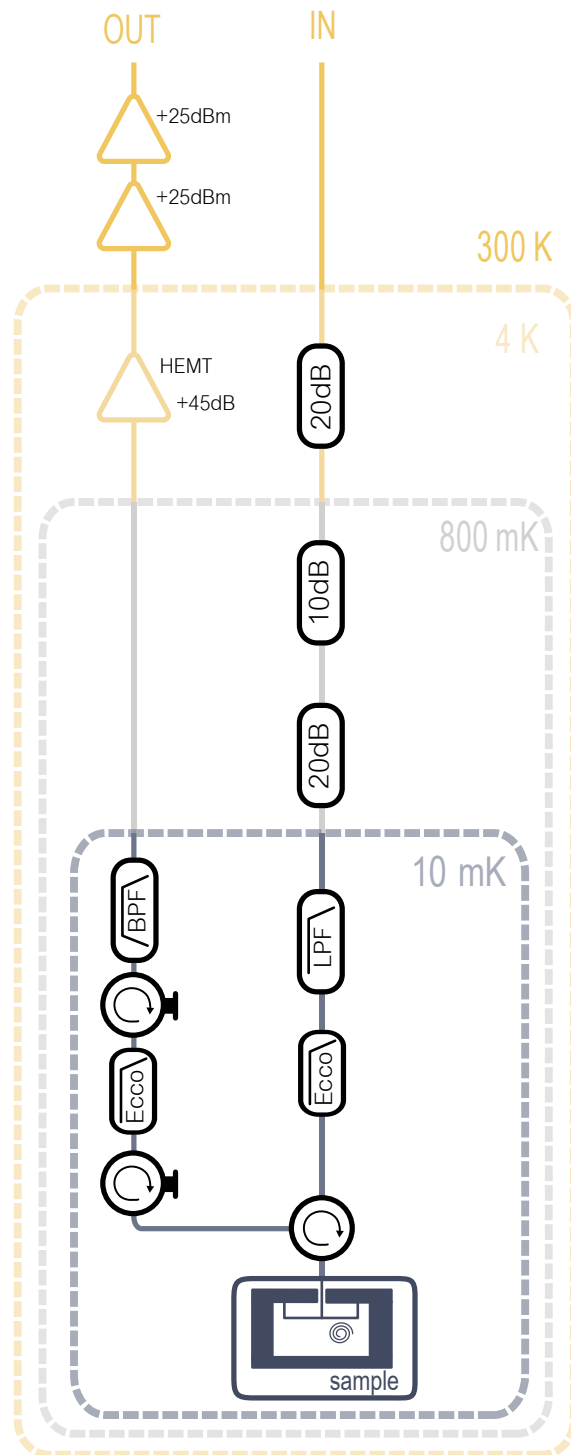
Figure 2.9: **Low temperature measurement setup.** Scheme of an input-output line used to conduct low temperature RF measurements. The boxes labelled with 10 (20) dB represent attenuators while the remaining boxes represent bandpass (BPF), lowpass (LPF) and Eccosorb (Ecco) filters. The circles with the curved arrows represent circulators. The triangles represent amplifiers. The setup is designed for reflection measurements.

input line goes to the sample, a wave coming from the sample goes to the output line and noise coming from the output line goes to a termination and is not sent back to the sample. This last step is crucial as the signal amplifier emits noise with a temperature of at least 4K. Only two circulators are strictly necessary and the third one is added for additional isolation, which amounts to 25 dB per circulator.

From the circulator the signal reaches a 6 port coaxial switch by Radiall. This is an element that allows for the signal to be redirected to six different lines and hence has the potential to measure six samples in a single cooldown.

From the switch the signal is sent directly to the sample where it interacts with the circuitry and then is reflected back. When approaching the circulators it is directed to the output line but not before another round of filtering. Specifically these filters are to avoid noise coming from the output line which is not attenuated as the input lines.

The 10 mK stage is connected to a low noise High Electron Mobility Transistor (HEMT) amplifier on the 4 K stage by one long superconducting cable. This allows for minimal signal loss before the amplifier. It is very important that as little of the signal as possible is lost between the sample and the HEMT in order to have a good signal to noise ratio. The reason is that often measurements are done at single photon equivalent powers while the HEMT adds 7-10 photons of noise.

After the amplifier the signal reaches room temperature undisturbed. At this point the signal has been amplified by 40 dB which means cable losses are much less critical.

Finally a word must be spent on the cable materials. Part of the method that the fridge uses to reach the low temperatures in to have very low thermal conductivity between stages. For this reason cables that connect different stages are made of Stainless Steel with the exception of the ouput cable connecting the to 50 K stage to RT which is made out of Beryllium Copper and Stainless Steel. Cables that connect objects on the 10 mK stage must have high thermal conductivity in order to thermalize all devices to the stage temperature and low loss to maintain high signal to noise ratio. Therefore all cables connecting samples and filters are made out of copper and additional thermal anchoring is added to pieces of equipment where signal is dissipated (i.e. attenuators, circulators and filters).

2.5.3 ROOM TEMPERATURE RF SETUP

The room temperature setup is designed in order to allow for switching between different types of measurements with minimal effort from the user. The two input lines were designed in a similar way. The 8-12 GHz line includes an additional switch with the option to route the outbound signal to a spectrum analyzer which is not present in the other line.

The incoming and outgoing signals are routed through a board (shown in Fig. 2.10) and are directed by room temperature switches. The board allows for the following measurements:

VNA measurements: in the case of all switches being set to 0 a signal enters by VNA IN and goes directly to the fridge. The outcoming signal is then directed to the VNA OUT port. The RF line also has a direct pathway to the fridge input and is used in spectroscopy measurements for excitation signals. This measurement method is used for resonator characterization and continuous wave qubit spectroscopy.

Digitizer measurements: Here the input lines are the RF and SPEC ports, connected to microwave sources. The SPEC port has the option to go directly into the fridge or to pass through an upconversion IQ mixer where it can be mixed with an AWG signal. The output signal is then routed to the downconversion mixer where it is mixed with the LO source. The I port is terminated and the signal going through the Q port is amplified and sent to the digitizer. This measurement method is used mostly for time domain qubit measurements.

Calibration measurement: In this configuration the signal avoids the fridge and goes through upconversion then downconversion and is detected by the digitizer. This mode is useful for visualizing the signals that are sent in the fridge and for calibration of the upconversion IQ mixer.

2.5.4 MEASUREMENT TECHNIQUES FOR QUBITS AND RESONATORS

Resonator characterization measurements

Resonator measurements reported in this work are done exclusively with a VNA. This is because the VNA allows to measure both phase and amplitude of the signal by mixing it
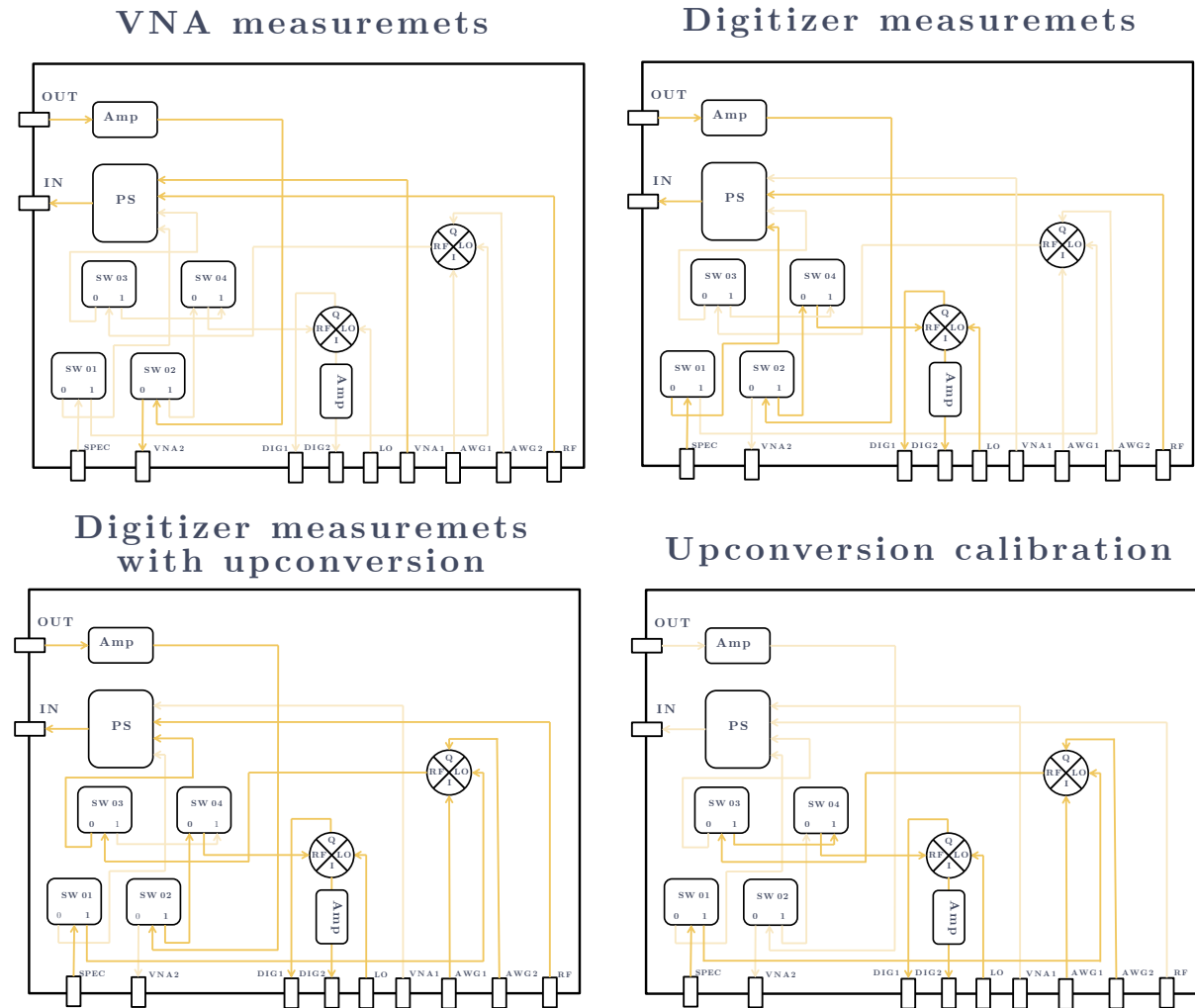
Figure 2.10: **Room temperature setup.** Visualization of the room temperature down conversion board with the paths for different types of measurements highlighted. Boxes named SW are switches, boxes named PS are power splitters, circles are IQ mixers.

with the outgoing signal.

In order to characterize a resonator the real and imaginary components of S_{11} (I and Q) are measured as a function of frequency. The majority of measurements are done in reflection and the S_{11} parameter was fitted to the function [Gao, 2008a]

$$S_{11} = A_0 e^{-i(\phi + 2\pi\nu\tau)}\left(1 - \frac{2Q_i - 2iQ_iQ_e\delta\nu/\nu_0}{(Q_i + Q_e) + 2iQ_iQ_e(\nu - \nu_0)/\nu_0}\right). \tag{2.2}$$

The equation is more complicated than a simple Lorentzian shape to include for our measurement conditions. The parameters in Eq. 2.2 are the following:

A_0 is the dimensionless measurement baseline given by attenuation and amplification

ϕ is a constant phase offset

ν is frequency

τ is a time constant meant to correct for a frequency dependent phase offset accumulated through the coaxial cables

Q_e, Q_i are the external and internal quality factors

ν_0 is the resonance frequency of the resonator

$\delta\nu$ is an asymmetry factor to fit resonators with an asymmetric/fano linewidth [Fano, 1961]. These are often due to interferences caused by experimental imperfections or asymmetries in the feedline circuit.

2.5.5 QUBIT CHARACTERIZATION MEASUREMENTS

This chapter will include a step-by-step procedure that allows to fully characterize a qubit coupled to a resonator. This includes measurement of qubit transition frequencies and coherence times performed on transmon qubits. The methods are independent on the specific qubit type and were used on the RF-SQUID qubits presented in later chapters.

Resonator characterization

A resonator coupled to a qubit will experience a shift χ in frequency according to the state of the qubit [Wallraff, 2005; Schuster, 2007; Bianchetti, 2009]. This shift is present when the cavity is being measured with a number of photons below a critical photon number [Blais, 2021]. When the critical photon number is surpassed the cavity+qubit system reaches a state of bistability. At very high photon numbers the effect of the qubit is no
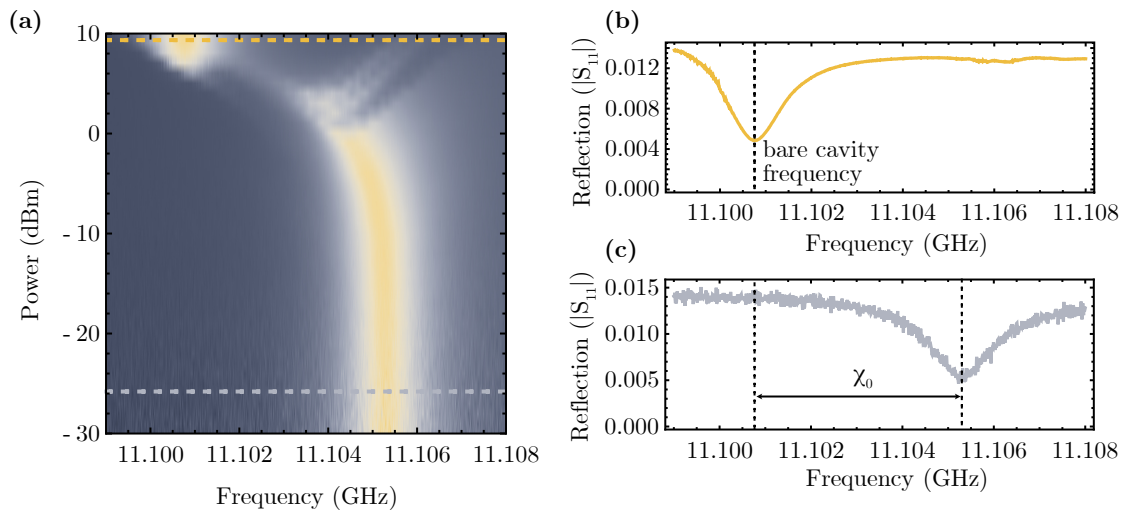
Figure 2.11: **Resonator vs. power.** (a) 2D plot of reflection amplitude vs. frequency measured with the VNA for different measurement powers. (b) and (c) Traces at low and high power showing the cavity frequency when the qubit is in the ground state and the bare frequency of the two cavities corresponding to the gray and yellow dashed lines in (a). The difference between the two frequencies is identified as χ_0.

longer felt by the resonator and the resonance is therefore at the cavity bare frequency. This process can be followed in a cavity trace vs power measurement that can be done with a VNA in Fig. 2.11.

The difference in resonance frequency between the high power and low power measurements reveals χ_0. In the case of tunable qubits (such as a fluxonium with a flux bias) χ_0 vs flux can be obtained by measuring a frequency trace vs flux.

Two tone continuous wave spectroscopy

The cavity trace vs flux might show a series of anti-crossings due to a qubit level crossing the resonator frequency. In this flux range the qubit-resonator interaction can be described as a direct interaction that allows energy exchange. Once the qubit is detuned far enough from the resonator the measurement of it's frequency must be done dispersively. Figure 2.12 shows the shift in the cavity as a function of qubit drive frequency when such drive is continuously applied. When the drive resonates with the qubit transition the qubit is placed in a mixed state resulting in a resonator shift of $\chi_{01}/2 = (\chi_1 - \chi_0)/2$. The magnitude of the shifts need to predicted by taking into account the qubit parameters and the magnitude and type of coupling (inductive or capacitive) [Zhu, 2013] and are
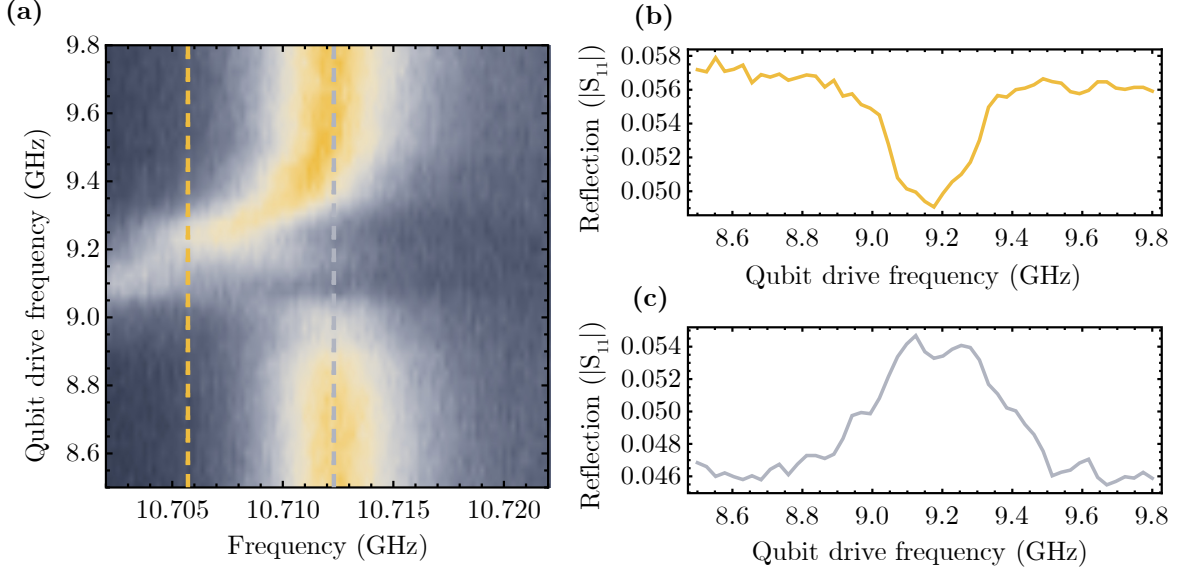
Figure 2.12: **Resonator shift due to qubit excitation.** (a) 2D measurement of a resonator trace vs qubit drive frequency done with a VNA. Around the frequency of the qubit the resonator shifts in resonance allowing to measure the qubit state by measuring the change in resonator reflection. (b) and (c) Two traces corresponding to the dashed lines on the 2D plot showing the peak that corresponds to the qubit frequency. The two traces represent the positions of best signal to noise ratio for the measurement.

given by

$$\chi_\alpha^C = \frac{1}{h} g_C^2 \sum_{\beta \neq \alpha} |\hat{n}_{\alpha\beta}|^2 \frac{2E_{\alpha\beta}}{E_{\alpha\beta}^2 - \hbar\omega_R} \tag{2.3}$$

for capacitive coupling and

$$\chi_\alpha^L = \frac{1}{h} g_L^2 \sum_{\beta \neq \alpha} |\hat{\phi}_{\alpha\beta}|^2 \frac{2\hbar\omega_R}{E_{\alpha\beta}^2 - \hbar\omega_R} \tag{2.4}$$

for inductive coupling. g_C (g_L) is the capacitive (inductive) coupling constant, $|\hat{n}_{\alpha\beta}| = |\langle 0|\hat{n}|1\rangle|$ is the charge number matrix element, $|\hat{\phi}_{\alpha\beta}| = |\langle 0|\hat{\phi}|1\rangle|$ is the phase matrix element and $E_{\alpha\beta} = E_\alpha - E_\beta$ is the difference in energy between two given qubit states and ω_R is the angular frequency of the resonator.

Rabi measurement and Chevron pattern

An important aspect of qubit characterization is to measure its time domain properties, this includes coherence and energy relaxation time.

As these values can be below $1\,\mu s$ the measurement setup must have a fast sampling rate. In the case of the data in this work an Alazar ATS9870 digitizer was used which has a

sampling rate up to 1 Gigasamples/s corresponding to resolution of 1 ns.

Qubit measurements in time domain described in this work are measured by applying an excitation pulse which moves the qubit state to the desired state on the Bloch sphere then sending a second pulse at the cavity resonance frequency ν_{res}. This second pulse is mixed with an local oscillator with frequency ν_{LO} resulting in a signal at frequency $\nu_{if} = \nu_{res} - \nu_{LO}$ which the digitizer can acquire (up to 500 MHz). The signal is recorded by the digitizer and then digitally downconverted to extract the time dependent quadratures, I and Q. The intermediate frequency becomes the measurement bandwidth unless additional digital filters are applied.

A high bandwidth is required for small time resolution therefore the noise in the data must be reduced by making many averages (a typical measurement would include 10k+) which requires excellent timing between all instruments over long stretches of time. In order for this to be achieved all instruments are synchronized to a rubidium clock and triggered by a delay generator with accuracy below 25 ps.

A Rabi measurement is executed by sending a drive pulse addressing the qubit and measuring the resonator response with a second pulse. This is repeated for increasing drive pulse length, a scheme of the pulse sequence is seen in Fig. 2.13(b). The drive pulse, if resonant with the qubit, will rotate the qubit state around the x,y axis of the Bloch sphere at a rate Ω_R resulting in an exponentially decaying cosine function [Wallraff, 2005; Bianchetti, 2009]. A typical trace is displayed in Fig. 2.13(c). The decay over time for high drive fields ($\Omega_R \gg 1/T_1, 1/T_2$) is due both to qubit relaxation T_1 and dephasing T_ϕ and is given by [Bianchetti, 2009]

$$1/T_{\mathrm{Rabi}} = (3/T_1 + 2/T_\phi)/4. \tag{2.5}$$

The frequency Ω_R of Rabi oscillations is proportional to drive amplitude and coupling strength. In addition to the rotation speed given by the drive the qubit will rotate around the z-axis of the Bloch sphere at a frequency corresponding to the detuning between the drive frequency and the qubit frequency. These two methods of rotation are what gives rise to the Chevron pattern when a Rabi measurement is done for different frequencies. Such measurement is shown in Fig. 2.13(a).

Doing such measurements is not particularly informative when it comes to extracting coherence times, however they reveal the length of a π pulse for a given power and detuning
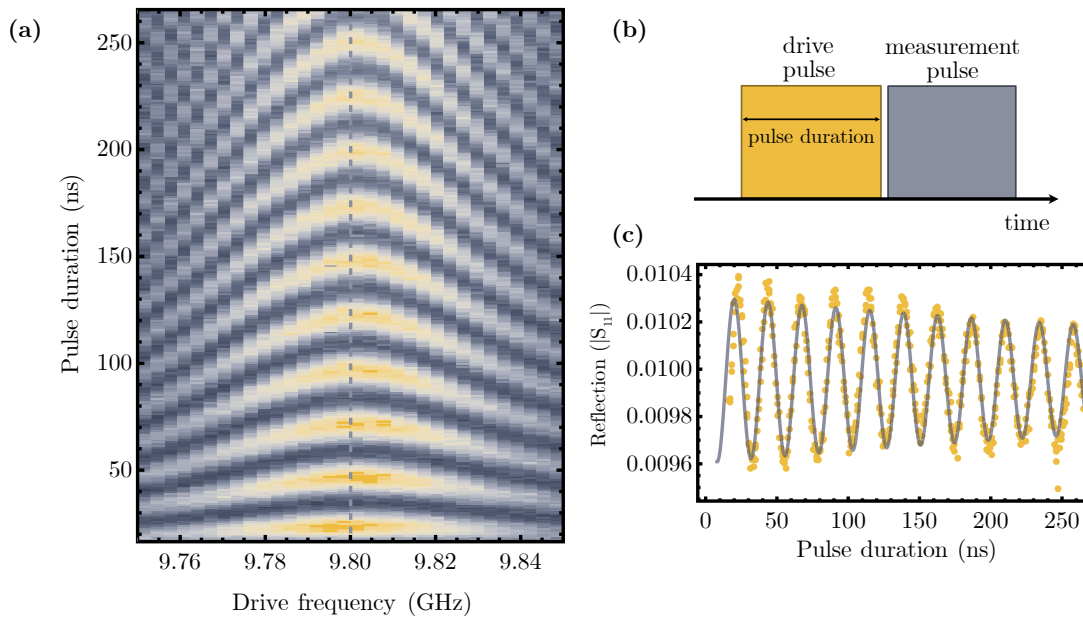
Figure 2.13: **Rabi measurement and Chevron pattern.** (a) Chevron pattern measurement, i.e. a series of Rabi measurements done for different drive frequencies. When the drive frequency corresponds to the qubit transition the rotation frequency is given solely by the coupling and drive amplitude. As the frequency changes the rotation increases in frequency. (b) Scheme of the pulses used. (c) A single Rabi sweep taken at the qubit resonance (see dashed line in Chevron pattern) showing the Rabi oscillation and the fit function.

(i.e. the pulse length and power that will take the qubit state to $|1\rangle$ on the Bloch sphere making it rotate by an angle of π).

Relaxation measurement

The measurement to extract the relaxation time consists of initializing the qubit state to $|1\rangle$ with a π pulse and measuring it after a wait time. The qubit excitation vs. wait time follows an exponential decay where the decay rate is T_1 i.e. the relaxation rate [Wallraff, 2005].

Ramsey measurement

A similar measurement is done in order to quantify T_2. However to measure the coherence the qubit is left in it's superposition state $(|0\rangle + |1\rangle)/\sqrt{2}$. This is achieved by applying a $\pi/2$ pulse which places the qubit state on the equator of the Bloch sphere. After a wait time a second $\pi/2$ pulse is applied which, if the qubit has not lost coherence, will bring the qubit state to $|1\rangle$.
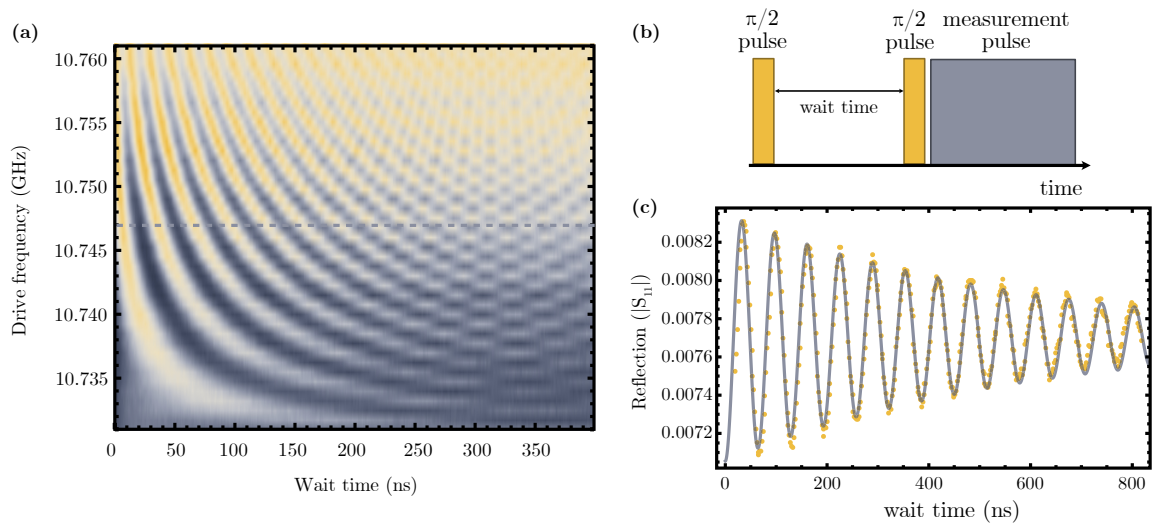
Figure 2.14: **Coherence measurement** (a) A Ramsey measurement as a function of detuning. Unlike in the Chevron pattern displayed in Fig. 2.13(a) the frequency of a Ramsey measurement is directly the detuning between the drive pulse frequency and the qubit transition. (b) Scheme of the pulse sequence used for a Ramsey measurement. (c) Shows a single trace from the 2D plot (corresponding to the dashed line) where the oscillations and decay are visible.

If the excitation pulses are detuned from the qubit resonance frequency the qubit state will rotate around the equator and the measurement will result in an exponentially decaying cosine function. An example of the measurement is seen in Fig. 2.14 where (b) shows the pulse sequence and in (a) the Ramsey measurement is done as a function of drive frequency displaying an increase of the rotation frequency as the drive is detuned from the qubit. (c) shows a trace from the 2D measurement (dotted gray line) where the rotation around the z axis of the Bloch sphere and the exponential decay are visible.

Spin echo measurements

The coherence time T_2 is composed of two parts [Yan, 2013]

$$T_2 = (\frac{1}{2T_1} + \frac{1}{T_\phi})^{-1}, \tag{2.6}$$

indicating that there are two sources of decoherence: the relaxation time T_1 and the dephasing time T_ϕ. While relaxation is an irreversible process, dephasing in principle is not [Bylander, 2011]. Because of this fact the qubit dephasing can be reversed by reversing the qubit phase. A sketch of the pulse sequence and a representation of the effect of such a measurement can be seen in Fig. 2.15. (a) displays the pulses, the two $\pi/2$

(a)

X

$\pi/2$ pulse

$\pi/2$ pulse   measurement pulse

wait time

π pulse

Y

time

(b)

$|1\rangle$

$|1\rangle$

3. dephasing spreads qubit wavefunction

1. start in ground state
$|0\rangle$

2. apply $\pi/2$ in X $|0\rangle$

$|1\rangle$

4. apply π in Y

$|1\rangle$

6. final $\pi/2$ pulse brings qubit to excited state

5. dephasing direction is reversed

$|0\rangle$

$|0\rangle$
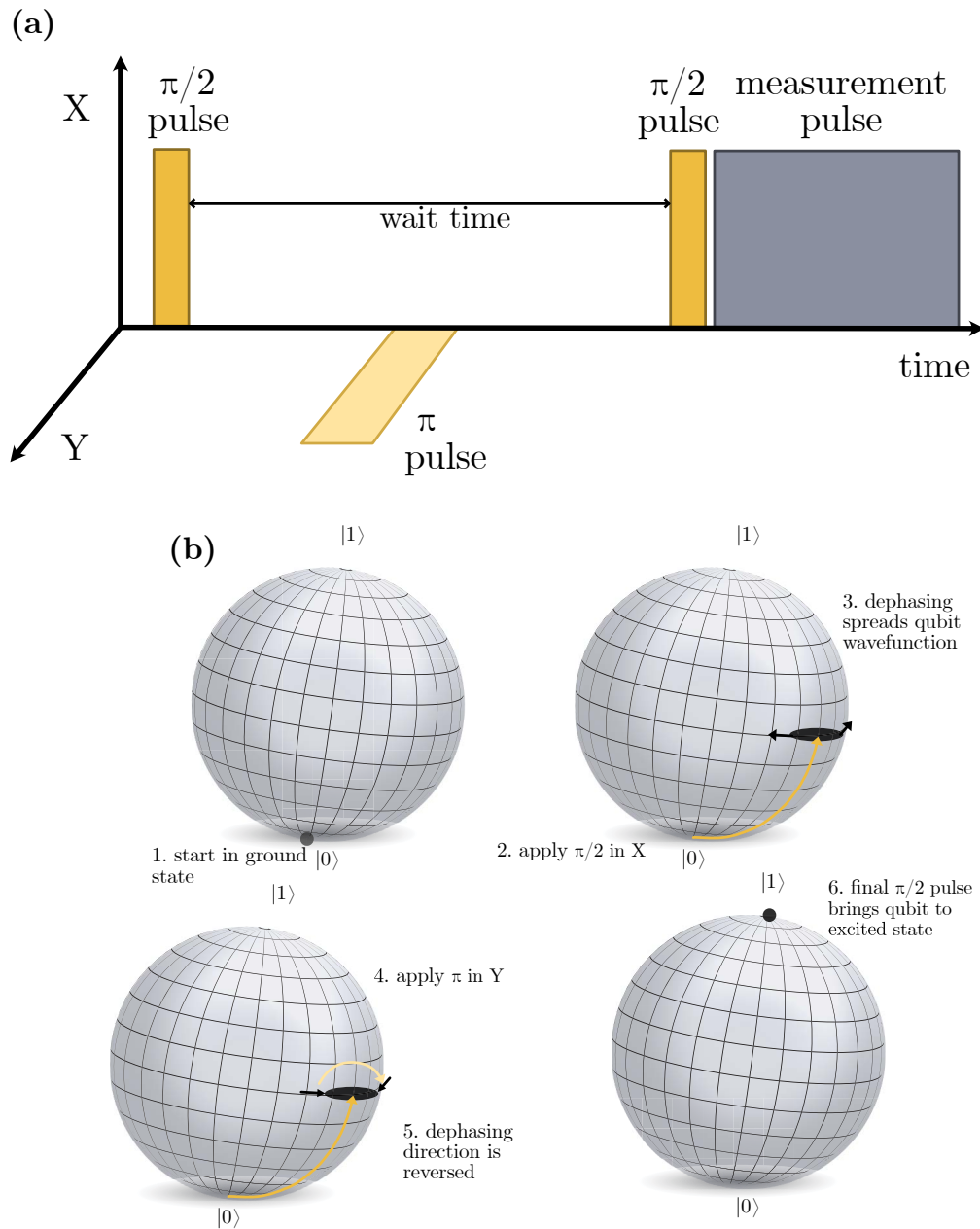
Figure 2.15: **Spin Echo measurement.** (a) Pulse sequence of a spin echo measurement where the π pulse and the $\pi/2$ pulses are different quadratures (X,Y). (b) a representation the evolution of the qubit state (black dot) on the Bloch sphere where the yellow arrows represent the trajectory taken when the pulses are applied. The black arrows indicate the direction of the dephasing which is inverted after the π pulse.

pulses are to be in a separate quadrature with respect to the π pulse. This guarantees that the $\pi/2$ and π pulses rotate the qubit around perpendicular axis. Figure 2.15(b) shows the evolution of the qubit state on Bloch sphere. The first pulse brings the qubit to the equator of the Bloch sphere where the wait time starts. The dephasing at this point begins spreading the qubit position, however once the phase of the qubit is rotated the direction of the spreading is also inverted bringing it to un-do the previous dephasing. This method applies a low pass frequency filter based on how many of the central pulses are applied [Bylander, 2011] allowing to remove more and more of the dephasing until the limit of $T_2 = 2T_1$ is reached.

CHAPTER 3

GEOMETRIC INDUCTOR CHARACTERIZATION

3.1 CHAPTER INTRO

This chapter discusses the measurement and analysis of planar coil resonators. The focus is on measurements done and trends that can be extracted from the data. The work in this chapter was done in collaboration with Andrea Trioni who helped develop the fabrication recipe and did the theoretical modelling. In addition Farid Hassani, Martin Žemlička and Mariia Labendik helped with simulations.

This chapter is based on the paper "Surpassing the resistance quantum with a geometric superinductor".

3.2 COIL MEASUREMENTS

This section will show experimental characterization of planar coils used as resonators. These were fabricated on Silicon, Silicon On Insulator (SOI) and Silicon On Insulator Backetched (SOI-BE). Fabrication steps are discussed in detail in Section 2.3 and Appendix A.

A total of 104 coils were measured in this manner and for each the resonance frequency was extracted by taking a frequency trace with a VNA which was then fitted to Eq. 2.2. The measurement was done as a function of probe power in order to track changes in quality factor and resonance frequency. Figure 3.1(a) shows an example of such a measurement and singles out three traces measured at different powers (b-d). The trace (b) shows a resonance dip distorted to a point where it is no longer in a Lorentzian shape illustrating the effect of the breakdown of superconductivity.

From the change in resonance frequency it is possible to extract the linearity of the resonator, defined as $\delta f_0/n_{\text{photons}}$. The average number of photons in the cavity n_{photons} is given by

$$n_{\text{photons}} = \frac{P_{in}}{h\nu} \frac{4\kappa_e}{(\kappa_i + \kappa_e)^2 + 4(\nu - f_0)^2},\tag{3.1}$$

where $\kappa_e = 2\pi f_0/Q_e$ and $\kappa_i = 2\pi f_0/Q_i$ are the external and internal linewidths of the resonator respectively and P_{in} is the power at the resonator input.
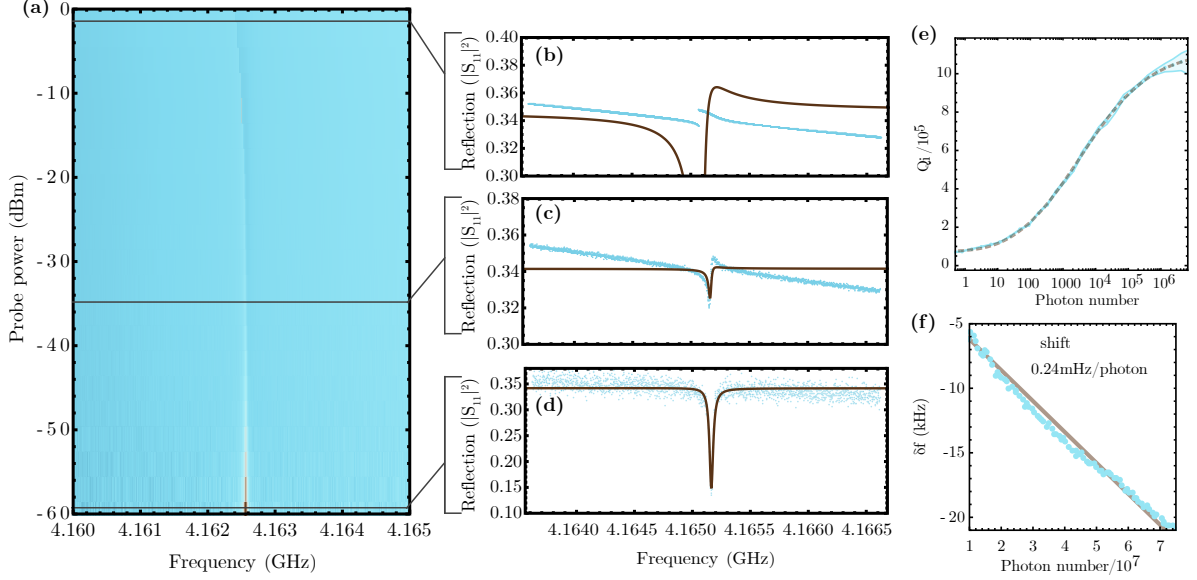
Figure 3.1: **Typical power sweep of a coil resonance.** (a) 2D plot of VNA traces vs source power. The data shows a high degree of linearity as the resonance frequency doesn't significantly change. (b-d) are three traces taken for different source powers. (d) shows the lowest Q_i due to the presence of Two Level Systems (TLS). At higher power, displayed in (c), the internal quality increases due to TLS saturation. In (b) the current in the coil is very high due to high probe power causing the beginning of the phase transition towards a normal metal which distorts the shape of the linewidth. The brown lines in the traces are fits to Eq. 2.2 with varying degree of accuracy. (e) is a plot showing the change in internal quality factor of a coil as a function of power. The brown line is a fit to a TLS model from Eq. 3.2. (f) Measurement of the change in frequency as a function of power fitted to a linear model where the gradient gives the linearity of the resonator. The plots in this column are not from the same coil as the rest of the plots in this figure. (a-d) coil parameters $n = 100$, $p = 0.3\mu m$, $d_{out} = 66~\mu m$ on Silicon, (e-f) coil parameters $n = 155$, $p = 0.3\mu m$, $d_{out} = 105~\mu m$ on SOI
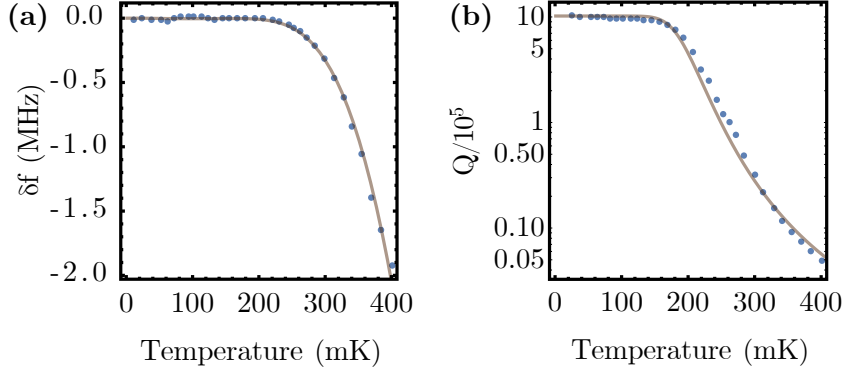
Figure 3.2: **Typical temperature sweep of a coil resonanace** Change in frequency (a) and quality factor (b) as a function of temperature. The fit lines are to Eqs. 3.3 and 3.4 respectively. Coil parameters $n = 155$, $p = 0.3\mu m$, $d_{out} = 105$ μm on SOI

The shift slightly varies between coils and is very challenging to measure as it is often obscured by the breakdown of the superconductor. Figure 3.1 (f) shows the change in resonance frequency as a function of photon number for an example coil, this was found to be 0.24 mHz per photon. Such a low non-linearity is unparallelled by other superinductors [Masluk, 2012; Maleeva, 2018; Niepce, 2019] and allows us to classify our coils as highly linear devices. The extracted non-linearity is representative in order of magnitude of the general non-linearity found in planar coils.

Figure 3.1(e) shows the internal quality factor (Q_i) as a function of power. The shape is consistent with losses due to two level systems (TLS). TLS can be due to surface defects or dangling surface bonds and are saturated at high probe powers. Consequently the fraction of photons absorbed by TLS decreases with increasing intra-cavity photon number increasing Q_i. The fit line in this plot is to the following TLS model [Gao, 2008a]

$$Q_{\mathrm{TLS}}^{-1} \simeq \frac{F\delta_{\mathrm{TLS}}\tanh(\hbar\omega/2k_{\mathrm{B}}T)}{(1 + n_{\mathrm{photons}}/n_{\mathrm{C}})^{\beta}} + Q_{\mathrm{sat}}^{-1}, \tag{3.2}$$

where F is the fraction of electric field in the lossy material, δ_{TLS} is the TLS loss tangent, n_{C} is the critical photon number needed to saturate the TLS, and Q_{sat} represents the losses due to the remaining loss mechanisms, such as quasiparticles or radiation, which for the shown sample is 1.1×10^{6}. The TLS loss tangent was found to be 1.3×10^{-5}.

While all coils were measured as a function of power only a couple were measured as a function of temperature. In fact when increasing the fridge temperature the resonance frequency and internal quality factor both decrease. This effect is due to the surface resistance and reactance of the superconductor which manifests as a temperature dependent

kinetic inductance due to surface effects.

The surface complex conductance governs the frequency and quality factor shifts as [Gao, 2008b]

$$\frac{\delta f(T)}{f} = -\frac{\alpha\gamma}{2}\frac{\delta\sigma_2(T,\Delta)}{\sigma_2(T,\Delta)}, \tag{3.3}$$

$$\delta Q^{-1}(T) = \alpha\gamma\frac{\delta\sigma_1(T,\Delta)}{\sigma_2(T,\Delta)}, \tag{3.4}$$

where $\alpha = L_k/(L_g + L_k)$ is the fraction the kinetic inductance L_k to total inductance $L_k + L_g$, γ is a material dependent variable which is -1 for aluminum thin films [Gao, 2008a], σ_1 and σ_2 are the real and imaginary part of the conductance $\sigma = \sigma_1 - i\sigma_2$ calculated as

$$\begin{aligned}\frac{\sigma_1}{\sigma_n} &= \frac{4\Delta}{hf}e^{-\frac{\Delta}{k_BT}}\sinh(\eta)K_0(\eta), \quad \eta = \frac{hf}{2k_BT}, \\ \frac{\sigma_2}{\sigma_n} &= \frac{\pi\Delta}{hf}[1 - 2e^{-\frac{\Delta}{k_BT}}e^{-\eta}I_0(\eta)],\end{aligned} \tag{3.5}$$

where σ_n is the normal conductivity, Δ is the gap energy, f is the resonance frequency and K_0 and I_0 are the 0th order modified Bessel functions of the first and second kind respectively [Gao, 2008b].

Figure 3.2 shows measurements of this effect. Fitting this data to Eqs. 3.3 and 3.4 allows to find α which in combination with the geometric inductance value calculated from Eq. 1.18 gives the value for the kinetic inductance L_k for the specific device. The kinetic inductance depends on wire length and cross section making it coil specific. More general is the London penetration depth, λ_L calculated as

$$L_k = \mu_0\lambda_L^2(0)\frac{l}{wh}, \tag{3.6}$$

where μ_0 is the vacuum permeability, and l, w and h are the length, width and thickness of the wire [Annunziata, 2010].

Applying this procedure to the data shown in Fig. 3.2 the penetration depth was extracted to be 147 nm. This number is much higher than the penetration depth of pure and bulk Aluminum [Gao, 2008a] due to the thin film nature of the metal [Reale, 1974]. In combination with the geometric parameters and Eq. 3.6 the penetration depth gives all the necessary information to extract the kinetic inductance of any coil.

Knowledge of the complex conductance allows one to calculate whether quasiparticles are limiting the internal quality factor. Even though the presence of thermal quasiparticles is expected to be exponentially suppressed at the fridge base temperature it was shown

[Visser, 2011] that the number of quasiparticles does not decrease with temperature below ~180 mK. Assuming this to be the quasiparticle temperature one can compute the expected quality factor $Q = \sigma_2(180 \text{ mK})/(\alpha\sigma_1(180 \text{ mK}))$ [Zemlicka, 2015] which gives a limitation of 2.5×10^6 for the coil in Fig. 3.1(e) and Fig. 3.2. This value being in the same order of magnitude as the fitted Q_{sat} indicates that out of equilibrium quasiparticles likely constitute one of the main loss mechanisms at high powers. Other loss mechanisms also expected to contribute are radiation loss and absorption from the copper box.

3.3 COIL RESULTS AND TRENDS

From each individual coil measurement it is possible to calculate kinetic and geometric inductance from Eqs. 3.6 and 1.18. The capacitance can then be retrieved by the LC oscillator resonance frequency formula:

$$\omega_{\text{LC}} = \frac{1}{\sqrt{LC}}. \tag{3.7}$$

In addition it is possible to calculate the characteristic impedance with

$$Z_{\text{C}} = \sqrt{\frac{L}{C}} = \omega_{LC}L. \tag{3.8}$$

Figure 3.3 shows the frequency and characteristic impedance of all measured coils. Points in (a-c) are given by fits to VNA measurements, in (d-f) they are calculated from the fundamental frequencies and Eqs. 3.6, 1.18 and 3.8. The fit lines are fits of the frequency data to Eq. 1.19 with the effective permittivity (ϵ_{eff}) being the only fit parameter. The fit lines to the characteristic impedance are calculated from the fit in the same way as the data.

Figure 3.4 displays calculated values of inductance and capacitance for the same devices reported in Fig. 3.3. The inductances (a-c) are calculated with Eqs. 3.6 and 1.18 while the capacitances (d-f) are extracted from the frequencies and the calculated inductances by using Eq. 3.7. As expected for $n \gg 1$ and fill-ratio $\rho \approx 1$ the capacitance is experimentally found to scale linearly with the outer radius of the coil ($C \propto r_{out} = r_{in} + np$). The data was therefore fitted to a linear model and the gradient extracted can be interpreted as the amount of capacitance that comes with adding a micron of radius to the coil. These
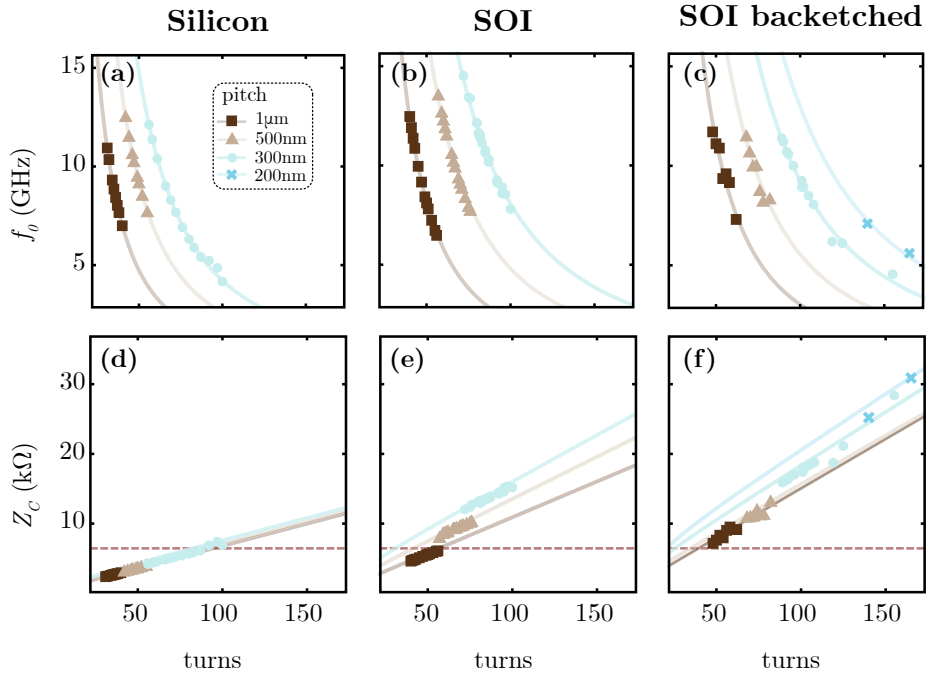
Figure 3.3: **Resonance frequency and impedance of planar resonators.** (a-c) measured resonance frequency of planar coils on the three substrates. Line fits are to Eq. 1.19 where the free parameter is the effective permittivity ϵ_{eff}. (d-f) Calculated impedance taken from the measured and fitted frequency data of the first row and the calculated inductance from Eqs. 1.18 and 3.6.
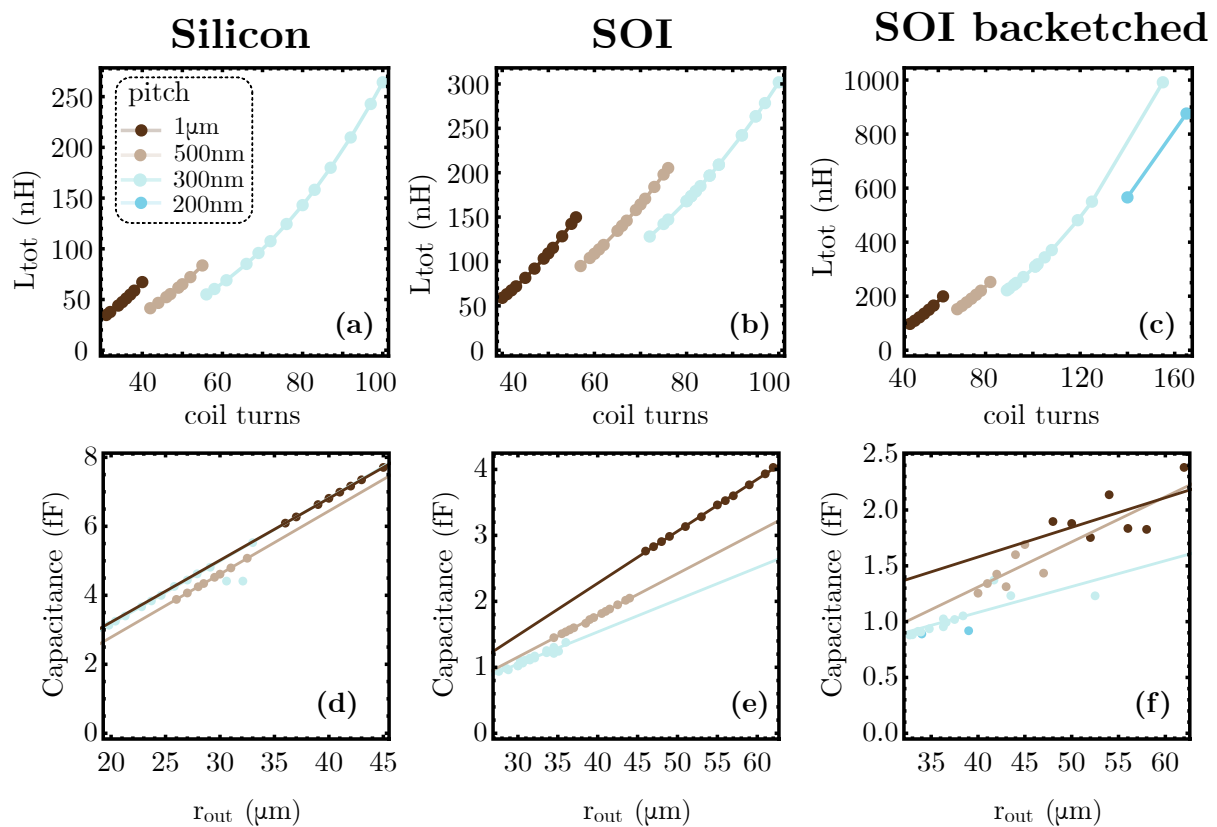
Figure 3.4: **Inductance and capacitance trends.** (a-c) Total calculated inductance taken from Eqs. 1.18 and 3.6. (d-f) Capacitance vs the coil outer radius r_{out}. The linear dependence is used to extract the capacitance per unit radius. The capacitance of the 200 nm pitch coil is not fitted to a linear model due to there only being two points.

values can be seen in Fig. 3.5(a). Figure 3.5(b) shows the extracted effective permittivity of the three substrates. The average values extracted are ϵ_{eff} of 6.89 ± 0.09 for silicon, 2.04 ± 0.93 for SOI and 1.25 ± 0.19 for SOI-BE. In the case of silicon ϵ_{eff} can be estimated with a simplified conformal mapping formula $\epsilon_{\text{eff}} = (\epsilon_{\text{Si}} + 1)/2 = 6.5$, very close to the fit results, and in the case of SOI-BE we find a value close to that of vacuum. The values of capacitance per μm of radius and effective permittivity for the SOI substrate exhibit a strong pitch dependence. The reason is that coils with higher pitch have larger size (as seen in Fig. 3.4(e)) and as a consequence a larger electric field distribution. Because SOI is not a homogeneous material, the higher the pitch the more electric field resides in the silicon handle wafer increasing ϵ_{eff}. This is the main reason for the large 90% confidence interval of ϵ_{eff}.

These numbers apply to any coil on a specific substrate which in turn allows to compare the efficiency of different substrates at decreasing stray capacitance. The steep decrease in both ϵ_{eff} and capacitance per μm between Silicon and SOI and subsequent saturation between SOI and SOI-BE should mimic the shape of the electric field in the vertical direction. This fact was additionally supported by a set of simulations showing the field distribution. This goes to show that the electric field is distributed around the coil structure and does not concentrate in the gaps between the coil turns which is also reflected in the relatively high internal quality factor suggesting a low amount of electric field focused on the interface.

Figure 3.5(c) shows the characteristic impedance for measured coils with similar fundamental frequency $f_0 = (10.7 \pm 0.3)\,\text{GHz}$. The superlinear improvement obtained by going to lower pitches occurs because fixing the frequency has the effect of fixing the wire length. For a set length, lower pitch coils have more turns, which gives higher inductance and smaller radii for lower parasitic capacitance. Both have the effect of boosting the characteristic impedance. The dashed lines represent analytical expressions derived from Eqs. 1.18, 3.6 and 1.19 and the bands correspond to the error of ϵ_{eff} as discussed earlier. In the case of SOI the ϵ_{eff} was interpolated between different pitches resulting in a slightly modified shape and a very small error band. Other curves are based on the average value of ϵ_{eff}.
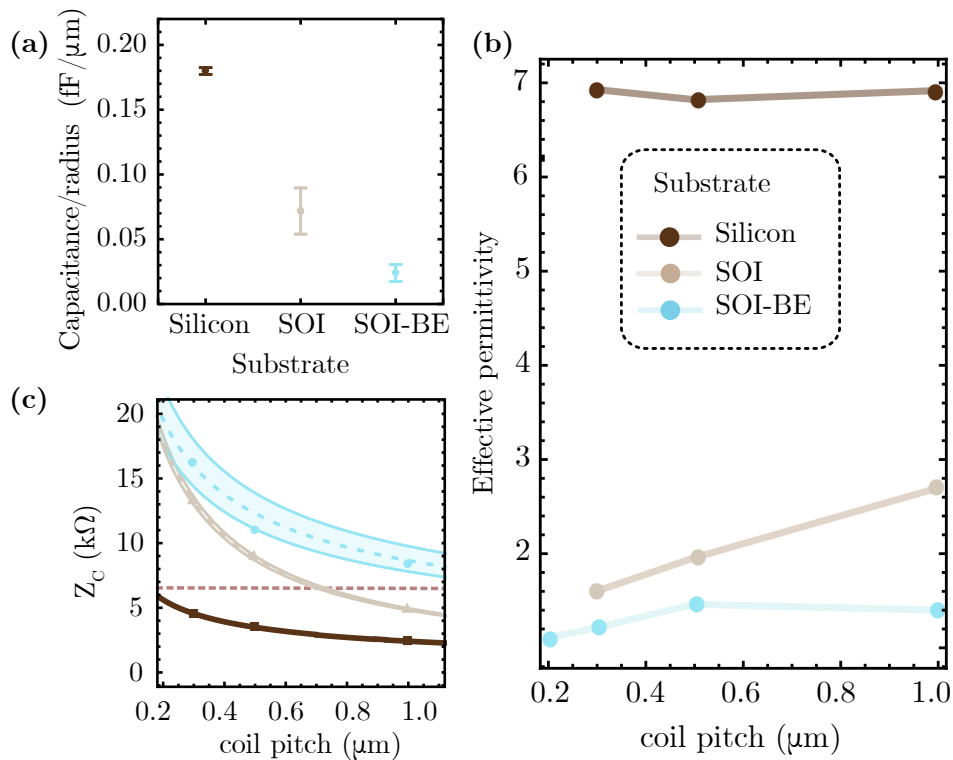
Figure 3.5: **Comparing trends across substrates.** (a) Capacitance per unit radius for different substrates, these numbers were extracted from the line fits shown in the bottom panels of Fig. 3.4. (b) Average effective permittivity values extracted from the fits to the frequency data shown in the top panels of Fig. 3.3. (c) Characteristic impedance vs. pitch for the three substrates where the coil frequency is fixed to 10.7 GHz. The points represent coils with this frequency measured for different substrates and pitches. The fit bands represent the standard deviation of the effective permittivity with the exception of the SOI curve (beige) where due to the high variation in the effective permittivity an interpolation function was taken instead of a constant value.

CHAPTER 4

GEOMETRIC RF SQUID QUBITS

4.1 CHAPTER INTRO

The following chapter reports on the measurement of several RF-SQUID qubits. The chapter will go over initial design considerations and measurements of spectra and coherence. This work was done with the help of Farid Hassani, who assisted in the modelling and fabrication of the devices, and of Grisha Szepp, who coded the fitting algorithm. This chapter is based on the paper "Geometric superinductance qubits: controlling phase delocalization across a single Josephson junction".

4.2 SAMPLE DESIGN

All qubits presented here are 2D integrated on-chip designs meaning that both the qubit and the resonator used for its readout are microscopic and fit on a single chip resulting in an extremely compact footprint of about $60\,\mu$m $\times\,120\,\mu$m for a full circuit QED system [Kjaergaard, 2020]. The full chip design consisted of 8 launchers placed along 2 sides of a 10x10 mm^2 SOI wafer. Each side having four 50 Ω launchers shorted to ground near a resonator coil.

Figure 4.1 shows a SEM of one of the launchers close to where the center conductor is shorted to ground. The sample is fabricated on SOI and therefore the center conductor and rectangle around the device are suspended. The ground is missing in the center of the chip in order to not have a superconducting loop around the qubit that can support currents and potentially affect or even obstruct the application of external magnetic flux. Figure 4.2 shows a closeup of the resonator and qubit. Both consist of planar coils with the difference that the resonator coil is open while for the qubit an air bridge is built such that the two coil ends can connect to the Josephson junction. Both air bridges and JJ can be seen in the insets.

The positions of the two coils with respect to the coupler wire's symmetry point guarantee a strong coupling to the resonator and a weak coupling to the qubit, as explained by simulations in Section 2. The coils were put in close proximity in order to guarantee a
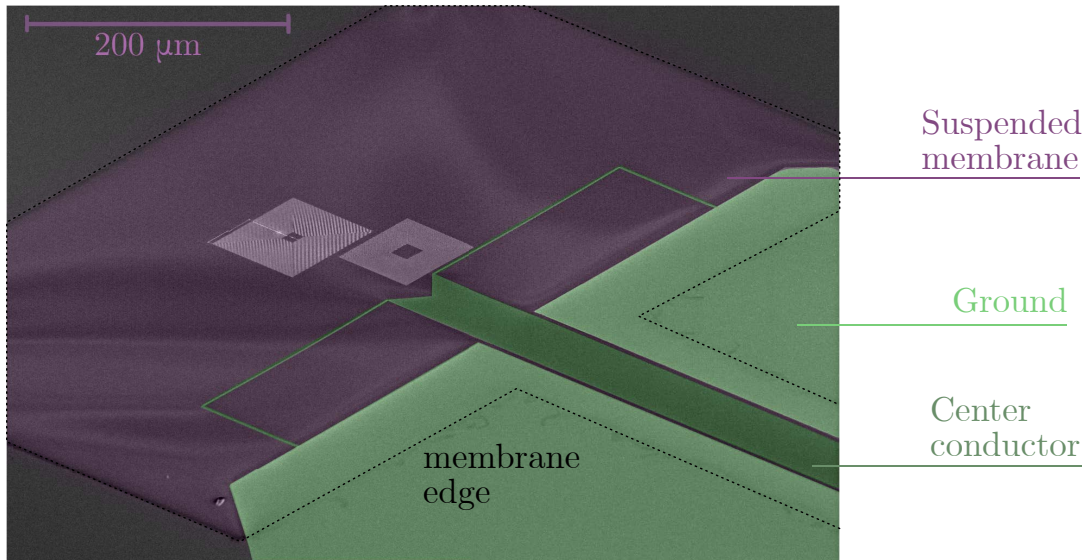
Figure 4.1: **Fluxonium SEM - overview.** A wide view of a Fluxonium qubit and resonator which shows the center conductor of the coplanar waveguide (dark green), the ground (light green) and suspended membrane (purple) on which the device is positioned. The edge of the suspended membrane (dotted, black) shows the coplanar waveguide is also free-standing.

strong coupling between the two.

Overall six RF-SQUID qubits were measured which can be devided in two different designs according to the size of the qubit coils. The different coil parameters are reported in Table 4.1

	Coil turns	pitch (μm)	L (nH)	C (fF)	f_0 (GHz)
Design 1	74	0.4	280	2.7	3.5
Design 2	125	0.3	720	3.2	3.6

Table 4.1: **Design parameters for RF-SQUIDs qubits.** The two different designs are distinguished by the different geometry of the qubit coil. The reported parameters are from the qubit coil geometry or Sonnet simulation of the coil properties. Within a single design the differences were given by changes in junction size and oxidation.
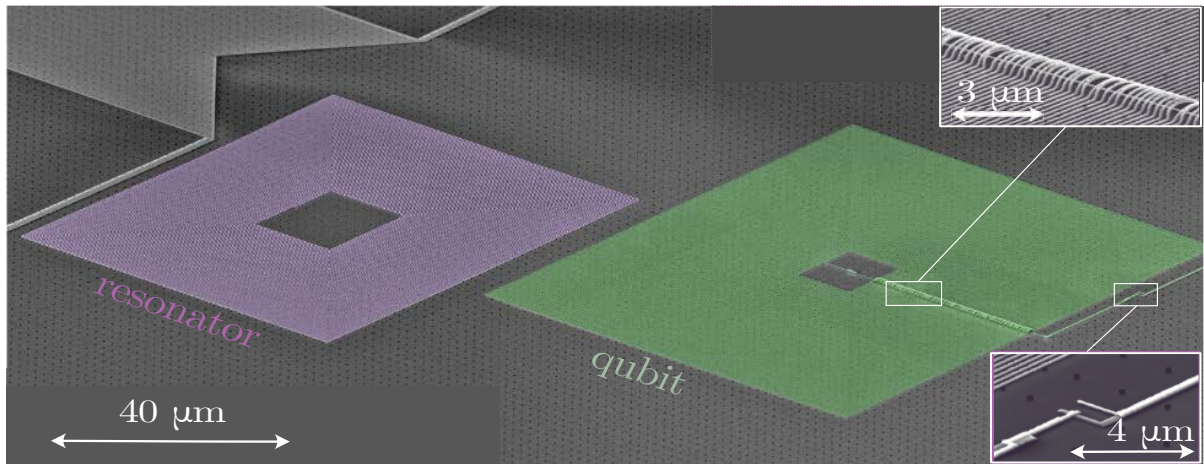
Figure 4.2: **Fluxonium SEM - close-up.** A close-up SEM of the device with design 2. In purple is the resonator coil, placed asymmetrically with respect to the coupler while the qubit in green is centered. Insets show an enlarged view of the bridges and the Josephson junction.

4.3 SPECTRA AND PROPERTIES

The first step in characterizing any qubit is to measure the transition frequencies. In the case of RF-SQUID qubits the spectrum is to be measured as a function of external flux threaded through the fluxonium loop. Flux Φ_{ext} was applied by a millimeter-sized coil attached to the outer side of the copper box shown in Section 2.5.1 as seen in Ref. [Bianchetti, 2010].

Figure 4.3 shows the spectroscopy data of the measured qubits belonging to the two types of designs described in Table 4.1. Superimposed to the spectroscopy data are the predicted energy levels obtained with the parameters displayed in Table 4.3. The parameters were found by fitting the data to the eigenvalues of the full Hamiltonian from Eqs. 1.13 and 1.24.

Fitting fluxonium spectra and their coupling constants can be a challenge due to the multitude of parameters and their non-trivial effect on the energy levels. In an effort to make parameter fitting computationally tractable, the energy levels of the full Hamiltonian are computed using the in-place eigenvalue solvers for Hermitian matrices available in the Julia standard library. These solvers are highly performant, yielding eigenvalues for a
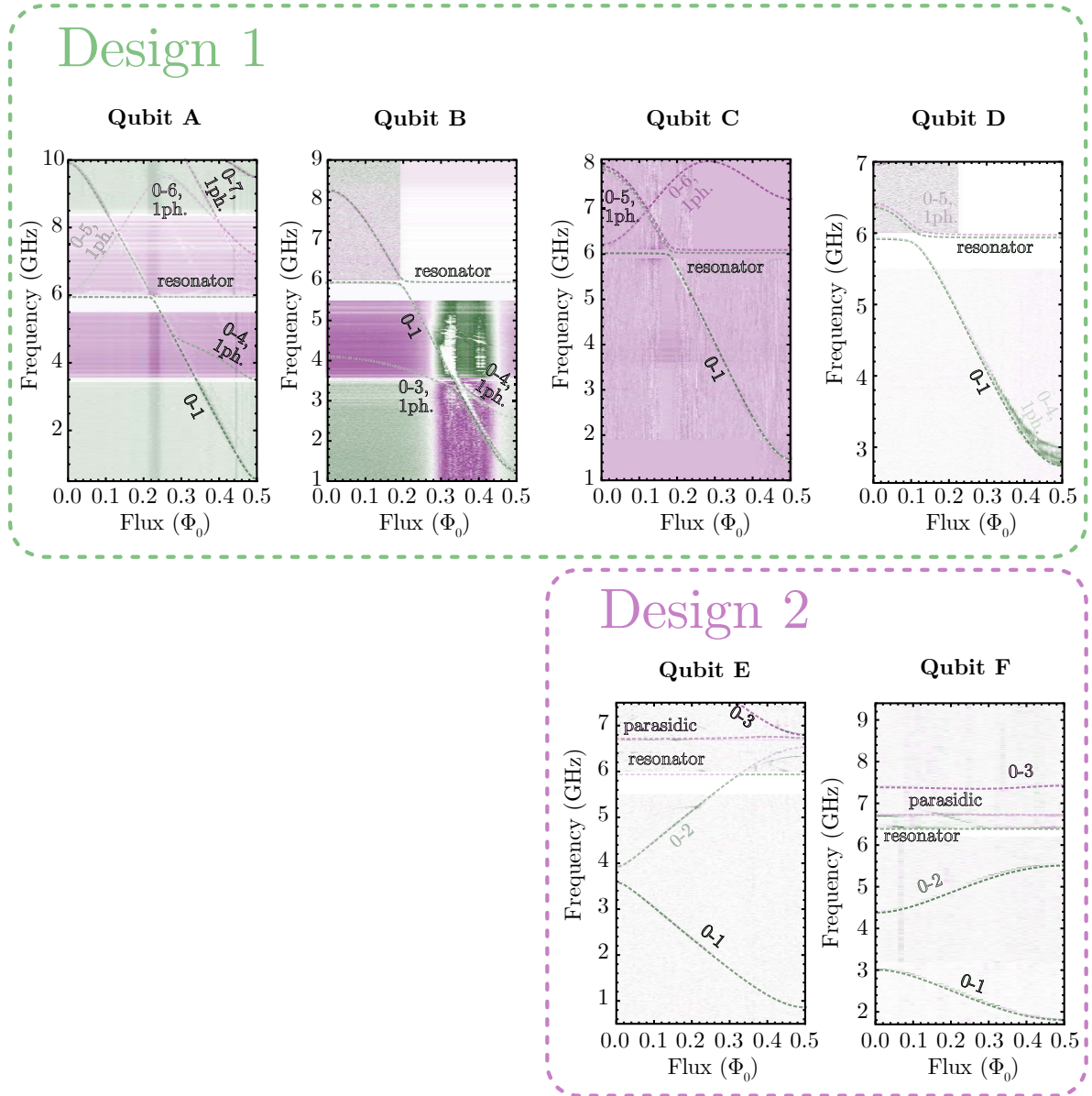
Figure 4.3: **All qubit spectra.** Spectroscopy data of the measured qubits with fit lines corresponding to the eigenvalues of the Hamiltonian of Eq. 1.13 for the values of E_J, E_L, E_C, g_C and g_L reported in Table 4.3.

Qubit	$\frac{E_L}{h}$ (GHz)	$\frac{E_C}{h}$ (GHz)	$\frac{E_J}{h}$ (GHz)	$\frac{g_C \hat{n}}{2\pi}$ (MHz)	$\frac{g_L \hat{\phi}}{2\pi}$ (MHz)
A	0.618	2.75	8.55	15	0.1
B	0.620	3.15	5.92	63	140
C	0.619	3.25	5.41	69	100
D	0.620	3.83	3.05	41	210
E	0.205	2.97	4.89	6	2
F	0.215	3.40	1.99	90	7

Table 4.2: **Measured and fitted qubit parameters.** A collection of all fitted parameters for the qubits displayed in Fig. 4.3

100×100 Hermitian matrix (5 photon states and 20 plasmon states) in less than 2 ms on a typical laptop (Intel Core i7-6700HQ CPU @ 2.60GHz x 8). The eigenvalue solver is then run repeatedly by a gradient-free local optimization routine [Mogensen, 2018] until it converges on a set of parameters which best matches the data. Since the optimization routine is local, whether a trajectory converges on the correct solution depends on the choice of initial parameters. The most efficient strategy is to first optimize the qubit parameters (E_L, E_C, E_J) to Eq. 1.13 and then adding the coupling constants (g_L and g_C) and fitting to the full model while fixing values for qubit parameters. The code implementing the fitting of RF-SQUID spectra and coupling constants has been made available [Szep, 2021].

For each design in Fig. 4.3 the value of E_J/E_C is decreased from left to right. The spectra with larger E_J/E_C demonstrate higher flux dispersion because of the higher flux localization explained in the Section 1.3.2. Qubits with design 2 show lower transition frequency and flux dispersion due to being in the higher impedance regime. Lines labelled as $i - j$ represent the transition frequency between the ith and j^{th} qubit state when no photons are populating the cavity. When a line is labelled $i - j$, k *photons* it represents the $i - j$ transition with k photons in the cavity. The fits show good agreement with the data even for higher photon numbers. The qubits with design 2 show an additional parasitic mode which is discussed in depth later in this chapter.

In Fig. 4.4(a) the measured qubits are placed on the parameter landscape in Fig. 1.9. Purple circles are geometrically implemented RF-SQUIDs, A-F are reported in this chapter while G and H were coupled to 3D cavities and are discussed in [Peruzzo, 2021]. The green markers represent RF-SQUID qubits where the inductor was made out of nanowire
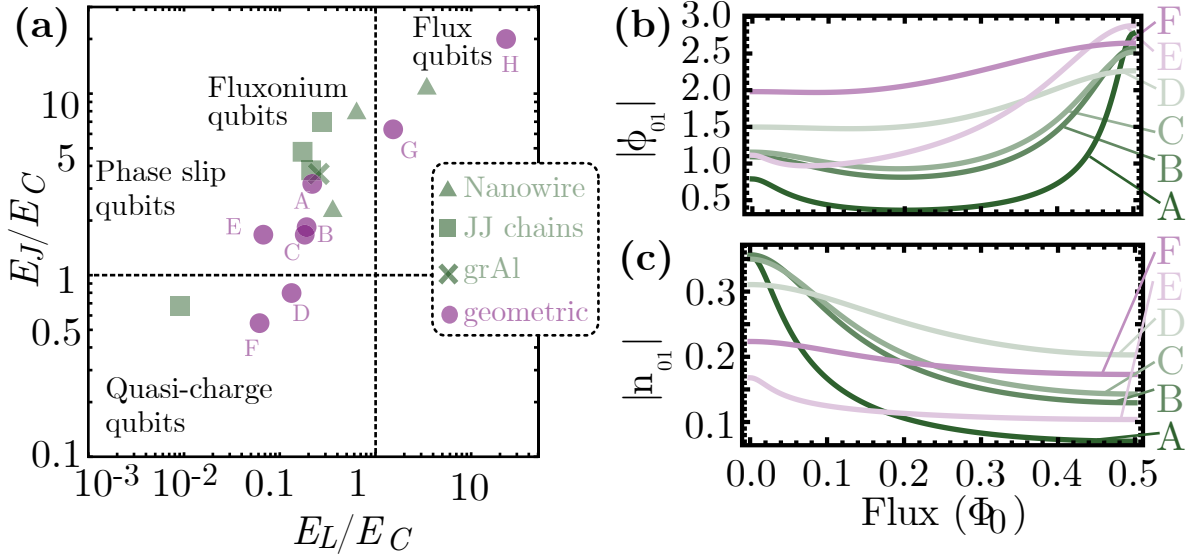
Figure 4.4: **Qubit energy ratios and matrix elements.** (1) Plot similar to that of Fig. 1.9 where qubits are positioned according to the ratio of the two potential energy terms (E_L and E_J) and the kinetic term (E_C). The qubits represent measured 2D and 3D geometric qubits (purple) alongside designs that rely on kinetic inductance (green). (b-c) Plots of flux (b) and charge (c) matrix elements of the $0-1$ transition of the measured qubits.

inductors [Hazard, 2019; Peltonen, 2018], Josephson junction chains [Manucharyan, 2009; Pop, 2014; Pechenezhskiy, 2020] and granular aluminum inductors [Grünhaupt, 2019]. The plot demonstrates the ability of the geometric method to reach a multitude of different qubit types in the RF-SQUID family.

Figure 4.4(b-c) presents the flux and charge matrix elements of the qubits' $0-1$ transition, ϕ_{01} and n_{01} respectively. These quantities represent the strength of the effects that flux/charge fluctuations have on the fist transition of the qubit, as well as quantifying the how well the qubit can be coupled to via inductance (flux) or capacitance (charge).

As a first consideration one can note the difference in magnitude and dispersion. While the charge matrix elements remain low for all flux values, the flux matrix elements show more variation and absolute magnitude. Charge matrix elements are lowest at the half flux quantum where flux matrix elements reach their maximum. This signifies that at the frustration point the qubit is mostly driven magnetically. In both cases the qubits with lower E_J/E_C display lower dispersion in both matrix elements mirroring the lower dispersion also observed in the transition frequency.
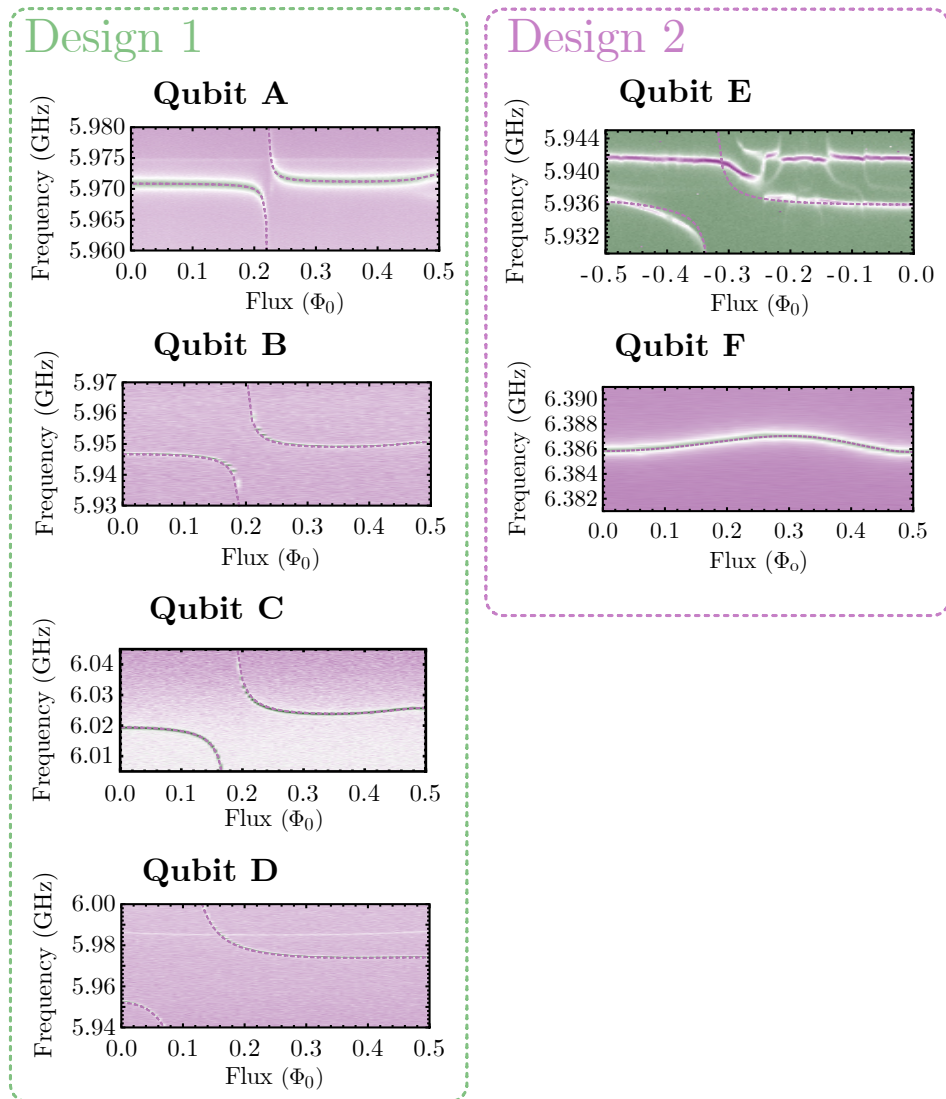
Figure 4.5: **Resonator dispersion.** Plots of the low power resonance frequency of the resonator as a function of external flux. Fit lines correspond to the eigenvalues of the full Hamiltonian with parameters displayed in Table 4.3.

In Fig. 4.5 the flux dispersion of the resonator and the fitted spectrum are shown for all devices. For the devices in design 1, due to the larger flux dispersion of the qubits, the resonators all show an anticrossing. In the case of qubit E the measurement showed some cross coupling to other resonators on the chip with similar resonance frequency. This resulted with two resonance lines both coupled to the qubit to different degrees. The effect was a smaller qubit-resonator coupling as the resonance mode was split between two saparate launchers. The fit did not take the double mode into consideration and is therefore less accurate.

4.4 TIME DOMAIN MEASUREMENTS

Relaxation and coherence measurements were conducted on all qubits with the exception of qubit A where the signal to noise was too low to obtain good quality coherence measurements.

Figure 4.6 shows the collection of time domain measurements done for the qubits. For each qubit the top plot is a relaxation measaurement taken at half flux quantum where the qubit state is being measured as a function of time after a π pulse. The π pulses were all in the range of 20-25 ns and were limited by instrument rise times. Overcoming these limitations could allow for the pulse length to go down to a few ns. Measurements are done by pulsing both the drive and measurement source, the measurement pulse is then averaged over and the process is repeated for different wait times. The averaged amplitude data S_{11} is then fitted to an exponential function in the case of T_1 and to a cosine function with an exponential envelope in the case of T_2. The data is then normalized by removing the fitted offset and dividing by the fitted amplitude returning values between 0 and 1, taken to be the average qubit state. This method assumes that the qubit is reset to $|0\rangle$ after each measurement and that it reaches $|1\rangle$ after a π pulse. Due to the low frequency of some of the qubit transitions at the flux frustration point thermal fluctuations might not allow for a perfect reset. Methods to reset very low frequency qubits have been explored in Ref. [Zhang, 2021] but were not attempted here.

The exponential fit to the relaxation data can be seen plotted on a logaritmic scale in

Fig. 4.3. With the exception of qubit E these are all under 4 μs. Below the relaxation measurement a coherence measurement as a function of external flux around the flux frustration point is presented. The error bars represents the coherence times and errors extracted from separate measurements often performed over 10-15 hours. The black solid line represents the fit to a flux noise induced decoherence model and with $2\mathrm{T}_1$ as the limit

$$\Gamma_\Phi^{\text{echo}} = 1/T_2^{\text{echo}} = \frac{\partial \omega}{\partial \Phi_{\text{ext}}} \sqrt{A_\Phi} \gamma + \frac{1}{2T_1}, \tag{4.1}$$

where $\Gamma_\Phi^{\text{echo}}$ is the decoherence rate, $\mathrm{T}_2^{\text{echo}}$ is the decoherence time, ω is the qubit's angular frequency, Φ_{ext} is external flux, A_Φ is the noise amplitude of the spectral density $S_\Phi(\omega) = A_\Phi/\omega$ and γ is a constant which depends on the specific filtering function given by the chosen spin echo sequence.

In the cases of qubits A, B, C and D the coherence was measured with a standard Ramsey measurement, while for qubits E and F different spin echo sequences were utilized.

Figure 4.6 demonstrates that the limiting factor for the coherence is flux noise. However

Qubit	T_1 [μs]	A_ϕ [$\mu\Phi_0$]
A	1.47	-
B	2.38	317
C	3.29	338
D	1.81	787
E	9.62	673
F	2.25	646

Table 4.3: **Coherence parameters.** Table containing the T_1 values at the sweet spot and the flux noise amplitude extracted from the plots in Fig. 4.6.

at the sweetspot the transition frequency becomes insensitive to first order flux noise and second order noise does not appear to be a limiting factor. Given that the qubits do not reach coherence of $2T_1$, the theoretical limit, there is an additional source of decoherence at play. The most likely candidate is the photon shot noise, i.e. noise due the shift in qubit frequency caused by variations in intra-cavity photon number. This noise is directly related to the high qubit-resonator coupling as it is exacerbated with a high ratio of κ/χ_{01} [Rigetti, 2012], where κ is the total cavity linewidth and χ_{01} is the cavity pull on the qubit. In fact the reason for photon shot noise is the displacement in qubit frequency due to photons occupying the cavity (AC stark shift) and therefore fluctuations in cavity
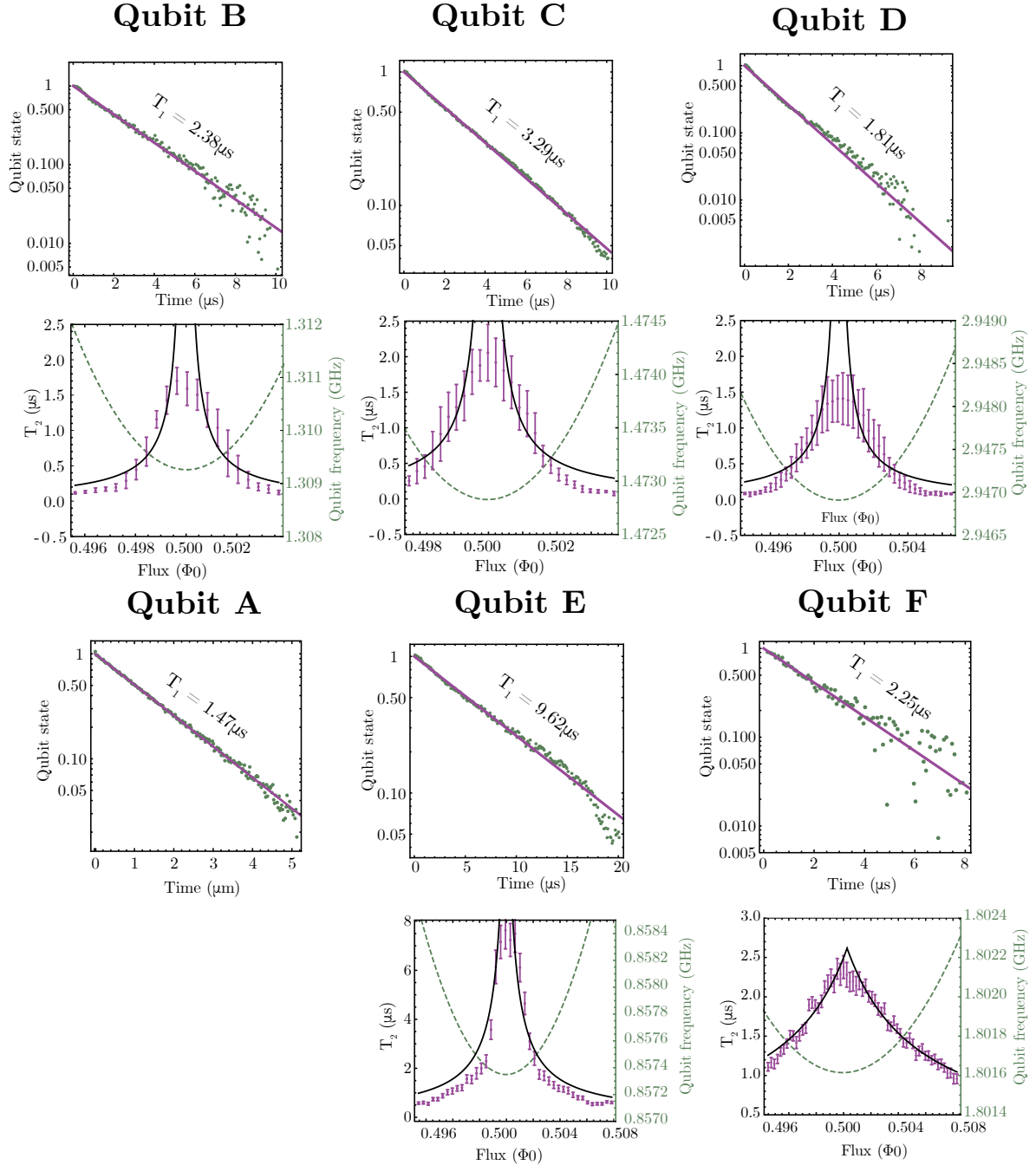
Figure 4.6: **Qubit coherence times.** A collection of the time domain data collected for all qubits showing measured energy relaxation time T_1 and decoherence time T_2 as a function of external flux in units of Φ_0.
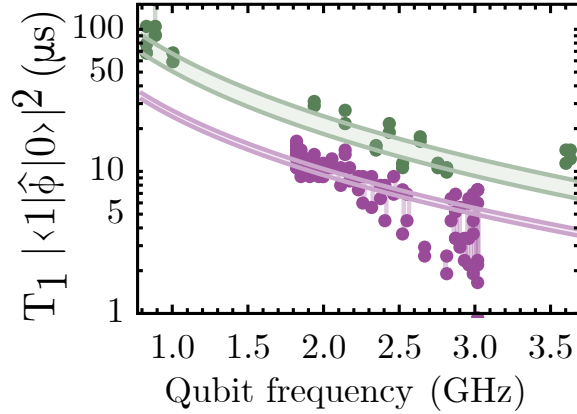
Figure 4.7: T_1 **vs frequency.** Measured energy relaxation time T_1 of qubits E and F multiplied by the squared flux matrix element $|\langle 0|\hat{\phi}|1\rangle|^2$ as a function of qubit frequency. Fit bands are to a dielectric loss model (Eq. 4.2) where the fit parameters are quality factors of the circuit capacitances. These were found to be $(48 \pm 9) \times 10^3$ for qubit E and $(18.4 \pm 0.7) \times 10^3$ for qubit F.

photon number shake the qubit frequency creating dephasing. The degree of the shaking will depend of the coupling strength and spacifically on κ/χ_{01}.

In the case of qubits E and F an additional limitation was added to the fit to account for shot noise, this was fitted to be 30.0 μs and 6.2 μs for qubits E and F respectively. These losses correspond to an average photon occupancy of 0.03 and 0.006, which in turn indicates a thermal bath of 80 mK and 60 mK. These numbers are on-par with similar implementations [Yan, 2016] and could be further improved with better shielding. The relaxation data displayed in Fig. 4.6 doesn't have a clear limiting factor, for such an analysis one needs to collect T_1 data as a function of frequency as shown in Fig. 4.7. The values of T_1 multiplied by the absolute square of the phase matrix element versus the qubit transition frequency for qubits E and F. The T_1 data was extracted placing the qubit in a mixed state via a saturation pulse and then measuring the decay, the measurement was repeated along side a spectroscopy measurement to determine the qubit frequency for different external flux values. The values of T_1 are consistent with measurements done with a π pulse excitation at the frustration point shown in Fig. 4.6. The matrix elements were calculated numerically using the *scqubits* python library [Koch, 2021].

The behavior of the data agrees with a pure capacitive loss model, indicating that other loss mechanisms such as losses through the inductor or through the resonator (i.e. the

Purcell effect [Houck, 2008]) were not limiting. Even with the high coupling the Purcell limit to T_1 for these qubits is in the hundreds of μs due to the large detuning. We plot the data along side a temperature dependent capacitive loss model derived from Fermi's golden rule [Schoelkopf, 2003]

$$\Gamma_1 = 1/T_1 = \frac{1}{(2e)^2} |\langle 0|\hat{\phi}|1\rangle|^2 \hbar \omega_q^2 \frac{C}{Q_{\text{diel}}} \coth\left(\frac{\hbar\omega}{2k_B T}\right), \qquad (4.2)$$

where Γ_1 is the relaxation rate, T_1 is the relaxation time, $\langle 0|\hat{\phi}|1\rangle$ is the phase matrix element, ω_q is the qubit's angular frequency, C and Q_{diel} are the total capacitance of the qubit and its quality factor and T is the qubit temperature.

The bands shown in Fig. 4.7 are fits to Eq. 4.2 with a fitted $Q_{\text{diel}} = (57 \pm 8) \times 10^3$ for E and $Q_{\text{diel}} = (25 \pm 1) \times 10^3$ for F. These values are similar to the internal quality factors found for geometric superinductor resonators at single photon power on the same substrate (i.e. without handle wafer removal) [Peruzzo, 2020] and on par with other fluxonium implementations [Hazard, 2019]. The temperature is taken as 60 mK and 80 mK respectively, as per the previous analysis. The values of T_1 of qubit F are found to be consistently higher than the values for qubit E. This is in part due to a lower transition frequency which stems from the larger tunneling barrier and a higher quality factor due to better cleaning in fabrication.

4.5 PARASITIC MODE

The planar coil used as a superinductor is a distributed element circuit. At low frequencies it can be described by a simple lumped element model, i.e. a parallel LC circuit where the fundamental mode forms the first transition frequency of the qubit. The second mode of the coil inductor acts as a resonator mode that couples strongly to this qubit mode. We use finite element simulations like the one shown in Fig. 2.4 for the coil used in qubits E and F to predict the frequency of this mode as shown in Fig. 4.8(a). At a frequency of about 6.5 GHz the admittance shows an additional pole compared to the simple LC model. We model this by adding in parallel to the original LC circuit an extra inductance and capacitance in series as shown in Fig. 4.8(b).
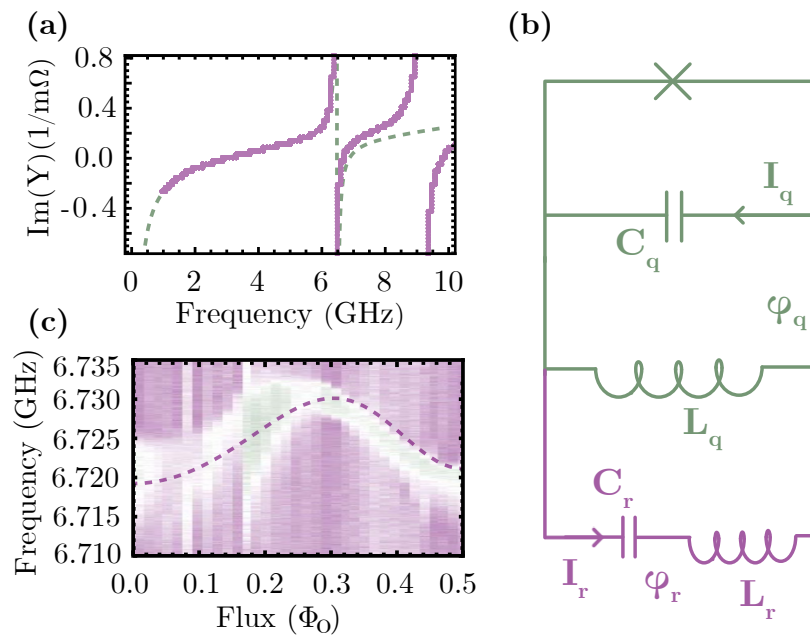
Figure 4.8: **Qubit parasitic mode.** (a) Simulated admittance of the coil used in qubits E and F. Purple dots represent the simulation, green dashed line is a fit to the circuit shown in panel (b). Fitted parameters are C_q = 4.8 fF, L_q = 530 nH, C_p = 0.47 fF, L_p = 1.3 μH. The simulated data shows an additional pole appearing at higher frequency that was not identified in the qubit spectrum. (b) A phenomenological circuit model for the high frequency response of the coil inductor that shows very good agreement with the simulated admittance up to around 8 GHz. The green part of the circuit represents the qubit while the purple part models the parasitic mode. (c) Two tone spectroscopy data of the parasitic mode of the qubit. The dashed line is obtained by solving the full Hamiltonian containing the qubit, the resonator mode and the parasitic mode. Here the coupling to the parasitic mode was taken to be 0.84 GHz as correctly predicted by Eq. 4.9.

The Lagrangian for this circuit is

$$\mathcal{L} = C_q(\dot{\phi}_q)^2 + C_p(\dot{\phi}_q - \dot{\phi}_p)^2 + \frac{1}{2}E_{L,q}\phi_q^2 + \frac{1}{2}E_{L,p}\phi_p^2 - E_J\cos\phi_q, \tag{4.3}$$

where C_q (C_p) and ϕ_q (ϕ_p) represent the capacitance and phase variable of the qubit (parasitic mode) and $E_{L,q}$ and $E_{L,p}$ represent the inductive energies of the qubit and parasitic mode, corresponding to L_q and L_p as shown in the circuit in Fig. 4.8(b).

Next the relation between the node voltages and currents of the circuit must be identified. This enables the replacement of the node voltages $\dot{\phi}_q$ and $\dot{\phi}_p$ with their respective canonical conjugates $Q_q = \frac{\partial I_q}{\partial t}$ and $Q_p = \frac{\partial I_r}{\partial t}$. Using Kirchhoff's laws one can write the following equations in the Fourier domain

$$\begin{cases} V_q - V_p = \frac{I_p}{C_p S} \\ \\ V_q = \frac{I_q - I_p}{C_p S} \end{cases}, \tag{4.4}$$

where S is the complex frequency, which corresponds to a differentiation operator in the time domain $\frac{d}{dt}$, while $\frac{1}{S}$ is an integration operator $\int dt$.

Using these relations and the fact that $V_q = \dot{\phi}_q$ and $V_p = \dot{\phi}_p$ we can rewrite Eq. 4.4 as

$$\begin{cases} \dot{\phi}_p = \frac{Q_q - Q_p}{C_q} - \frac{Q_p}{C_p} \\ \\ \dot{\phi}_q = \frac{Q_q - Q_p}{C_q}. \end{cases} \tag{4.5}$$

Replacing Eq. 4.5 into Eq. 4.3 gives rise to the final form of the total Hamiltonian

$$H = H_{\text{parasitic}} + H_{\text{qubit}} + H_{\text{coupling}} =$$

$$\frac{\hat{Q}_p^2}{(C_p^{-1} + C_q^{-1})^{-1}} + \frac{1}{2}E_{L,p}\hat{\phi}_p^2 + \frac{1}{2}E_{L,q}\hat{\phi}_q^2 - E_J\cos\hat{\phi}_q + \frac{\hat{Q}_q^2}{C_q} + \frac{2\hat{Q}_q\hat{Q}_p}{C_q} \tag{4.6}$$

where we quantize $\hat{\phi}$ and $\hat{Q}$. From Eq. 4.6 it is possible to identify the frequency of the parasitic mode as

$$\omega_p = \sqrt{\frac{1}{L_p(C_p^{-1} + C_q^{-1})^{-1}}}. \tag{4.7}$$

Rewriting the coupling term of Eq. 4.6 in the second quantization formalism results in

$$H_{\text{coupling}} = \frac{2\hat{Q}_q\hat{Q}_p}{C_q} = \frac{2}{C_q}\sqrt{\frac{\hbar}{2Z_p}}(\hat{a} + \hat{a}^\dagger)\hat{Q}_q, \tag{4.8}$$

which identifies the coupling strength as

$$g_p = \frac{4e}{C_q} \sqrt{\frac{\hbar \omega_p (C_p^{-1} + C_q^{-1})^{-1}}{2}}. \tag{4.9}$$

By fitting the coil admittance in Fig. 4.8(a) we find the parasitic inductance to be $L_p =$ 1.28 μH and the parasitic capacitance to be $C_p = 0.47$ fF. By inserting these values into Eq. 4.7 alongside the fitted qubit parameters the frequency of the parasitic mode is expected at $\nu_p = 6.74$ GHz, very close to the measured value seen in Fig. 4.8(c) and the coupling is expected to be $g_p/(2\pi) = 0.84$ GHz.

The fit line in Fig. 4.8(c) is obtained by diagonalizing the Hamiltonian of the whole system consisting of the qubit, the resonator and the parasitic mode where the parasitic mode is added as an additional resonator coupled to the qubit. For the fit the frequency of the parasitic mode was taken to be 6.73 GHz while the coupling was taken from Eq. 4.9 with values based on the simulated admittance. We find excellent agreement between the measured data and the predicted curve Fig. 4.8(c).

CHAPTER 5

TOWARDS THE OBSERVATION OF COULOMB BLOCKADE OF COOPER PAIR TUNNELING

5.1 CHAPTER INTRO

This chapter documents a series of experiments on Josephson junctions done with the goal to measure Coulomb blockade of Cooper pair tunneling and eventually dual Shapiro steps across a single junction. As this work is still in process, the work presented is mostly tests and lead-up experiments. This chapter serves as a guide and starting point for future developments towards the aforementioned goals.

The work in this chapter was done with the theoretical support of Lisa Arndt and Fabian Hassler from RWTH Aachen University who helped with the understanding of the system and interpretation of the results and with the help of Andrea Trioni who has helped with the design and fabrication and will be further progressing this work. When describing the series resistance or inductance of a component (off-chip resistors or coils) the values specified are per component. When adding resistors or inductors to the circuit they are added as pairs (one on each side of the junction) and therefore the total resistance/inductance is double.

5.2 JOSEPHSON JUNCTION MEASUREMENTS

5.2.1 IV CURVES

As a first step it is important to establish the capability of the experimental setup in measuring Josephson junction IV curves and whether the system is able to thermalize sufficiently.

The samples were mounted on a customized PCB from Beta Layout screwed into a copper box which in turn was thermally anchored to the 10 mK stage of the dilution refrigerator. These measurements were conducted with a 4-probe approach which allows to see the resistance of the junction alone. Two different IV curves are presented in Fig. 5.1: (a) is an IV curve where thermalization was not optimal while on (b) a copper clip was
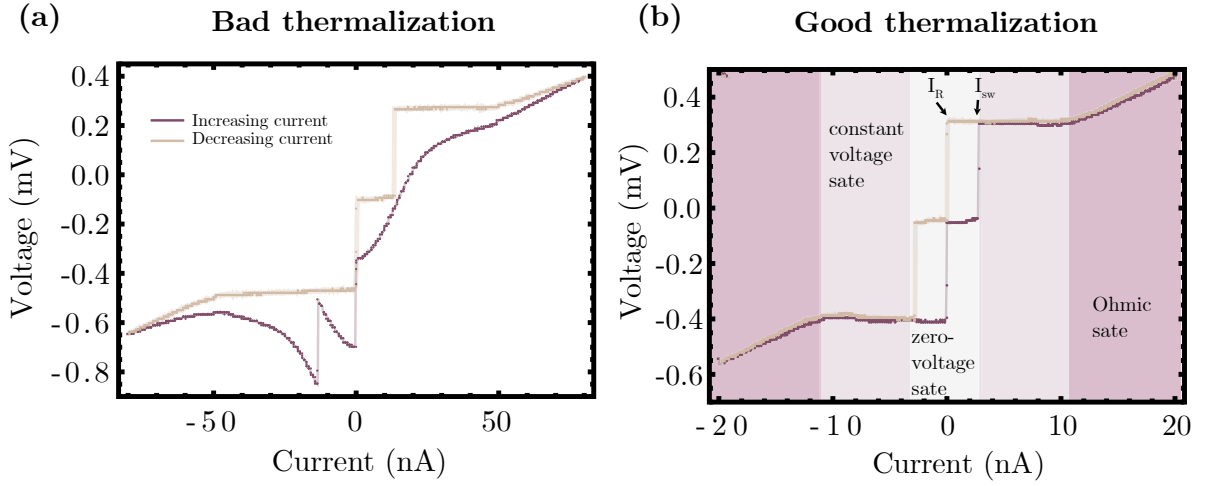
Figure 5.1: **Josephson junctions and thermalization.** Difference between a well thermalized (a) and badly thermalized (b) IV curve of a Josephson junction. For both plots the purple line indicates increasing current, meaning that the sweep went from negative to positive, while the cream colored lines indicates the opposite. In the good thermalization case the three areas of the IV curve are highlighted. Arrows identify the switching current I_{sw} and the return current I_R

used to clamp the chip to improve thermalization of the sample. The hot sample (a) showed a non-reliable IV curve which gave different results when the current sweep was started at zero or at higher absolute values of the current or for different measurements. This indicates that the reason is a temperature increase due to Joule heating which is proportional to the square of the current. When the sample was better thermalized these effects disappeared further confirming the origin of this effect.

In addition to thermalization properties the measured IV curves are able to tell us about properties of our Josephson junction and setup. Firstly three distinct areas of the IV curve can be identified: the zero voltage state, the constant voltage state and the Ohmic state. These distinctions can be seen on Fig. 5.1(b). The measurement shows hysteresis in the IV curve, meaning that the shape of the IV curve depends on weather the current is tuned from low to high values or vice-versa. Strong hysteresis is the characteristic of a junction with high quality factor, i.e. in Eq. 1.6 the term associated with the second order derivative is dominant meaning a high resistance and capacitance parallel to the junction. Considering the fact that no parallel resistance was added to the junction high quality factor is to be expected. The current at which the junction switches from the zero-voltage
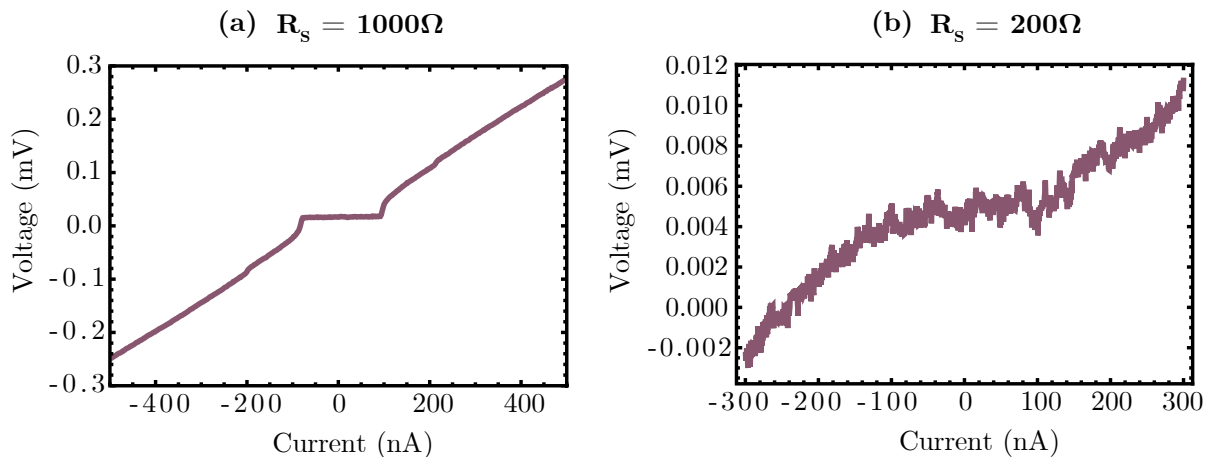
Figure 5.2: **Josephson junctions and parallel resistance.** (a) Measured IV curve of Josephson junction shunted on the PCB by R_S = 1 kΩ. (b) Measured IV curve of Josephson junction shunted on the PCB by R_S = 200 Ω.

state to the constant voltage state is the switching current. When the junction's quality factor is low this is equal to the critical current, however in the case of a high quality factor thermal and quantum fluctuations can cause the junction to jump to the voltage state early via tunnelling. As this is a stochastic process the switching current I_{sw} will occur at random points following a distribution. On the other hand the current at which the voltage goes to zero when the current is decreased from above I_C is the return current, I_R. Finally the Ohmic state is where the junction behaves as a regular resistance, from this branch the junction resistance can be extracted which can be used to determine the Josephson energy E_J and critical current I_C with the following relation:

$$E_J = \frac{\Phi_0}{2\pi} I_C = \frac{R_Q \Delta}{2 R_N e} \tag{5.1}$$

where R_Q is the resistance quantum, Δ is the voltage gap of the superconductor at zero temperature and R_N is the normal resistance of the junction. This formula assumes that the resistance is given by the junction alone and no parallel resistance is added. The junction's nominal size is 300×200 nm² with a critical current extracted from the resistance of the voltage branch to be $I_C = 13$ *nA*.

Further investigation into quality factors was done by adding series resistors to Josephson junctions to try control the hysteresis parameters. In Fig. 5.2 it is shown how different series resistors added affected the IV curve. In Fig. 5.2(a) the resistor was shorted by 1 kΩ while in (b) it was shorted by 200 Ω. Both show no hysteresis and can therefore be

classified as overdamped. In addition, Fig. 5.2(b) shows a very noisy plateau due to the low voltages deriving from the small shorting resistance. Both junctions were fabricated on the same Silicon chip with a nominal size of 300×1000 nm^2.

5.2.2 SWITCHING CURRENT DISTRIBUTIONS AND TEMPERATURE SWEEPS

The previous samples were evaporated on a high resistivity Silicon chip, however to increase impedance the area around the Josephson junction would eventually need to be suspended on a SOI membrane similarly to the qubits in Section 4. Consequently another sample was fabricated on SOI where three scenarios were tested for their thermalization:

- Silicon on silicon dioxide, where a sample is fabricated on the SOI chip but the silicon dioxide is not removed from under the junction. This was meant to be a control device.

- Silicon on insulator where the membrane was released. The sample was included to investigate weather the membrane could dissipate temperature.

- Silicon on insulator with a released membrane and a 100 kΩ resistor was placed in series with the junction off chip. The resistor is a necessary component for a Coulomb blockade measurement and hence its thermal dissipation also needs to be investigated. The resistors used were from Sumusu (S.N. RR12P100KDTR-ND) with resistance of 100 kΩ.

Samples were fabricated on an SOI substrate with nominal size of 250×200 nm^2 and the critical current was extracted to be 37 nA, 27 nA and 26 nA for the three junctions respectively. None of the samples displayed obvious signs of bad thermalization as seen in Fig. 5.1(a) and a further investigation was conducted. As stated, high Q junctions don't have a fixed switching current as this is a random process. It is properly measured as a histogram of the switching current distribution [Blackburn, 2014]. In order to extract a histogram an IV curve measurement is repeated many times and the switching current is extracted at each iteration. Figure 5.3(a-c) shows histograms of the switching current for different fridge temperatures for the three cases presented above. The histograms have an asymmetric shape and can be represented as a convolution between a Gaussian distribution and a thermal one [Wallraff, 2003]. This results in a thermal decay below the mean and a Gaussian decay above. Physically this happens because of the two types of
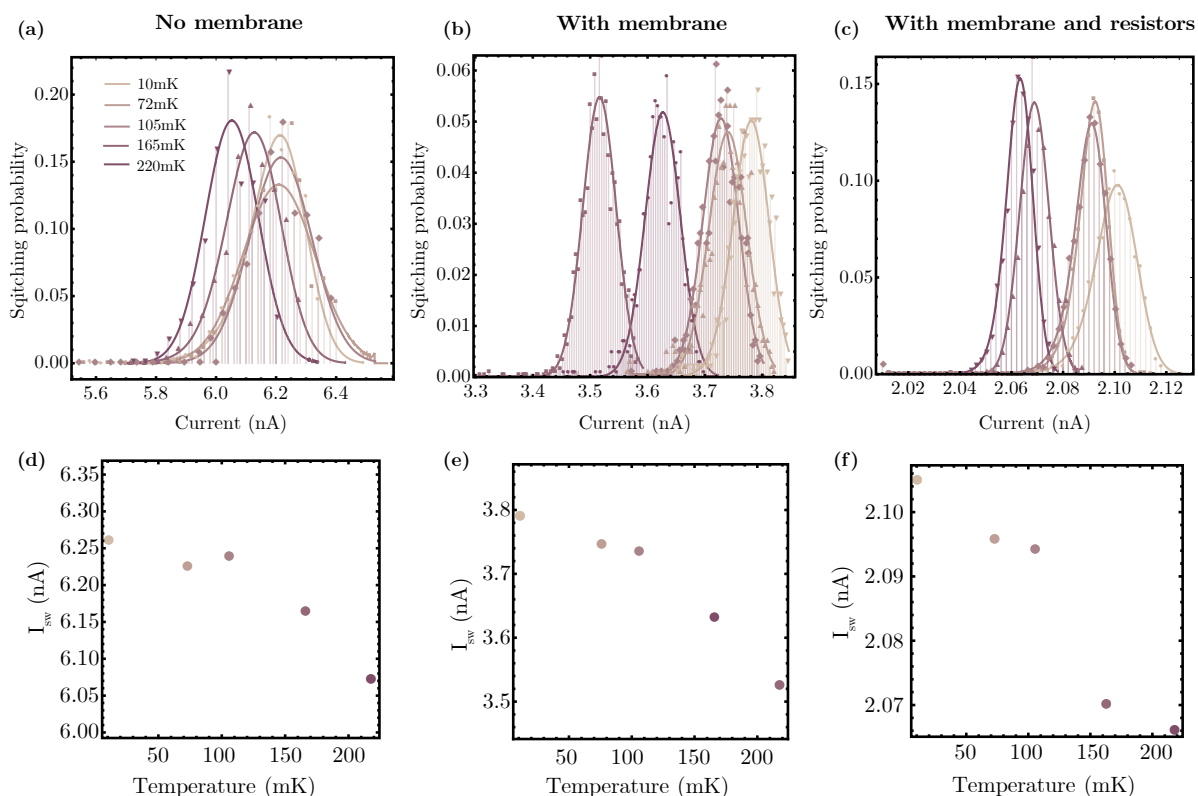
Figure 5.3: **Josephson junctions switching distributions.** (a-c) Histograms of switching current vs temperature. (d-f) Plot of the fitted mean switching point as a function of mixing chamber temperature.

fluctuations that cause the switching: thermal and quantum. While quantum fluctuations have the same chance to move the value of the switching current up or down thermal fluctuations will only move it down.

The second row of Fig. 5.3 shows the extracted mean of the histogram distribution versus temperature. The mean generally decreases monotonically with temperature for all three cases leading to the conclusion that all three sample are well thermalized. Attempting to extract effective temperatures from the relative standard deviation of the two distributions resulted in no clear conclusion due to these not following any clear trend.

The changes in mean switching currents between the samples are mostly due to changes in the external circuitry as they were found to have similar critical currents. Most interesting is the sample where the resistor was added as this has a smaller switching current but also displayed the smallest return current of all the samples. This is possibly due to the high impedance created by the resistor as it is increasing the phase fluctuations of the

environment facilitating more phase slip events which result in the escape of the phase particle from the minimum.

5.2.3 SHAPIRO STEPS

As the aim of this project is to measure dual Shapiro steps, measuring regular Shapiro steps represents an essential intermediate result. In an effort to conduct this experiment in the simplest possible way a sample was placed near an open coaxial cable pin in order to excite the junction through radiation. A more rigorous version of this measurement requires a bias tee in order to combine DC and RF signals. The junction has nominal size of 300×1000 nm^2 and a calculated critical current of 226 nA.

The method presented here resulted in the measurement of Shapiro steps, however, it required a high RF power which resulted in higher losses that manifested in a more washed out IV curve and slight heating of the fridge temperature. Figure 5.4(a) shows the results of the Shapiro steps measurement where the different lines represent different powers of the RF source ranging from -15 dBm to 0 dBm. One IV curve shows one or two steps, however, by plotting them all specific lines emerge. These are compared with the voltages where the Shapiro steps are expected (black solid lines) and the voltages at which photon assisted tunnelling occurs (red dotted lines). The latter phenomenon occurs when a quasiparticle is able to tunnel across the junctions by absorbing an integer number of photons [Tinkham, 1996]. These are distinguishable from Shapiro steps because they appear at voltages $V_{\text{PAT}} = V_{\text{g}} + n\nu/e$ where $V_{\text{g}} = 2\Delta/e$ is the gap voltage of the junction, n is an integer and ν is the frequency of the AC drive. On the other hand the Shapiro steps appear at voltages $V_{\text{Shapiro}} = n\nu/(2e)$.

The steps are more visible when the data at all powers from Fig. 5.4(a) is displayed in a histogram, seen in Fig. 5.4(b). The last three peaks in the histogram appear at double the distance and symmetrically with respect to the gap voltage and are hence attributed to photon assisted tunneling while the other peaks can be identified as Shapiro steps.
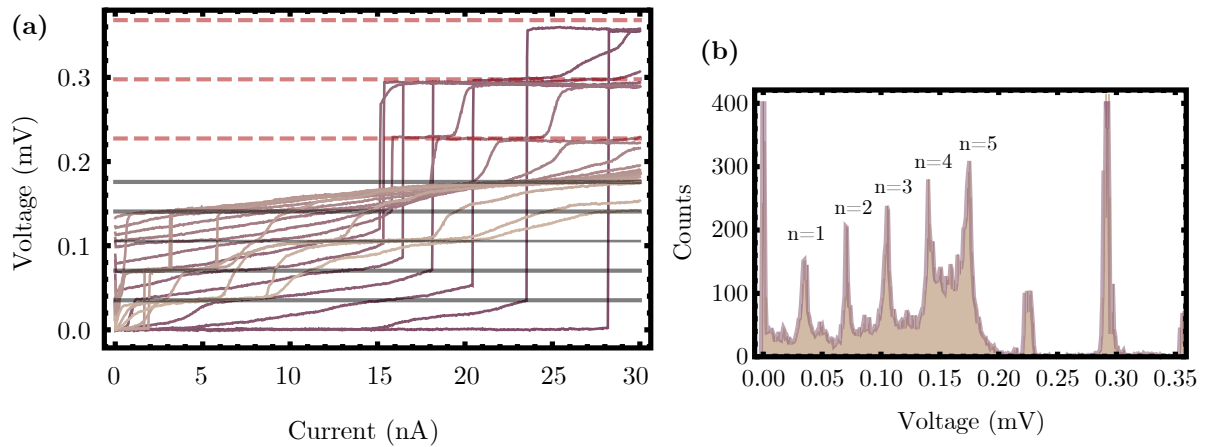
Figure 5.4: **Shapiro steps.** (a) IV curves of a junction irradiated by a microwave signal at 17 GHz. Different curves correspond to different values of RF power ranging from -15 dBm to 0 dBm. Black lines represent the expected position of Shapiro steps while the red dotted lines represent the expected position of steps due to photon assisted tunnelling. (b) Histogram taken from the data in (a). This visualization better displays the emergence of periodic steps in voltage.

5.3 MEASUREMENTS WITH COILS

As noted in the introduction both resistors and high impedance superconducting coils are needed to obtain the necessary conditions to measure Coulomb blockade and dual Shapiro steps across a single junction. The measurements in this section all include geometric superinductors and therefore for each section a table reports the coil inductance and capacitance as determined from simulations or calculations. The values of resistance used are also indicated.

5.3.1 TESTING THE DIFFERENCE WITH AND WITHOUT RESISTORS

As a first test the coils were added to the sample on each side of the junction. The sample was measured with and without 100k Ω resistors placed on the PCB. The resistors used were from Sumusu (S.N. RR12P100KDTR-ND) with resistance of 100 kΩ.

For this sample a SQUID was used in order to have control on $E_{\mathrm{J}}/E_{\mathrm{C}}$. Figure 5.5 is for

Coil turns	pitch (μm)	L (nH)	C (fF)	ν (GHz)	R (kΩ)
110	0.4	370	3.6	4.35	100

Table 5.1: **Coil parameters.** Geometric parameters, simulated coil parameters and resistor used in the samples that produced Fig. 5.5 and 5.6
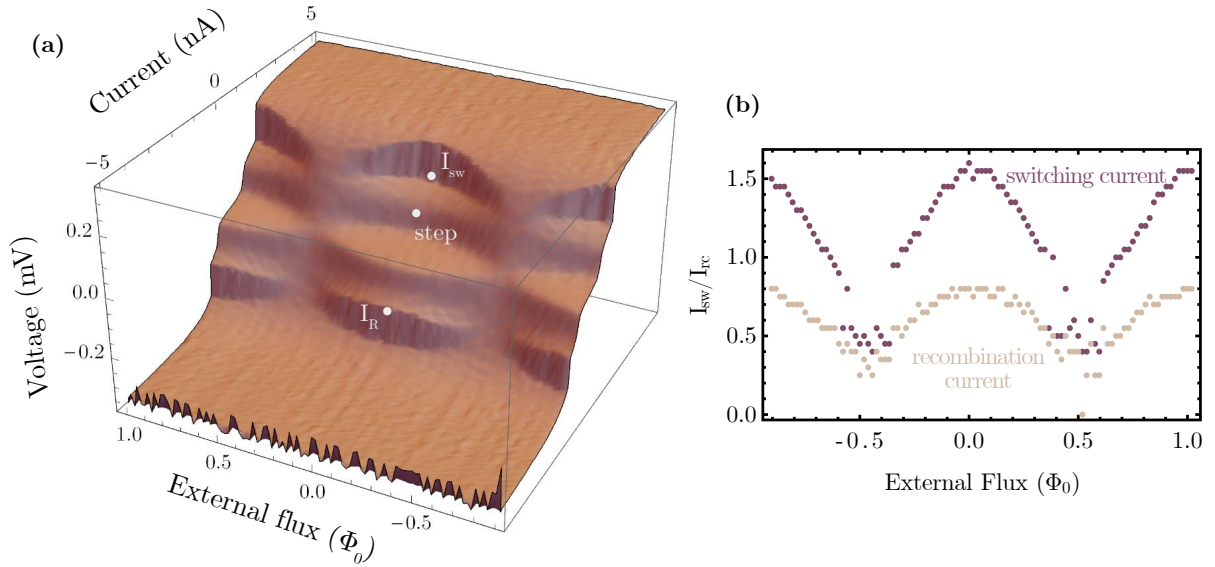
Figure 5.5: **SQUID + coil.** (a) 3D plot of IV curves vs. external flux for a SQUID in between two coils. Coil parameters reported in Table 5.1. Switching and return current as well as step location are identified for $\Phi_{ext} = 0$. (b) switching and return currents of the SQUID as a function of external flux extracted from the data shown in the left panel.
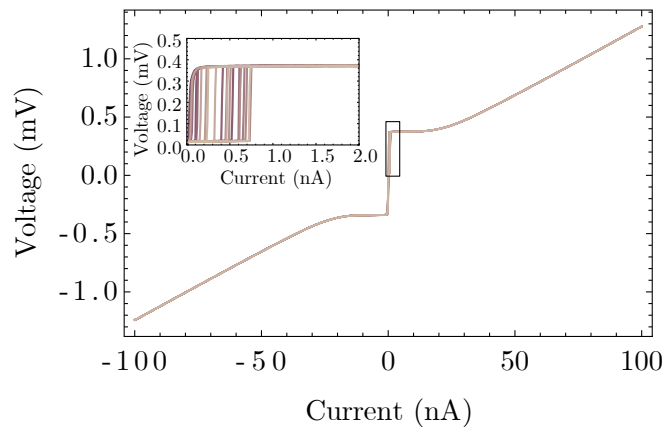
Figure 5.6: **SQUID + coil with resistors.** IV curves of a SQUID in series with two planar coils and two resistors with DC resistance 100k Ω. The indent is a close up of the IV curve around zero current showing the small but still present zero voltage state.

the sample without resistors and shows the IV curve for different values of the external magnetic field which determines the value of $E_J(\Phi_{ext})$. The junctions in the SQUID had nominal size of 200×200 nm^2 and ane extracted critical current of 32 nA. When adding the coils to the junction the first obvious change is a step in the IV curve, identified for $\Phi_{ext} = 0$ in 5.5(a). This effect is recognized as being due to changes in the impedance along the wire resulting in resonances [Tinkham, 1996; Grabert, 1992]. Figure 5.5(b) tracks the switching current and return current of the IV curve for different values of flux. As they are both dependent on the critical current and therefore the Josephson energy E_J they vary as a function of flux with a $|\cos(\Phi_{ext}/\Phi_0)|^2$ shape. The return current is consistently lower than the switching current indicating a significant level of hysteresis. As resistors were not included in this sample the IV curve was qualitatively similar to those measured on membranes from Section 5.2.2.

The same sample was cooled down in a PCB which included resistors in series to the coil and junction. The data can be seen in Fig. 5.6. The main plot shows a large view of the IV curve where all three junction states are visible, the inset is a closeup of the data in the black rectangle around 0 nA of current. The different lines correspond to different values of external flux. Once again the resistor has significantly decreased the value of the switching current but the junction is not in a completely high impedance environment as it still displays a zero voltage state instead of a Coulomb blockade.

As the expected result for this sample was to measure a Coulomb blockade away from

Coil turns	pitch (μm)	L (nH)	C (fF)	ν (GHz)	R (kΩ)
110	0.4	370	3.6	4.35	1800

Table 5.2: **Coil parameters.** Geometric parameters, simulated coil parameters and resistor used in the samples that produced Fig. 5.7

Phi$_{ext}$ $= \Phi_0/2$ it is possible to identify the potential reasons that this did not occur:

- The impedance is not high enough: this is possibly due to stray capacitance being to high and the inductance of the coil being too low.

- The setup is too noisy: Coulomb blockade measurements require very good isolation in order to avoid quasi-particles or high thermal fluctuations.

- The resistors are not suitable. The resistors used in these experiments are commercially bought and therefore are macroscopic in dimensions and are soldered on the PCB. This has the advantage of creating less localized heating that is more easily dispersed. However the large dimension will decrease the range of frequency in which it operates as a pure resistance due to large stray capacitance. Even though the junction is measured in DC the charge dynamics have a frequency component as discussed in Section 1.3.1 and this creates the risk of the resistor's range not covering the frequency required and therefore not serving its function.

The next part of this chapter attempts to work on these points and conclude weather these are limiting factors in our experiment.

5.3.2 INCREASING RESISTANCE

The fist attempt was to switch the resistor with one with a much higher DC resistance. The resistor used was from Vishay (S.N. MMU01020C1804FB300) with a DC resistance of 1.8 MΩ. The junction had nominal size of 200×250 nm^2 and a calculated critical current of 51 nA. The goal was to test the effect of changing the DC resistance on the sample. The results are show in Fig. 5.2 where one can see the 3D plot of IV curve versus external flux in panel (a) and the change in switching and return current vs external flux in panel (b). Immediately some differences emerge, specifically the lack of a pronounced hysteresis. This is shown in the fact that the switching current and the return current

Figure 5.7: **SQUID + coils + higher resistance.** (a) 3D plot of IV curves vs external flux for a SQUID in between between two coils. (b) Switching and return currents of the SQUID as a function of external flux extracted from the data shown in the left panel.

are very similar in value. A low hysteresis indicates a lowered quality factor of the junction. In Ref. [Tinkham, 1996] it is stated that a high impedance environment can reduce the effective quality factor of the junction which is consistent with this result, however this contradicts our previous observations where adding a resistor (in Sections 5.2.2 and 5.3.1) increased hysteresis. Both the switching and return current are much lower than the critical current extracted from the voltage state of the junction which is calculated to be around 14 nA. The lowering of the switching current is also a possible effect of the high impedance environment which favours phase fluctuations in the junction allowing it to jump to the voltage state at lower currents.

Nevertheless the junction is still displaying a zero voltage state rather than a Coulomb blockade. The resistor used in this experiment is much larger in size than the previously used one making it less likely to maintain its high resistance at higher frequency and therefore not providing the junction with a high impedance environment at the correct frequency.

From this test we are able to conclude that higher resistance is helpful but larger size resistors need to be avoided.

	Coil turns	pitch (μm)	L (nH)	C (fF)	ν (GHz)	R (kΩ)
Device 1	200	0.3	1600	11.5	2.20	100
Device 2	250	0.3	3400	12.7	1.40	100

Table 5.3: **Coil parameters.** Geometric parameters, simulated coil parameters and resistor used in the samples that produced Fig. 5.8

5.3.3 INCREASING IMPEDANCE

The following sample was optimized to have the highest possible impedance by means of increasing the coil inductance but also by trying to minimize the stray capacitance on-chip. The latter was realized by fabricating the device near the edge of the chip with small distance between the coil, junction and bonding pads that connect to the off chip resistors. Decreasing the length of the leads decreases the cross capacitance increasing the impedance of the sample. In addition the sample was removed from the copper box, which provides additional capacitance, but was still thermally anchored through a clip to the dilution refrigerator. Two devices were measured in this configuration with very different inductances giving a predicted impedance of 6.3 kΩ and 9.2 kΩ. This is not to be confused with the coil impedance as it is it includes the coil inductance L and the parasitic capacitance C_P as explained in Section 1.3.1. The parasitic capacitance is was simulated to be 40 fF for this design. The junctions had the same nominal size of 200×200 nm^2 and calculated critical currents of 52 nA and 46 nA.

Figure 5.8 shows IV curves vs. external flux and the extracted switching and return currents for both implementations. Notably the IV curve has gone back to being hysteretic and a step is again visible. Also interesting is the fact that at half a flux quantum the IV curve still shows a very small voltage plateau. This is possibly due to an asymmetry between the E_J of the two junctions in the SQUID. However no clear difference can be seen between the IV curves of the two devices indicating that the main limitation to the experiment isn't the on-chip impedance.
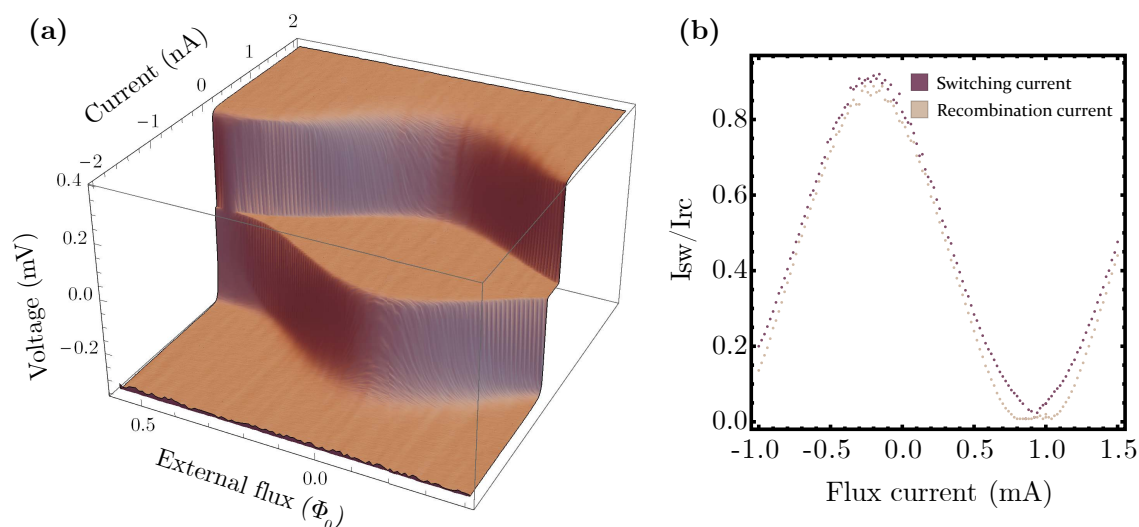
Device 1
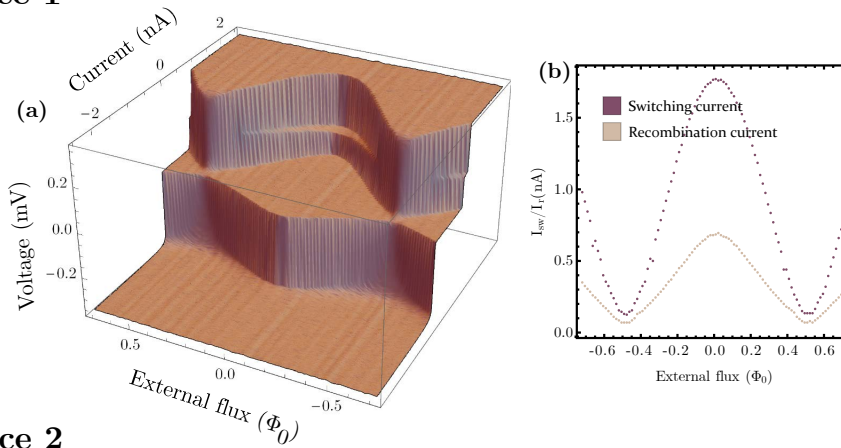
Device 2
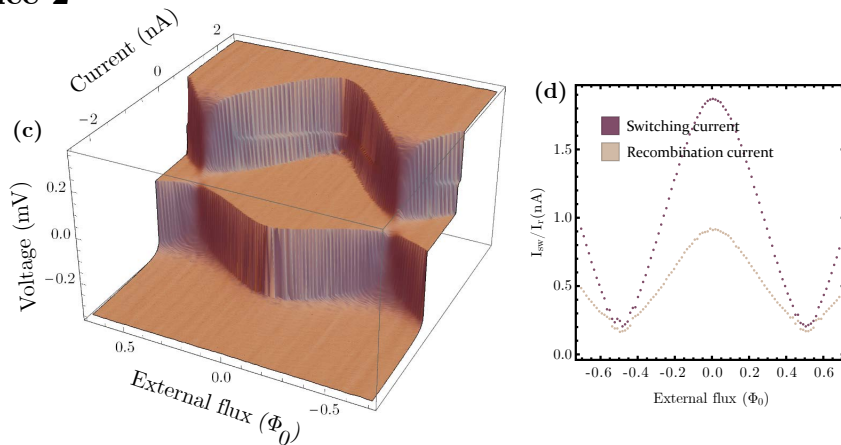
Figure 5.8: **SQUID + coil with higher impedance** (a),(c) 3D plot of IV curves vs. external flux for a SQUID in between two coils. (b),(d) Switching and return currents of the SQUID as a function of external flux extracted from the data shown in the left panel. Devices 1 and 2 correspond to the device parameters reported in Table 5.3

Device 1
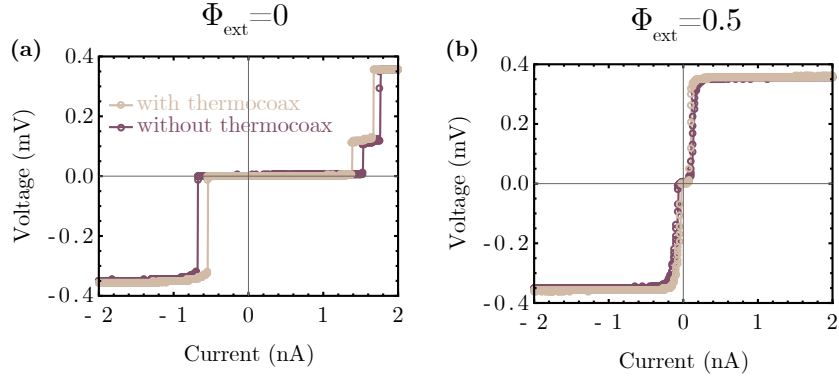
Device 2
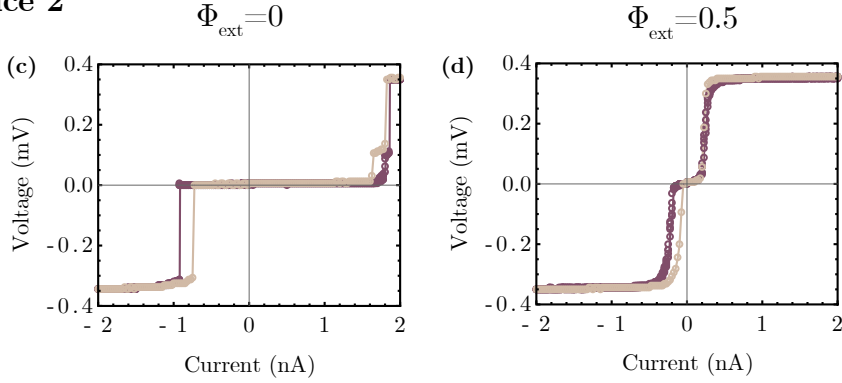
Figure 5.9: **SQUID + coil with higher impedance and thermocoax** Comparison between the IV curves of the devices with parameters reported in Table 5.3. The plots show each device at the 0 and 0.5 external flux points, these are the points where the Josephson energy is maximum and minimum respectively. The plot shows the curves measured with and without a thermocoax line filtering the input and output signals.

5.3.4 BETTER SHIELDING

In order to test weather noise is a potential limitation to the experiment the same samples as the previous section were measured using a Thermocoax line. Thermocoax is a highly absorbing material which has been shown to effectively filter quasiparticle noise [Cedergren, 2017]. This test was performed on the same sample as the previous section with parameters in Table 5.3.

From Fig. 5.9 one can see a very small change associated with adding the thermocoax. The only differences seem to be the shrinking of the switching and return current. Such a change is most likely due to aging of the Josephson junctions which is a process by which the Josephson energy decreases when the sample is in contact with the Oxygen present in

| Coil turns	pitch (μm)	L (nH)	C (fF)	ν (GHz)	R (kΩ)
110	0.4	370	3.6	4.35	100

Table 5.4: **Coil parameters.** Geometric parameters, simulated coil parameters and resistor used in the samples that produced Fig. 5.10

the atmosphere. The aging explanation is backed by the fact the normal state resistance increased by 5% indicating a reduction in E_J.

From this measurement we conclude that the quasiparticle poisoning is not a limiting factor of our measurement for the time being. This sample however did not include RF shielding which could also be a limiting factor.

5.3.5 CHANGING OFF-CHIP IMPEDANCE

Table 5.4 shows the coil parameters being the same as those presented in Section 5.3.1 and 5.3.2 samples, in this sample however the distance between the coils and junction was increased and the leads connecting the coils to the edge of the chip were decreased in width from 1 μm to 200 nm in an effort to reduce parallel capacitance on chip. This resulted in a simulated C_P of 45 fF. The junction has nominal size of 200×100 nm^2 and a calculated critical current of 25 nA. Once again the sample was removed from the copper box to avoid extra capacitance between the leads. In addition this sample was measured with a 2-probe configuration with the goal to additionally reduce capacitance before and after the resistor stage.

As presented in Section 2 of this work the samples are connected to a filter via a copper cable. For the tests done in this section two different cables were utilized. One where the corresponding input and output wire were in a twisted pair and ones where this was not the case. Making a twisted pair is often recommended as it avoids picking up magnetic noise, however it creates a larger capacitance between the input and output. Said capacitance should be countered by the resistor which turns the signal into a current bias, however as this measurement confirmed this effect was not reached.

Figure 5.10 shows results from the use of the two types of cables. Figure 5.10(a) shows the sample with the twisted pair cable. Here the data is similar to previous samples, specifically the sample displays a zero voltage state and appears to have no hysteresis.

Figure 5.10(b) is a series of IV curves around the half flux quantum displaced from one another for better visibility. These show how the zero voltage state gets smaller but does not disappear entirely.

Figure 5.10(c) is the same sample measured with the cable without the twisted pairs. In this sample a small Coulomb blockade like feature appears around the half flux quantum, indicated by the gray box. A close-up of this feature can be seen in Fig. 5.10(d) where again the IV curves can be seen as the external flux goes further from the half flux quantum (blue line). The feature disappears for E_J/E_C above 0.9 which is likely due to the fact that the critical voltage (i.e. the width of the plateau) decays exponentially as a function of E_J/E_C and probably gets too small to measure. The points represent $\pm V_C$ for the different values of E_J corresponding to the flux where $E_J^{\max}$ = 12 GHz adn E_C = 7.5 GHz. As they seem to correlate very well with the width of the plateau we can conclude that this is in fact a Coulomb blockade due to suppression of charge fluctuations.

From this test we can conclude that the resistors are not shielding from the rest of the circuitry and therefore are not functioning as intended. This could be for a number of reasons but the most plausible one is that the frequency range of such resistors is not sufficiently large to cover the charge dynamics sufficiently. Further investigations in this topic will require on-chip fabricated resistors that are smaller in size and hence will work for higher frequencies. A potential downfall to having smaller resistors is the fact that the smaller the size the more localized thermal noise they will produce. This has been a limitation for previous measurements of Coulomb blockade across a single junction [Kuzmin, 1994; Vora, 2017] but we hope that due to the length of the coil wire we can put a large effective distance between the resistor and the junction and therefore help thermalize the charges before they reach the junction.
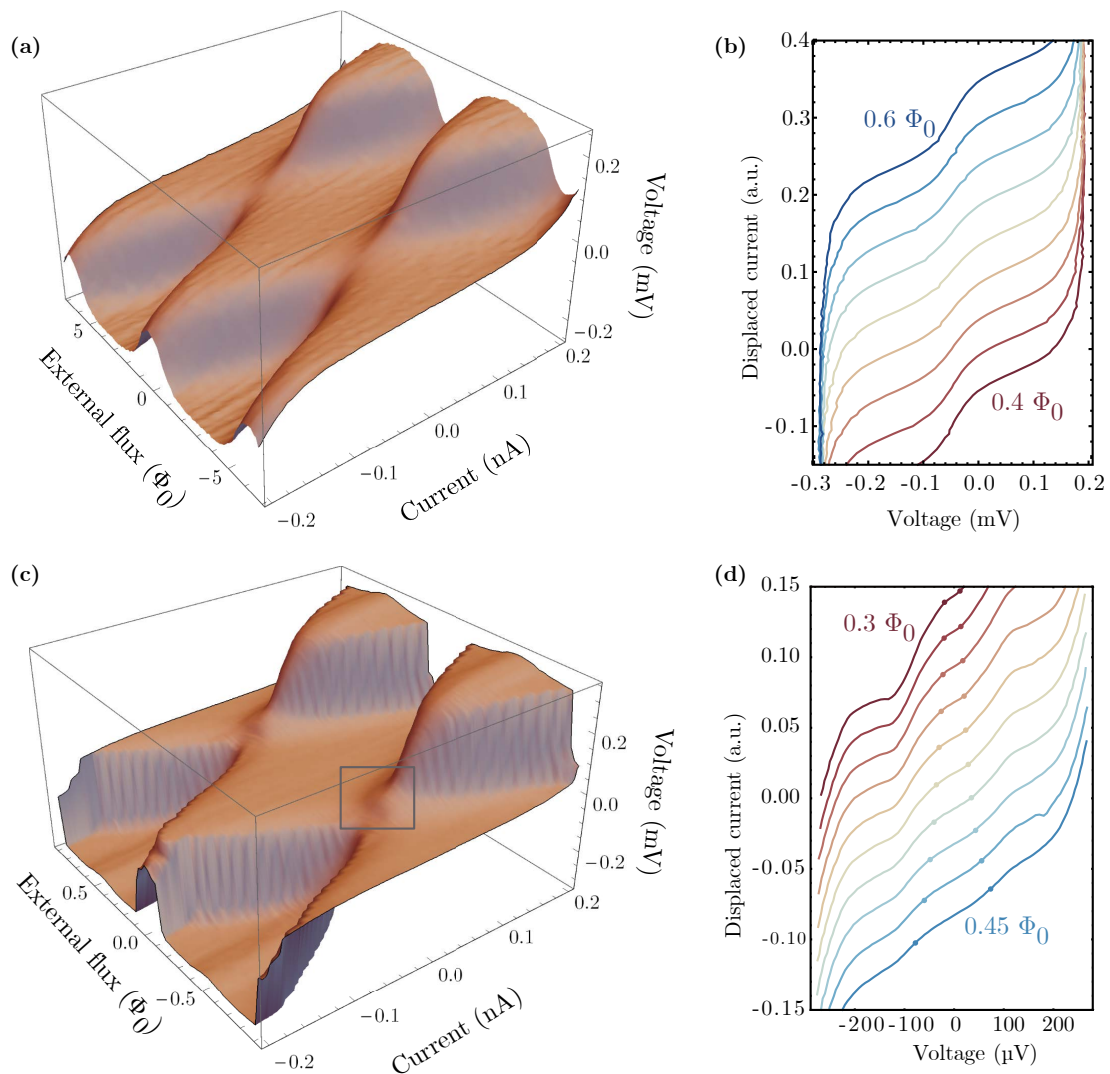
Figure 5.10: **SQUID + coil and different connections.** (a-b) Data collected from a device where the connection between the sample and the filter was done with a twisted pair cable. On the right several IV curves are shown for external fluxes in the range 0.4-0.6 Φ_0. The IV curves were displaced from one another for better visibility. (c-d) The same data sets for the same sample but where the connection cable used did not make twisted pairs out of input and output lines. The plot on the right is also a series of IV curves displaced for better visibility, the points represent calculations of the position of the critical voltage for $E_J^{max} = 12$ GHz and $E_C = 7.5$ GHz.

CHAPTER 6

CONCLUSIONS

This work concludes with a short summary of the main results followed by an outlook where possible continuations will be outlined.

6.1 GEOMETRIC SUPERINDUCTORS AS RESONATORS

In Chapter 3 we showed suspended aluminum coils to be linear low-loss geometric superinductor resonators that can be used as an ideal superinductance below their self-resonance frequency. These reached a characteristic impedance $Z_C \approx 5 \times R_Q$, about 80 times the previously claimed limitation for geometric inductors, $Z_0 = 377\Omega$ [Manucharyan, 2009; Manucharyan, 2012; Masluk, 2012; Kamenov, 2020].

Such a highly miniaturized microwave resonator with large zero point voltage fluctuations reaching $V_{ZPF} \approx 50\,\mu V$ that maintains a linearity of up to 10^8 photons is an attractive platform for hybrid devices. Losses were found to be as low as $Q_i \approx 8 \times 10^5$ at single photon powers despite the small gap sizes on the order of $100\,nm$ (see Fig. 3.1(c) in Section 3.2). In addition strong controllable magnetic coupling was shown to shorted feed-lines allowing for a wide range of Q_e.

A simple analytical model to guide future design choices was provided. Specifically the coil self-capacitance only relies on the radius and substrate used (see Figs. 3.4(d-f) and 3.5(a) in Section 3.3).

In the future even larger coil impedance could be obtained by etching rather than lift-off, which would enable even smaller coil pitch with better interfaces and lower TLS losses. This technique has already beed tested by other group memebers and is the method by which geometric inductors were fabricated in Ref. [Hassani, 2021]. Moreover the presented design and fabrication methods could also help to reliably increase the Z_C of kinetic superinductors.

6.2 GEOMETRIC SUPERINDUCTORS AS QUBITS

Following teh characterization of a the geometric superinductor this work presented two main applications, the first being the geometric RF-SQUID, i.e. a planar coil in series with

a Josephson junction. In Section 1.3.2 a wide range of parameters were presented and an attempt was made to unify and classify the zoo of RF-SQUID qubits according to the physics rather than their physical implementation. Then in Chapter 4 several geometric RF-SQUIDs were presented. The device design included two coils, one used as a readout resonator while the other was the superinductor of the qubit. This work presented only 2D implementation of high-impedance devices however flux qubits, heavy fluxoniums and inductively shunted transmon qubits were also implemented with geometric superinductors [Peruzzo, 2021; Hassani, 2021] showing the versatility of the geometric approach.

Due to the device configuration we observe simultaneous capacitive and inductive coupling between the qubit and the resonator and we provide a model and an algorithm that can efficiently fit the coupled RF-SQUID - resonator spectrum. We find couplings of the order of tens to hundreds of MHz achieved with very small coupling capacitance of 1 - 2 fF due to the small size and high impedance of both the qubit and the resonator - a feature that enables large capacitive coupling in the light fluxonium and quasi-charge regimes, seen in Table 4.3.

While the sensitivity to quasi-particle loss is expected to be much smaller compared to kinetic inductance qubits, the observed high flux noise amplitude is a potential disadvantage. In Section 4.4 the flux noise amplitudes extracted were found to be several orders of magnitude higher than those of qubits relying on kinetic inductance [Nguyen, 2019] (see Table 4.4). This highlights the need for low flux dispersion by design, as achieved in the case of the measured quasi-charge qubit where T_2 is limited only by T_1 and the calculated shot noise limit. Other mitigation strategies include further miniaturization of the coil geometry in order to maximize the inductance per unit length as well as the use of materials with fewer magnetic surface defect states. On the positive side, this sensitivity points at other potential applications such as high precision quantum sensing of elementary spin systems.

The coherence and relaxation time will improve with more optimized design choices in future device generations but most importantly by increasing the quality factor of the inductor, for example by back-etching the handle wafer [Peruzzo, 2020], which would incidentally also allow to reach even lower values of E_L/E_C. The resulting further enhanced zero point phase fluctuations are a prerequisite towards the realization of degenerate ground state qubits, where the full protection requires Hamiltonian engineering with

carefully maintained circuit symmetries, a characteristics of top-down fabricated circuit elements.

Table 4.3 in Section 4.3 illustrates the low chip-to-chip variance of the capacitive and inductive energy of $< 1\%$ which is a key ingredient towards realizing hardware protected qubits in new parameter regimes in the near future.

6.3 GEOMETRIC SUPERINDUCTORS FOR QUANTUM METROLOGY

When it comes to the measurement of Coulomb blockade and dual Shapiro steps across a single junction, Section 5 concluded with the need to fabricate on-chip micro-resistors. The results presented in this work used commercially bought surface mount thin film resistors which were found not to shield the experiment sufficiently from the off-chip capacitance. This is due to the resistance decreasing as a function of frequency due to stray capacitance which renders the resistance ineffective at the desired frequency $1/(RC_S)$ (see Section 1.3.1). Reference [Lotkhov, 2013] lays out a recipe for TiOx resistors where Titanium is evaporated in the presence of Oxygen in the chamber.

Preliminary fabrication attempts to reproduce the results in [Lotkhov, 2013] were done in our cleanroom resulting in the data shown in Fig. 6.1. The resistor cross section had the nominal value of 200×10 nm, the evaporation was done with 0.2 sccm of Oxigen resulting in a chamber pressure of 1.5×10^{-6}. The resulting resistors are lower than what is ideal for this experiment (100 kΩ - 1 MΩ) and hence subsequent recipies will require an increased Oxygen flow.

Once an appropriate resistor recipe is found a comparison can be made between a Josephson junction sandwidched by closeby resistors and a similar sample where a suprinducting coil is placed between the two. Temperature sweeps similar to those done in Section 5 or the thermal characterization done in Ref. [Maibaum, 2011] would be able to quantify the thermalizing effect of the superinductor and reveal weather this strategy will be effective in reducing quasiparticles and thermal excitation sufficiently to reveal dual Shapiro steps. Given the parameters extracted in Chapter 5 a prediction of the shape of the dual Shapiro steps in the absence of temperature was done using the equations from Ref. [Arndt, 2018].
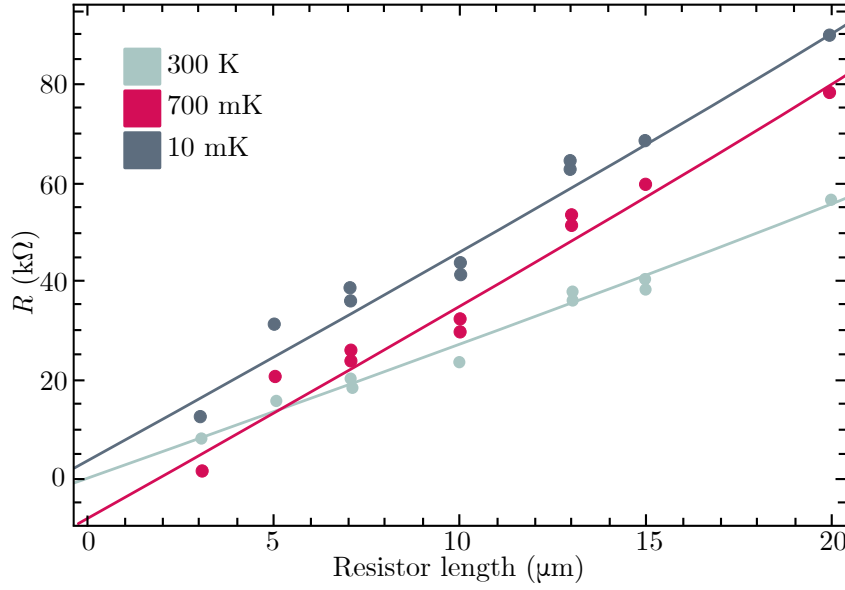
Figure 6.1: **Measurements of on-chip resistors.** Resistance vs length for TiOx resistors at 300 K, 700 mK and 10 mK. Line fits show the expected linear dependence
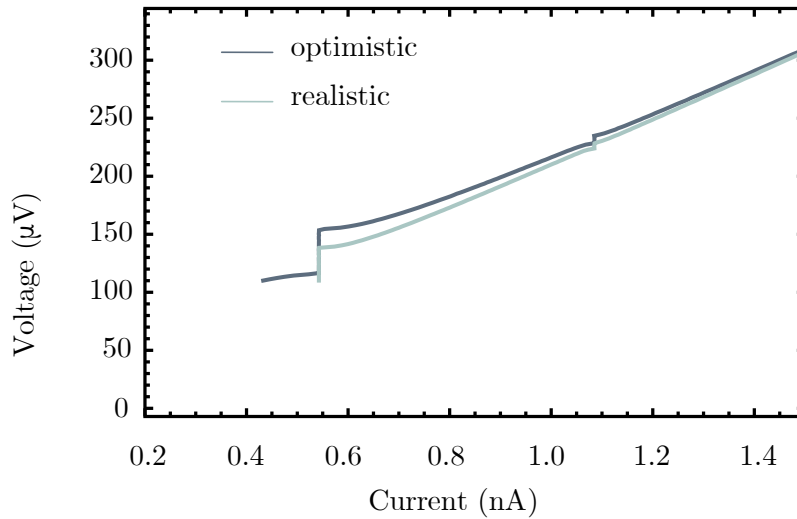
Figure 6.2: **Predicted dual Shapiro steps.** Calculated Shapiro steps for junction parameters $E_J = 10$ GHz and $E_C = 15$ GHz which give $V_C = 109\mu V$. Resistance is assumed to be $R = 200$ kΩ meaning $\omega_R C = 2\pi 1.97$ GHz. The two lines represent a realistic and optimistic estimation of the circuit impedance (12 kΩ and 22 kΩ) given by L = 1.5 μH and 5 μH and $C_p = 10$ fF.

The predicted steps are shown in Fig. 6.2 where the two lines represent a realistic and optimistic estimation of the circuit impedance. The optimistic version shows a wider step as predicted and therefore is going to be easier to measure even with some thermal fluctuations. Such an impedance could be reached with very small pitch coils with ultrahigh impedance (5 μH) and by even placing the sample on an SOI-BE substrate.

Bibliography

[Ambegaokar, 1969]   V. Ambegaokar and B. I. Halperin. "Voltage Due to Thermal Noise in the dc Josephson Effect". In: *Phys. Re. Lett.* 22.25 (June 1969), pp. 1364–1366. DOI: 10.1103/physrevlett.22.1364 (cit. on p. 6).

[Annunziata, 2010]   A. J Annunziata et al. "Tunable superconducting nanoinductors". In: *Nanotechnology* 21.44 (2010), p. 445202. URL: http://dx.doi.org/10.1088/0957-4484/21/44/445202 (cit. on p. 56).

[Arndt, 2018]   L. Arndt, A. Roy, and Fabian Hassler. "Dual Shapiro steps of a phase-slip junction in the presence of a parasitic capacitance". In: *Phys. Rev. B* 98.1 (July 2018), p. 014525. DOI: 10.1103/physrevb.98.014525 (cit. on pp. 9, 15, 16, 99).

[Aspelmeyer, 2013]   M. Aspelmeyer, T. J. Kippenberg, and F. Marquardt. "Cavity Optomechanics". In: (2013). URL: arXiv:1303.0733 (cit. on p. 21).

[Barzanjeh, 2017]   S. Barzanjeh et al. "Mechanical on-chip microwave circulator". In: *Nature Comm.* 8.1 (2017), p. 953. URL: https://doi.org/10.1038/s41467-017-01304-x (cit. on p. 21).

[Bell, 2012]   M. T. Bell et al. "Quantum Superinductor with Tunable Nonlinearity". In: *Phys. Rev. Lett.* 109 (13 Sept. 2012), p. 137003. DOI: 10.1103/PhysRevLett.109.137003. URL: https://link.aps.org/doi/10.1103/PhysRevLett.109.137003 (cit. on p. 11).

[Bianchetti, 2010]   R. Bianchetti. "Control and readout of a superconducting artificial atom". PhD thesis. ETH Zurich, 2010. URL: http://qudev.phys.ethz.ch/content/science/thesis/dr_Bianchetti.pdf (cit. on p. 65).

[Bianchetti, 2009]   R. Bianchetti et al. "Dynamics of dispersive single-qubit read-out in circuit quantum electrodynamics". In: *Phys. Rev. A* 80.4, 043840 (Oct. 2009), p. 043840. DOI: 10.1103/PhysRevA.80.043840. URL: http://link.aps.org/abstract/PRA/v80/e043840 (cit. on pp. 44, 47).

[Blackburn, 2014]   James A. Blackburn, Matteo Cirillo, and Niels Grønbech-Jensen. "Switching current distributions in Josephson junctions at very low temperatures". In: *EPL (Europhysics Letters)* 107.6 (Sept. 2014), p. 67001. DOI: 10.1209/0295-5075/107/67001 (cit. on pp. 6, 82).

[Blais, 2021]   Alexandre Blais et al. "Circuit quantum electrodynamics". In: *Rev. Mod. Phys.* 93.2 (May 2021), p. 025005. DOI: 10.1103/revmodphys.93.025005 (cit. on pp. 2, 17, 44).

[Brooks, 2013]   P. Brooks, A. Kitaev, and J. Preskill. "Protected gates for superconducting qubits". In: *Phys. Rev. A* 87.5 (May 2013), p. 052306. DOI: 10.1103/physreva.87.052306 (cit. on p. 23).

[Bylander, 2011]   J. Bylander et al. "Noise spectroscopy through dynamical decoupling with a superconducting flux qubit". In: *Nature Phys.* 7 (2011), pp. 565–570. DOI: doi:10.1038/nphys1994. URL: http://www.nature.com/nphys/journal/v7/n7/full/nphys1994.html (cit. on pp. 49, 51).

[Cedergren, 2017]   K. Cedergren et al. "Insulating Josephson Junction Chains as Pinned Luttinger Liquids". In: *Phys. Rev. Lett.* 119.16 (Oct. 2017), p. 167701. DOI: 10.1103/physrevlett.119.167701 (cit. on p. 92).

[Clarke, 2008]   J. Clarke and F. K. Wilhelm. "Superconducting quantum bits". In: *Nature* 453.7198 (June 2008), pp. 1031–1042. DOI: 10.1038/nature07128. URL: http://dx.doi.org/10.1038/nature07128 (cit. on p. 17).

[Dieterle, 2016]   P. B. Dieterle et al. "Superconducting Cavity Electromechanics on a Silicon-on-Insulator Platform". In: *Phys. Rev. Applied* 6.1

(July 2016), p. 014013. URL: https://link.aps.org/doi/10.1103/PhysRevApplied.6.014013 (cit. on p. 21).

[Dolan, 1977]   G. J. Dolan. "Offset masks for lift-off photoprocessing". In: *App. Phys. Lett.* 31.5 (Sept. 1977), pp. 337–339. DOI: 10.1063/1.89690 (cit. on p. 35).

[Earnest, 2018]   N. Earnest et al. "Realization of a Λ System with Metastable States of a Capacitively Shunted Fluxonium". In: *Phys. Rev. Lett.* 120 (15 May 2018), p. 150504. DOI: 10.1103/PhysRevLett.120.150504. URL: https://link.aps.org/doi/10.1103/PhysRevLett.120.150504 (cit. on p. 17).

[Fano, 1961]   U. Fano. "Effects of Configuration Interaction on Intensities and Phase Shifts". In: *Phys. Rev.* 124 (6 Dec. 1961), pp. 1866–1878. DOI: 10.1103/PhysRev.124.1866 (cit. on p. 44).

[Fink, 2010]   J. M. Fink. "Quantum nonlinearities in strong coupling circuit QED". PhD thesis. ETH Zurich, 2010 (cit. on p. 26).

[Fink, 2016]   J. M. Fink et al. "Quantum electromechanics on silicon nitride nanomembranes". In: *Nature Comm.* 7.1 (Aug. 2016). DOI: 10.1038/ncomms12396 (cit. on pp. 13, 21, 22, 28).

[Fulton, 1974]   T. A. Fulton and L. N. Dunkleberger. "Lifetime of the zero-voltage state in Josephson tunnel junctions". In: *Phys. Rev. B* 9.11 (June 1974), pp. 4760–4768. DOI: 10.1103/physrevb.9.4760 (cit. on p. 6).

[Gao, 2008a]   J. Gao. "The Physics of Superconducting Microwave Resonators". PhD thesis. California Institute of Technology, 2008 (cit. on pp. 44, 55, 56).

[Gao, 2008b]   J. Gao et al. "Equivalence of the Effects on the Complex Conductivity of Superconductor due to Temperature Change and External Pair Breaking". In: *Journal of Low Temp. Phys.* 151.1-2 (Jan. 2008), pp. 557–563. DOI: 10.1007/s10909-007-9688-z (cit. on p. 56).

[Göppl, 2008]   M. Göppl et al. "Coplanar Waveguide Resonators for Circuit Quantum Electrodynamics". In: *J. Appl. Phys.* 104 (July 2008), p. 113904.

DOI: 10.1063/1.3010859. URL: http://dx.doi.org/10.1063/1.3010859 (cit. on p. 26).

[Grabert, 1992] H. Grabert and M. H. Devoret. *Single Charge Tunneling*. Ed. by Hermann Grabert and Michel H. Devoret. Springer US, 1992. DOI: 10.1007/978-1-4757-2166-9 (cit. on p. 87).

[Groszkowski, 2018] P. Groszkowski et al. "Coherence properties of the 0-πqubit". In: *New Journal of Physics* 20.4 (Apr. 2018), p. 043053. DOI: 10.1088/1367-2630/aab7cd. URL: https://doi.org/10.1088/1367-2630/aab7cd (cit. on p. 23).

[Grünhaupt, 2018] L. Grünhaupt et al. "Loss Mechanisms and Quasiparticle Dynamics in Superconducting Microwave Resonators Made of Thin-Film Granular Aluminum". In: *Phys. Rev. Lett.* 121 (11 Sept. 2018), p. 117001. DOI: 10.1103/PhysRevLett.121.117001. URL: https://link.aps.org/doi/10.1103/PhysRevLett.121.117001 (cit. on p. 11).

[Grünhaupt, 2019] L. Grünhaupt et al. "Granular aluminium as a superconducting material for high-impedance quantum circuits". In: *Nature Materials* 18 (8 May 2019), pp. 816–819 (cit. on pp. 11, 68).

[Halpern, 1986] M. Halpern et al. "Far infrared transmission of dielectrics at cryogenic and room temperatures: glass, Fluorogold, Eccosorb, Stycast, and various plastics". In: *Applied Optics* 25.4 (Feb. 1986), p. 565. DOI: 10.1364/ao.25.000565 (cit. on p. 39).

[Hamilton, 1997] C.A. Hamilton, C.J. Burroughs, and S.P. Benz. "Josephson voltage standard-a review". In: *IEEE Transactions on Applied Superconductivity* 7.2 (1997), pp. 3756–3761. DOI: 10.1109/77.622234 (cit. on p. 7).

[Hassani, 2021] F. Hassani, M. Peruzzo, and J. M. Fink. *The inductively shunted transmon, in preparation.* 2021 (cit. on pp. 19, 97, 98).

[Haviland, 1991] D. B. Haviland et al. "Experimental evidence for the Coulomb blockade of Cooper pair tunneling and Bloch oscillations in single Josephson junctions". In: *Zeitschrift fur Physik B Condensed*

Matter 85.3 (Oct. 1991), pp. 339–347. DOI: `10.1007/bf01307629` (cit. on pp. 14, 15).

[Hazard, 2019]   T. M. Hazard et al. "Nanowire Superinductance Fluxonium Qubit". In: *Phys. Rev. Lett.* 122 (1 Jan. 2019), p. 010504. DOI: `10.1103/PhysRevLett.122.010504`. URL: `https://link.aps.org/doi/10.1103/PhysRevLett.122.010504` (cit. on pp. 11, 68, 74).

[Houck, 2008]   A. A. Houck et al. "Controlling the Spontaneous Emission of a Superconducting Transmon Qubit". In: *Phys. Rev. Lett.* 101.8 (Aug. 2008), pp. 080502–4. DOI: `10.1103/PhysRevLett.101.080502`. URL: `http://link.aps.org/abstract/PRL/v101/e080502` (cit. on p. 74).

[Josephson, 1962]   B. D. Josephson. "Possible new effects in superconductive tunnelling". In: *Phys. Lett.* 1.7 (July 1962), pp. 251–253. DOI: `10.1016/0031-9163(62)91369-0`. URL: `http://www.sciencedirect.com/science/article/B6X44-47RBX8S-5/2/31fc71946bd983d4a8fd06a69e77` (cit. on p. 3).

[Kalaee, 2019]   M. Kalaee et al. "Quantum electromechanics of a hypersonic crystal". In: *Nature Nanotech.* 14.4 (Feb. 2019), pp. 334–339. DOI: `10.1038/s41565-019-0377-2` (cit. on p. 28).

[Kamenov, 2020]   P. Kamenov et al. "Granular Aluminum Meandered Superinductors for Quantum Circuits". In: *Phys. Rev. App.* 13 (5 May 2020), p. 054051. DOI: `10.1103/PhysRevApplied.13.054051`. URL: `https://link.aps.org/doi/10.1103/PhysRevApplied.13.054051` (cit. on pp. 11, 97).

[Kitaev, 2006]   A. Kitaev. "Protected qubit based on a superconducting current mirror". 2006. URL: `https://arxiv.org/abs/cond-mat/0609441` (cit. on p. 23).

[Kjaergaard, 2020]   M. Kjaergaard et al. "Superconducting Qubits: Current State of Play". In: *Ann. Rev. of Cond. Matt. Phys.* 11.1 (Mar. 2020), pp. 369–395. DOI: `10.1146/annurev-conmatphys-031119-050605` (cit. on p. 63).

[Koch, 2021]   J. Koch and P. Groszkowski. *scqubits: a Python package for superconducting qubits*. 2021. URL: https://arxiv.org/pdf/2107.08552.pdf (cit. on pp. 21, 73).

[Koch, 2007]   J. Koch et al. "Charge-insensitive qubit design derived from the Cooper pair box". In: *Phys. Rev. A* 76.4, 042319 (2007), p. 042319. DOI: 10.1103/PhysRevA.76.042319. URL: http://link.aps.org/abstract/PRA/v76/e042319 (cit. on pp. 9, 17).

[Koch, 2009]   J. Koch et al. *Charging effects in the inductively shunted Josephson junction*. 2009 (cit. on p. 9).

[Krantz, 2019]   P. Krantz et al. "A quantum engineer's guide to superconducting qubits". In: *Applied Physics Reviews* 6.2 (July 2019), p. 021318. DOI: 10.1063/1.5089550 (cit. on pp. 2, 17).

[Krueger, 1972] W. H. Krueger and S. R. Pollack. "The initial oxidation of aluminum thin films at room temperature". In: *Surface Science* 30.2 (1972), pp. 263–279. DOI: https://doi.org/10.1016/0039-6028(72)90002-7. URL: https://www.sciencedirect.com/science/article/pii/0039602872900027 (cit. on p. 35).

[Kuzmin, 1992]   L S Kuzmin and D B Haviland. "Bloch oscillations and Coulomb blockade of Cooper pair tunneling in ultrasmall Josephson junctions". In: *Physica Scripta* T42 (Jan. 1992), pp. 171–176. DOI: 10.1088/0031-8949/1992/t42/029. URL: https://doi.org/10.1088/0031-8949/1992/t42/029 (cit. on p. 14).

[Kuzmin, 1994]   L. Kuzmin et al. "Linewidth of Bloch oscillations in small Josephson junctions". In: *Phys. B: Cond. Matt.* 203.3 (1994), pp. 376–380. DOI: https://doi.org/10.1016/0921-4526(94)90083-3. URL: https://www.sciencedirect.com/science/article/pii/092145269490083-3 (cit. on pp. 15, 94).

[Kuzmin, 1991]   L. S. Kuzmin and D. B. Haviland. "Observation of the Bloch oscillations in an ultrasmall Josephson junction". In: *Phys. Rev. Lett.* 67 (20 Nov. 1991), pp. 2890–2893. DOI: 10.1103/PhysRevLett.67.2890. URL: https://link.aps.org/doi/10.1103/PhysRevLett.67.2890 (cit. on p. 14).

[Lotkhov, 2013]   S. V Lotkhov. "Ultra-high-ohmic microstripline resistors for Coulomb
                    blockade devices". In: *Nanotechnology* 24.23 (May 2013), p. 235201.
                    DOI: 10.1088/0957-4484/24/23/235201 (cit. on p. 99).

[Maibaum, 2011]   F. Maibaum, S. V. Lotkhov, and A. B. Zorin. "Towards the obser-
                    vation of phase-locked Bloch oscillations in arrays of small Joseph-
                    son junctions". In: *Phys. Rev. B* 84 (17 Nov. 2011), p. 174514. DOI:
                    10.1103/PhysRevB.84.174514. URL: http://link.aps.org/
                    doi/10.1103/PhysRevB.84.174514 (cit. on p. 99).

[Maleeva, 2014]   N. Maleeva et al. "Electrodynamics of a planar Archimedean spiral
                    resonator". In: (2014). arXiv: 1411.5823 [cond-mat.supr-con]
                    (cit. on p. 12).

[Maleeva, 2018]   N. Maleeva et al. "Circuit quantum electrodynamics of granular
                    aluminum resonators". In: *Nature Comm.* 9.1 (Sept. 2018). DOI:
                    10.1038/s41467-018-06386-9 (cit. on pp. 12, 55).

[Manucharyan, 2012] V. E. Manucharyan. "Superinductance". PhD thesis. Yale Univer-
                    sity, 2012 (cit. on pp. 2, 11, 97).

[Manucharyan, 2009] V. E. Manucharyan et al. "Fluxonium: Single Cooper-Pair Circuit
                    Free of Charge Offsets". In: *Science* 326.5949 (2009), pp. 113–
                    116. DOI: 10.1126/science.1175552. eprint: http://www.
                    sciencemag.org/content/326/5949/113.full.pdf. URL:
                    http://www.sciencemag.org/content/326/5949/113.abstract
                    (cit. on pp. 11, 17, 68, 97).

[Manucharyan, 2010] Vladimir E. Manucharyan et al. *Evidence for coherent quantum
                    phase-slips across a Josephson junction array.* Dec. 2010. eprint:
                    1012.1928 (cit. on p. 8).

[Masluk, 2012]   N. A. Masluk et al. "Microwave Characterization of Josephson
                    Junction Arrays: Implementing a Low Loss Superinductance". In:
                    Phys. Rev. Lett. 109 (13 Sept. 2012), p. 137002. DOI: 10.1103/
                    PhysRevLett.109.137002. URL: http://link.aps.org/doi/
                    10.1103/PhysRevLett.109.137002 (cit. on pp. 11, 55, 97).

[McCumber, 1968]   D. E. McCumber. "Effect of ac Impedance on dc Voltage-Current
                    Characteristics of Superconductor Weak-Link Junctions". In: *J.*

Appl. Phys. 39.7 (1968), pp. 3113–3118. DOI: 10.1063/1.1656743. URL: http://link.aip.org/link/?JAP/39/3113/1 (cit. on p. 4).

[Mogensen, 2018]   P. K. Mogensen and A. N. Riseth. "Optim: A mathematical optimization package for Julia". In: *Journal of Open Source Software* 3.24 (2018), p. 615. DOI: 10.21105/joss.00615. URL: https://doi.org/10.21105/joss.00615 (cit. on p. 67).

[Mohan, 1999]   S. S. Mohan et al. "Simple accurate expressions for planar spiral inductances". In: *IEEE Journal of Solid-State Circuits* 34.10 (Oct. 1999), pp. 1419–1424. DOI: 10.1109/4.792620 (cit. on p. 11).

[Mooij, 2006]   J. E. Mooij and Yu. V. Nazarov. "Superconducting nanowires as quantum phase-slip junctions". In: *Nature Phys.* 2.3 (2006), pp. 169–172. DOI: 10.1038/nphys234. URL: https://doi.org/10.1038/nphys234 (cit. on p. 8).

[Nguyen, 2019]   L. B. Nguyen et al. "High-Coherence Fluxonium Qubit". In: *Phys. Rev. X* 9.4 (Nov. 2019), p. 041041. URL: https://link.aps.org/doi/10.1103/PhysRevX.9.041041 (cit. on pp. 11, 17, 20, 98).

[Niepce, 2019]   D. Niepce, J. Burnett, and J. Bylander. "High Kinetic Inductance NbN Nanowire Superinductors". In: *Phys. Rev. App.* 11 (4 Apr. 2019), p. 044014. DOI: 10.1103/PhysRevApplied.11.044014. URL: https://link.aps.org/doi/10.1103/PhysRevApplied.11.044014 (cit. on p. 55).

[Pechenezhskiy, 2020]   I. V. Pechenezhskiy et al. "The superconducting quasicharge qubit". In: *Nature* 585.7825 (Sept. 2020), pp. 368–371. DOI: 10.1038/s41586-020-2687-9 (cit. on pp. 9, 11, 17, 20, 68).

[Peltonen, 2018]   J. T. Peltonen et al. "Hybrid rf SQUID qubit based on high kinetic inductance". In: *Scientific Reports* 8.1 (2018), p. 10033. URL: https://doi.org/10.1038/s41598-018-27154-1 (cit. on p. 68).

[Peruzzo, 2020]   M. Peruzzo et al. "Surpassing the Resistance Quantum with a Geometric Superinductor". In: *Phys. Rev. Applied* 14 (4 Oct. 2020), p. 044055. DOI: 10.1103/PhysRevApplied.14.044055. URL:

https://link.aps.org/doi/10.1103/PhysRevApplied.14.044055 (cit. on pp. 10, 74, 98).

[Peruzzo, 2021]   M. Peruzzo et al. *Geometric superinductance qubits: Controlling phase delocalization across a single Josephson junction.* 2021. arXiv: 2106.05882 [quant-ph] (cit. on pp. 17, 67, 98).

[Piquemal, 2000]   F. Piquemal and G. Genevs. "Argument for a direct realization of the quantum metrological triangle". In: *Metrologia* 37.3 (June 2000), pp. 207–211. DOI: 10.1088/0026-1394/37/3/4. URL: https://doi.org/10.1088/0026-1394/37/3/4 (cit. on p. 14).

[Pop, 2010]   I. M. Pop et al. "Measurement of the effect of quantum phase slips in a Josephson junction chain". In: *Nat. Phys.* (2010), pp. 589–592. DOI: doi:10.1038/nphys1697 (cit. on p. 8).

[Pop, 2014]   I. M. Pop et al. "Coherent suppression of electromagnetic dissipation due to superconducting quasiparticles". In: *Nature* 508.7496 (May 2014), pp. 369–372. DOI: 10.1038/nature13017 (cit. on pp. 18, 68).

[Pozar, 1993]   D. M. Pozar. *Microwave Engineering.* Addison-Wesley Publishing Company, 1993 (cit. on p. 26).

[Reale, 1974]   C. Reale. "Thickness and temperature dependence of the critical magnetic field of thin superconducting films of the aluminium group metals". In: *Acta Physica* 37 (June 1974), pp. 53–60. DOI: https://doi.org/10.1007/BF03157926 (cit. on p. 56).

[Rigetti, 2012]   C. Rigetti et al. "Superconducting qubit in a waveguide cavity with a coherence time approaching 0.1 ms". In: *Physical Review B* 86.10 (Sept. 2012), p. 100506. DOI: 10.1103/physrevb.86.100506 (cit. on pp. 23, 71).

[Scherer, 2012]   H. Scherer and B. Camarota. "Quantum metrology triangle experiments: a status review". In: *Measurement Science and Technology* 23.12 (Nov. 2012), p. 124010. DOI: 10.1088/0957-0233/23/12/124010. URL: https://doi.org/10.1088/0957-0233/23/12/124010 (cit. on p. 14).

[Scherer, 2019]   H. Scherer and H. W. Schumacher. "Single-Electron Pumps and Quantum Current Metrology in Revised SI". In: *Annalen der Physik* 531.5 (2019), p. 1800371. DOI: https://doi.org/10.1002/andp.201800371 (cit. on p. 14).

[Schoelkopf, 2003]   R. J. Schoelkopf et al. "Qubits as Spectrometers of Quantum Noise". In: *Quantum Noise in Mesoscopic Physics*. Ed. by Yuli V. Nazarov. Dordrecht: Springer Netherlands, 2003, pp. 175–203. DOI: 10.1007/978-94-010-0089-5_9. URL: https://doi.org/10.1007/978-94-010-0089-5_9 (cit. on p. 74).

[Schuster, 2007]   D. I. Schuster. "Circuit Quantum Electrodynamics". PhD thesis. Yale University, 2007 (cit. on p. 44).

[Shapiro, 1963]   S. Shapiro. "Josephson Currents in Superconducting Tunneling: The Effect of Microwaves and Other Observations". In: *Phys. Rev. Lett.* 11.2 (July 1963), pp. 80–82. DOI: 10.1103/physrevlett.11.80 (cit. on p. 7).

[Somoroff, 2021]   A. Somoroff et al. *Millisecond coherence in a superconducting qubit.* 2021. arXiv: 2103.08578 [quant-ph] (cit. on pp. 17, 20, 23).

[Stewart, 1968]   W.C. Stewart. "Current-voltage characteristics of Josephson junctions". In: *Appl. Phys. Lett.* 12 (1968), p. 277 (cit. on p. 4).

[Szep, 2021]   G. Szep and M. Peruzzo. *Hamiltonian optimization github repository.* 2021. URL: https://github.com/gszep/hamiltonian-optimisation (cit. on p. 67).

[Teufel, 2011]   J. D. Teufel et al. "Circuit cavity electromechanics in the strong-coupling regime". In: *Nature* 471.7337 (Mar. 2011), pp. 204–208. URL: http://dx.doi.org/10.1038/nature09898 (cit. on p. 22).

[Tinkham, 1996]   M. Tinkham. *Introduction to Superconductivity.* McGraw-Hill International Editions, 1996 (cit. on pp. 3, 8, 84, 87, 89).

[Toth, 2017]   L. D. Toth et al. "A dissipative quantum reservoir for microwave light using a mechanical oscillator". In: *Nat. Phys.* advance online publication (May 2017). URL: http://dx.doi.org/10.1038/nphys4121 (cit. on p. 28).

[Ulrich, 2016]   J. Ulrich and F. Hassler. "Dual approach to circuit quantization using loop charges". In: *Phys. Rev. B* 94 (9 Sept. 2016), p. 094505. DOI: 10.1103/PhysRevB.94.094505. URL: https://link.aps.org/doi/10.1103/PhysRevB.94.094505 (cit. on pp. 2, 8, 9).

[Visser, 2011]   P. J. de Visser et al. "Number Fluctuations of Sparse Quasiparticles in a Superconductor". In: *Phys. Rev. Lett.* 106 (16 Apr. 2011), p. 167004. DOI: 10.1103/PhysRevLett.106.167004. URL: http://link.aps.org/doi/10.1103/PhysRevLett.106.167004 (cit. on p. 57).

[Vool, 2017]   U. Vool and M. H. Devoret. "Introduction to quantum electromagnetic circuits". In: *International Journal of Circuit Theory and Applications* 45.7 (June 2017), pp. 897–934. DOI: 10.1002/cta.2359 (cit. on pp. 8, 17).

[Vool, 2018]   U. Vool et al. "Driving Forbidden Transitions in the Fluxonium Artificial Atom". In: *Phys. Rev. App.* 9.5 (May 2018), p. 054046. DOI: 10.1103/physrevapplied.9.054046 (cit. on p. 20).

[Vora, 2017]   H. Vora et al. "Modeling Bloch oscillations in nanoscale Josephson junctions". In: *Phys. Rev. B* 96.5 (Aug. 2017), p. 054505. DOI: 10.1103/physrevb.96.054505 (cit. on pp. 15, 94).

[Wallraff, 2003]   A. Wallraff et al. "Switching current measurements of large area Josephson tunnel junctions". In: *Review of Scientific Instruments* 74.8 (Aug. 2003), pp. 3740–3748. DOI: 10.1063/1.1588752 (cit. on p. 82).

[Wallraff, 2005]   A. Wallraff et al. "Approaching Unit Visibility for Control of a Superconducting Qubit with Dispersive Readout". In: *Phys. Rev. Lett.* 95 (Aug. 2005), p. 060501. URL: http://link.aps.org/abstract/PRL/v95/e060501 (cit. on pp. 44, 47, 48).

[Wang, 2019]   J. Wang and W. D. Oliver. "An aluminium superinductor". In: *Nature Materials* 18.8 (2019), pp. 775–776. URL: https://doi.org/10.1038/s41563-019-0401-9 (cit. on p. 11).

[Washburn, 1985]   S. Washburn et al. "Effects of Dissipation and Temperature on Macroscopic Quantum Tunneling". In: *Phys. Rev. Lett.* 54.25 (June

1985), pp. 2712–2715. DOI: 10.1103/physrevlett.54.2712 (cit. on p. 6).

[Yan, 2013]   F. Yan et al. "Rotating-frame relaxation as a noise spectrum analyser of a superconducting qubit undergoing driven evolution". In: *Nature Comm.* 4.1 (Aug. 2013). DOI: 10.1038/ncomms3337 (cit. on p. 49).

[Yan, 2016]   F. Yan et al. "The flux qubit revisited to enhance coherence and reproducibility". In: *Nature Comm.* 7.1 (Nov. 2016). DOI: 10.1038/ncomms12964 (cit. on pp. 19, 73).

[Zemlicka, 2015]   M. Zemlicka et al. "Finite quasiparticle lifetime in disordered superconductors". In: *Phys. Rev. B* 92.22 (Dec. 2015), p. 224506. DOI: 10.1103/physrevb.92.224506 (cit. on p. 57).

[Zhang, 2021]   H. Zhang et al. "Universal Fast-Flux Control of a Coherent, Low-Frequency Qubit". In: *Phys. Rev. X* 11.1 (Jan. 2021), p. 011010. DOI: 10.1103/physrevx.11.011010 (cit. on pp. 20, 70).

[Zhu, 2013]   G. Zhu et al. "Circuit QED with fluxonium qubits: Theory of the dispersive regime". In: *Phys. Rev. B* 87.2 (Jan. 2013), p. 024510. DOI: 10.1103/physrevb.87.024510 (cit. on p. 45).

APPENDIX A

NANOFABRICATION RECIPES

A.1 COIL ONLY DEVICES

A.1.1 COILS ON SI

Coils on Si		
Layer	Step	Notes
1 - Holes and markers	**Cleaning** 5min in Acetone (ACE) ultrasonication (uc) power 9, 5 min in Isopropyl Alcohol (IPA) uc power 9	
	Spin & Bake spin CSAR AR-P 6200.13 at 6 krpm (acceleration 1.5krpm/s), height 300 nm. Bake at 160 ^{o}C for 2 min	
	Ebeam lithography write coils with 0.8 nm beam (dose = 300-330 μC/cm^2 with PEC) and the ground and launchers with 100-200 nA beam (dose = 250-270 μC/cm^2 with PEC)	Coils are overdosed in order to avoid breaks in the coil.
	Develop in AR 600-549 developer for 1 min then rinse for 30 s in IPA	
	Evaporate 80-100 nm of Al at a rate of 1 nm/s	For better chamber pressure evaporate Ti for 3 min at 0.2 nm/s while the sample is rotated to avoid deposition.
	Lift-off in N-Methyl-2-pyrrolidone (NMP) on a hot plate at 140 ^{o}C (hot plate temp.) for 30+ min	For cleaner/more effective lift-off use a pipette

A.1.2 COILS ON SOI

Coils on SOI		
Layer	Step	Notes
1 - Holes and markers	**Cleaning** 5 min in ACE ultrasonication (uc) power 9, 5 min in IPA uc power 9	
	Spin & Bake spin CSAR AR-P 6200.13 at 6krpm (acceleration 1.5 krpm/s), height 300 nm. Bake at 160 ^{o}C for 2 min	
	Ebeam lithography write holes and markers with 0.8 nm beam (dose = 300-330 μC/cm^2 with PEC)	Holes are purpusefully overdosed
	Develop in AR 600-549 developer for 1 min then rinse for 30 s in IPA	
	ICP etch with C_4F_8 and SF_6 for 2 min	Etch time will vary, shorter etch times risk not etching through all the holes
	Lift-off in NMP on hot plate at 140 ^{o}C for 10 min then uc for 2 min, rinse in ACE and IPA with 2 min uc at power 2	
2 - Coils	**Cleaning** 5min in ACE ultrasonication (uc) power 9, 5min in IPA uc power 9	
	Spin & Bake spin CSAR 13% at 6 krpm (acceleration 1.5 krpm/s), height 300 nm. Bake at 160 ^{o}C for 2 min	
	Ebeam lithography write coils with 0.8 nm beam (dose = 300-330 μC/cm^2 with PEC) and the ground and launchers with 100-200 nA beam (dose = 250-270 μC/cm^2 with PEC)	Coils are purpusefully overdosed in order to avoid breaks in the coil.
	Develop in AR 600-549 developer for 1 min then rinse for 30 s in IPA	

	Evaporate 80-100 nm of Al at a rate of 1 nm/s	For better chamber pressure evaporate Ti for 3 min at 0.2 nm/s while sample is rotated to avoid deposition
	Lift-off in NMP on hot plate at 140 ^{o}C for 30+ min then uc for 2 min, rinse in ACE and IPA with 2 min uc at power 2	For cleaner/more effective lift-off use a pipette
	HF vapour in a Memstar machine with 18 T pressure, 2 mg of water for 10000 s or 16 T for 24000 s	Use longer recipe if shorter recipe leaves flouridization on the sample

A.1.3 COILS ON SOI - BACKETCHED

Coils on SOI - Backetched		
Layer	Step	Notes
1 - Holes and markers	**Cleaning** 5 min in ACE ultrasonication (uc) power 9, 5min in IPA uc power 9	
	Spin & Bake spin CSAR AR-P 6200.13 at 6 krpm (acceleration 1.5 krpm/s), height 300 nm. Bake at 160 ^{o}C for 2min	
	Ebeam lithography write holes and markers with 0.8 nm beam (dose = 300-330 μC/cm^2 with PEC)	Holes are purpusefully overdosed
	Develop in AR 600-549 developer for 1 min then rinse for 30 s in IPA	
	ICP etch with C_4F_8 and SF_6 for 2 min	Etch time will vary, shorter etch times risk not etching through all the holes

	Lift-off in NMP on hot plate at 140 ^{o}C for 10 min then uc for 2 min, rinse in ACE and IPA with 2 min uc at power 2	
2 - Coils	**Cleaning** 5min in ACE ultrasonication (uc) power 9, 5 min in IPA uc power 9	
	Spin & Bake spin CSAR AR-P 6200.13 at 6 krpm (acceleration 1.5 krpm/s), height 300 nm. Bake at 160 ^{o}C for 2 min	
	Ebeam lithography write coils with 0.8 nm beam (dose = 300-330 μC/cm^2 with PEC) and the ground and launchers with 100-200 nA beam (dose = 250-270 μC/cm^2 with PEC)	Coils are purpusefully over-dosed in order to avoid breaks in the coil.
	Develop in AR 600-549 developer for 1 min then rinse for 30 s in IPA	
	Evaporate 80-100 nm of Al at a rate of 1 nm/s	For better chamber pressure evaporate Ti for 3 min at 0.2 nm/s while sample is rotated to avoid deposition
	Lift-off in NMP on hot plate at 140 ^{o}C for 30+ min, rinse in ACE and IPA with 2 min uc at power 2	For cleaner/more effective lift-off use a pipette
Backetch	**Spin & Bake** spin LOR 5B at 4kpm (acc 1.5 krpm/s), height 600 nm. Bake at 180 ^{o}C for 2 min	repeat 2-3 times
Flip chip	**Spin & Bake** spin PMMA 950k 4% at 4 krpm (acc 1.5 krpm/s), height 270 nm. Bake at 170 ^{o}C for 3 min	
	Ebeam lithography entire chip except squares directly under the coil devices with a large beam (dose = 700 μC/cm^2 no PEC)	

	Evaporate 50 nm of Cr at a rate of 1 nm/s	
	Lift-off in Acetone at 40 ^{o} for 30+ min	
	ICP etch with C_4F_8 and SF_6 with a customized Bosh process	
Flip chip back	**Lift-off** in NMP on hot plate at 140 ^{o}C for 30+ min, rinse in ACE and IPA	
	HF vapour in a Memstar machine with 16 T pressure, 2 mg of water for 24000 s	place the chip in an elevated manner such that the open squares under the devices are reachable with the vHF

A.2 COILS WITH JOSEPHSON JUNCTIONS

Fluxonium and Coulomb blocakde chip		
Layer	Step	Notes
1 - Holes and markers	**Cleaning** 5min in ACE ultrasonication (uc) power 9, 5min in IPA uc power 9	
	Spin & Bake spin CSAR AR-P 6200.13 at 6 krpm (acceleration 1.5 krpm/s), height 300 nm. Bake at 160 ^{o}C for 2 min	
	Ebeam lithography write holes and markers with 0.8 nm beam (dose = 300-330 μC/cm^2 with PEC)	Holes are purpusefully overdosed
	Develop in AR 600-549 developer for 1 min then rinse for 30 s in IPA	
	ICP etch with (chemicals) for 2 min	Etch time will vary, shorter etch times risk not etching through all the holes

	Lift-off in NMP on hot plate at 140 ^{o}C for 10 min then uc for 2 min, rinse in ACE and IPA with 2 min uc at power 2	
2 - Ground and cross-wires	**Cleaning** 5min in ACE ultrasonication (uc) power 9, 5min in IPA uc power 9	
	Spin & Bake spin CSAR AR-P 6200.13 at 6 krpm (acceleration 1.5 krpm/s), height 300 nm. Bake at 160 ^{o}C for 2 min	
	Ebeam lithography write crosswires with 0.8 nm beam (dose = 300-330 μC/cm^2 with PEC) and the ground and launchers with 100-200 nA beam (dose = 250-270 μC/cm^2 with PEC)	
	Develop in AR 600-549 developer for 1 min then rinse for 30 s in IPA	
	Evaporate 80-100 nm of Al at a rate of 1 nm/s	For better chamber pressure evaporate Ti for 3 min at 0.2 nm/s while sample is rotated to avoid deposition
	Lift-off in NMP on hot plate at 140 ^{o}C for 30+ min then uc for 2 min, rinse in ACE and IPA with 2 min uc at power 2	For cleaner/more effective lift-off use a pipette
3 - Bridges	**Spin & Bake** spin LOR 5 at 4 krpm (acc 1 krpm), height 4000 nm. Bake at 180 ^{o} for 5 min then spin PMMA 950K 2% at 4 krpm (acceleration 1 krpm), height 70 nm. Bake at 180 ^{o} for 6min	

	Ebeam lithography write cutouts around coils excluding a 4 μm wide rectangle covering the crosswire with a large beam (eg. 250 nA) and dose = 700 μC/cm^2	
	Develop in MIBK:IPA (1:3) for 1 min and rinse in IPA for 30 s	
	Wet etch etch in MIF316 for 6 s then rinse in water for 5 s and IPA for 10 s, then remove the PMMA by shaking chip is ACE for 45 s and rinse in IPA for 10 s	The wet etch time (6 s) must be very accurate, it is recommended to remove chip after 5 s and transfer it to the water beaker during the 6th second
4 - Coils	**Spin & Bake** spin PMMA 600k 6% at 4krpm (acc 1krpm/s), height 520 nm, bake at 180 ^{o}C for 2 min then spin PMMA 950k 2% at 2krpm (acc 1krpm/s), height 70 nm, bake at 180 ^{o}C for 2 min	
	Ebeam lithography write coils with 0.8 nm beam (dose = 1200 μC/cm^2 with PEC)	Coils are purpusefully over-dosed in order to avoid breaks in the coil.
	Develop in MIBK:IPA (1:3) for 1 min and rinse in IPA for 30 s	move chip delicately in developer
	Evaporate 150 nm of Al at a rate of 0.2 nm/s or 1 nm/s	For better chamber pressure evaporate Ti for 3 min at 0.2 nm/s while sample is rotated to avoid deposition
	Lift-off in NMP on hot plate at 140 ^{o}C for 20+ min, pipette to remove majority of metal then leave for 30+ more min. Finally rinse in IPA and ACE	Use pipette delicately and dry sample quickly to avoid prolonged nitrogen gun use which may damage the bridges.

5 - JJs	**Spin & Bake** spin MMA EL13 at 3.5 krpm (acceleration 1krpm/s), height, bake at 170°C for 3min then spin PMMA 950k 4% at 4 krpm (acceleration 1 krpm/s), height , bake at 170 ^{o}C for 3 min	
	Ebeam lithography write junctions and undercut with 0.8 nm beam (dose = 110×4 μC/cm^2 with PEC)	
	Develop in water:IPA (1:3) for 2 min and rinse in IPA for 10 s	
	Evaporate 60 nm of Al at a rate of 1 nm/s with the sample tilted by 25 degrees then add oxigen to the chamber in order to oxidised the deposited Al. The time and pressure of this step will determine the thickness of the oxide layer. Then tilt the sample by -25 degrees and deposit 120 nm of Al at 1 nm/s. Finally oxidise the top layer by adding 10mbar of oxigen to the chamber for 2 min.	For better chamber pressure evaporate Ti for 3 min at 0.2 nm/s while sample is shielded to avoid deposition
	Lift-off in NMP on hot plate at 140 ^{o}C for 20+ min, pipette to remove majority of metal then leave for 30+ more min. Finally rinse in IPA and ACE	Use pipette delicately and dry sample quickly to avoid prolonged nitrogen gun use which may damage the bridges.
6 - Bandaids	**Spin & Bake** spin PMMA 600k 6% at 4 krpm (acceleration 1 krpm/s), height 520 nm, bake at 180 ^{o}C for 2 min then spin PMMA 950k 2% at 2 krpm (acceleration 1 krpm/s), height 70 nm, bake at 180 ^{o}C for 2 min	

	Ebeam lithography write bandaids and undercut with 0.8 nm beam (dose = 900 μC/cm² for bandaids and 400 μC/cm² for undercuts)	
	Develop in MIBK:IPA (1:3) for 1 min and rinse in IPA for 30 s	
	Etch with Argon ion gun, 400 V, 21 mA for 5 min. then **evaporate** 240 nm at 1 nm/s	For better chamber pressure evaporate Ti for 3 min at 0.2 nm/s while sample is shielded to avoid deposition
	Lift-off in NMP on hot plate at 140 ^{o}C for 20+ min, pipette to remove majority of metal then leave for 30+ more min. Finally rinse in IPA and ACE	Liftoff is challanging and often one has to scratch the corner of the chip in order to remove the bulk of the metal
	HF vapour in a Memstar machine with 18 T pressure, 2 mg of water for 10000 s or 16 T for 24000 s	Use longer recipe if shorter recipe leaves flouridization on the sample